THE PHASE DIVERSITY OF NICKEL PHYLLOSILICATES FROM NEW CALEDONIA: AN INVESTIGATION USING TRANSMISSION ELECTRON MICROSCOPY (TEM)

A THESIS

SUBMITTED TO THE GRADUATE SCHOOL

IN PARTIAL FULFILLMENT OF THE REQUIREMENTS

FOR THE DEGREE

MASTER OF SCIENCE

BY

BRITTANY CYMES

DR. KIRSTEN NICHOLSON – ADVISOR

BALL STATE UNIVERSITY

MUNCIE, INDIANA

MAY 2016

ABSTRACT

THESIS: The Phase Diversity of Nickel Phyllosilicates from New Caledonia: An Investigation Using Transmission Electron Microscopy (TEM)

STUDENT: Brittany A. Cymes

DEGREE: Master of Science

COLLEGE: Sciences and Humanities

DATE: May, 2016

PAGES: 136

New Caledonia is a French territorial island in the Southwest Pacific with an economy heavily dependent upon nickel-mining, being the 5th largest producer worldwide. The nickel deposits result from tropical lateritic weathering of ophiolite units that were emplaced during the late Eocene. The ultramafic units weathered and continue to weather into bright green Ni-rich phyllosilicates colloquially referred to as 'garnierite'. Detailed investigations of 'garnierite' using transmission electron microscopy (TEM) have been carried out in other locations to characterize important nanoscale features; however, none have been undertaken in New Caledonia.

In this investigation, ten samples of 'garnierite' from New Caledonia were examined with powder X-ray diffraction (XRD) and TEM with energy dispersive spectrometry (EDS). The XRD results show the phyllosilicate material to be comprised of highly disordered talc- and serpentine-like minerals with minor chlorite indicated by significantly broad reflections and two-

dimensional diffraction bands, consistent with published data. TEM analysis, however, revealed new information.

Talc-like minerals occur as fluffy aggregates of crystals with lattices with approximately 10 Å d-spacing and significant crystallographic disorder and also as aggregates of larger crystals with more orderly lattices; these two varieties represent the kerolite-pimelite series and the talc-willemseite series, respectively. Lizardite, chrysotile, and antigorite, with approximately 7 Å basal spacing, were observed in approximately equal measure among the samples. Chlorite occurs as crystals with lattices having approximately 14 Å basal spacing with both high amounts of crystallographic order, indicated by continuous lattices, and as crystals with highly disordered lattices, as observed in the kerolite-pimelite series. Large percentages of silver nanoparticles occur within matrices of amorphous silica within two of the samples. A bimodal size distribution is observed among the nanoparticles, with particles 2 to 30 nm in diameter comprising 75 % of the textures and particles 150 to 650 nm in diameter comprising 25% of the textures.

These findings have several broad implications; (1) the antigorite observed indicates that the ophiolite unit experienced high-temperature alteration at one point in time, which is in disagreement with accepted supergene interpretation of its tectonic history; (2) the high relative chrysotile percentage and the fiber size (50-700 nm) may relate to the high incidence of lung disease among island civilians; and (3) the silver nanoparticles may have significant implications for both the economy of New Caledonia, being of great potential value, and the environment, being very toxic to aquatic and terrestrial flora and fauna and also humans.

ACKNOWLEDGEMENTS

This research was supported by a Ball State University ASPiRE research grant.

To my committee members Dr. Mark Krekeler, Dr. Kirsten Nicholson, and Dr. Jeffry Grigsby: thank you for your dedication, support, time, and mentorship.

To the faculty, staff, and students of Ball State University's Department of Geological Sciences: thank you for your assistance, encouragement, support, and friendship.

To Dr. Richard Edelmann, Mr. Matthew Duley, Michelle Burke, Miami University's Department of Geology and Environmental Earth Science and Center for Advanced Microscopy and Imaging: I cannot express enough gratitude for allowing me access to your facilities and for the immense assistance and support you so freely offered.

To Dr. Christine Clark: thank you for believing in me from day one. Without you, none of this would have been possible.

To my family and friends: thank you for supporting me through this endeavor. Your support, patience, and love are enormously appreciated.

A final thank you to my grandmother and grandfather, words cannot express my enormous gratitude and love. This thesis is dedicated to you both.

Thank you.

TABLE OF CONTENTS

ABSTRACT……...……..i

ACKNOWLEDGEMENTS …….……...…….....iii

TABLE OF CONTENTS …….……..…….Iv

LIST OF FIGURES…….……...…....viii

LIST OF TABLES…….…….……xi

CHAPTER 1: INTRODUCTION AND BACKGROUND…….....……..……1

1.1 GENERAL INFORMATION……..…..1

1.2 GEOLOGIC AND TECTONIC SETTING……...……...…….1

1.3 MINING IN NEW CALEDONIA: IMPORTANCE, HISTORY, ENVIRONMENTAL IMPACTS, AND PUBLIC HEALTH…….…..……5

1.4 MINERALOGY AND NOMENCLATURE……..……..……..7

1.5 TEM STUDIES OF NICKEL PHYLLOSILICATES…….…..14

1.6 OBJECTIVE……...15

CHAPTER 2: METHODOLOGY…….…….17

2.1 SAMPLE ACQUISITION AND SELECTION…….……...17

2.2 Power X-ray Diffraction (XRD) Analysis……..17

2.3 Transmission Electron Microscopy (TEM) and Energy Dispersive Spectroscopy (EDS) Analyses…….……18

Chapter 3: Results……..23

3.1 Powder X-ray Diffraction (XRD) Analysis……23

3.1.1 Sample 1……23

3.1.2 Sample 2……24

3.1.3 Sample 3……24

3.1.4 Sample 4……25

3.1.5 Sample 5……26

3.1.6 Sample 6……26

3.1.7 Sample 7……27

3.1.8 Sample 8……27

3.1.9 Sample 9……28

3.1.10 Sample 10……28

3.2 Transmission Electron Microscopy (TEM) Analysis……40

3.2.1 Sample 1……40

3.2.2 SAMPLE 2……44

3.2.3 SAMPLE 3……44

3.2.4 SAMPLE 4……49

3.2.5 SAMPLE 5……56

3.2.6 SAMPLE 6……58

3.2.7 SAMPLE 7……62

3.2.8 SAMPLE 8……66

3.2.9 SAMPLE 9……68

3.2.10 SAMPLE 10……79

CHAPTER 4: DISCUSSION……85

4.1 NOMENCLATURE……85

4.2 X-RAY DIFFRACTION……87

4.2.1 LORENTZ POLARIZATION (*LP*) AND GENERAL DIFFRACTION CHARACTERISTICS……87

4.2.2 SERPENTINE DEHYDROXYLATION……88

4.2.3 COMMENTS ON MISCELLANEOUS XRD RESULTS……90

4.3 COMMENTS ON TEM AND EDS DATA INTERPRETATION……91

4.4 MINERALOGY……94

4.4.1 Talc-Willemseite and Kerolite-Pimelite……....94

4.4.2 Chlorite…….……96

4.4.3 Lizardite……....97

4.4.4 Chrysotile and Polygonal Serpentine……98

4.4.5 Antigorite…….99

4.4.6 Amorphous Silica……...……100

4.4.7 Silver and Gold……..100

4.5 Assemblage-Based Metamorphic Regime Reconstruction……..…102

4.6 Implications for New Caledonia: Mining and Health…….108

4.7 Further Investigations…….111

Chapter 5: Conclusions……...…113

References…….116

LIST OF FIGURES

CHAPTER 1: INTRODUCTION AND BACKGROUND

FIGURE 1.1: GEOLOGICAL MAP OF NEW CALEDONIA……2

FIGURE 1.2: GENERALIZED STRATIGRAPHIC COLUMN OF NI-LATERITE……4

FIGURE 1.3: SIMPLIFIED DEPICTION OF TURBOSTRATIC STACKING……9

FIGURE 1.4: SIMPLE POLYGONAL DEPICTIONS OF 2:1 PHYLLOSILICATES……11

FIGURE 1.5: SIMPLIFIED POLYGONAL DEPICTIONS OF 1:1 PHYLLOSILICATES……13

CHAPTER 2: METHODOLOGY

FIGURE 2.1: PHOTOGRAPHS OF HAND SAMPLES USED IN INVESTIGATION……21

CHAPTER 3: RESULTS

FIGURE 3.1: XRD PATTERNS OF SAMPLE 1……30

FIGURE 3.2: XRD PATTERNS OF SAMPLE 2……31

FIGURE 3.3: XRD PATTERNS OF SAMPLE 3……32

FIGURE 3.4: XRD PATTERNS OF SAMPLE 4……33

FIGURE 3.5: XRD PATTERNS OF SAMPLE 5……34

FIGURE 3.6: XRD PATTERNS OF SAMPLE 6……35

FIGURE 3.7: XRD PATTERNS OF SAMPLE 7……36

FIGURE 3.8: XRD PATTERNS OF SAMPLE 8……37

FIGURE 3.9: XRD PATTERNS OF SAMPLE 9……38

FIGURE 3.10: XRD PATTERNS OF SAMPLE 10……39

FIGURE 3.11: TEM IMAGES OF NI-PHYLLOSILICATES IN SAMPLE 1……41

FIGURE 3.12: EDS SPECTRA OF NI-PHYLLOSILICATES IN SAMPLE 1……...42

FIGURE 3.13: TEM IMAGES OF AMORPHOUS SILICA AND AG-NANOPARTICLES IN SAMPLE 1…..43

FIGURE 3.14: TEM IMAGES OF NI-PHYLLOSILICATES IN SAMPLE 2……45

FIGURE 3.15: EDS SPECTRA OF NI-PHYLLOSILICATES IN SAMPLE 2……...46

FIGURE 3.16: TEM IMAGES OF CHLORITE AND TALC IN SAMPLE 3……47

FIGURE 3.17: EDS SPECTRA OF CHLORITE IN SAMPLE 3……48

FIGURE 3.18: EDS SPECTRA OF TALC IN SAMPLE 3……48

FIGURE 3.19: TEM IMAGES OF ANTIGORITE IN SAMPLE 3……..50

FIGURE 3.20: EDS SPECTRA OF ANTIGORITE IN SAMPLE 3……51

FIGURE 3.21: TEM IMAGES OF CHRYSOTILE AND CHLORITE IN SAMPLE 4……..52

FIGURE 3.22: EDS SPECTRA OF CHRYSOTILE IN SAMPLE 4……53

FIGURE 3.23: TEM IMAGES OF LIZARDITE AND 5 Å PHASE IN SAMPLE 4……54

FIGURE 3.24: EDS SPECTRA OF LIZARDITE IN SAMPLE 4……55

FIGURE 3.25: EDS SPECTRA OF 5 Å PHASE IN SAMPLE 4……55

FIGURE 3.26: TEM IMAGES OF PHYLLOSILICATES IN SAMPLE 5……57

FIGURE 3.27: EDS SPECTRA OF TALC-LIKE PHASE IN SAMPLE 5……58

FIGURE 3.28: TEM IMAGES OF LIZARDITE IN SAMPLE 6……59

FIGURE 3.29: TEM IMAGES OF CHRYSOTILE IN SAMPLE 6……..60

FIGURE 3.30: EDS OF LIZARDITE AND CHRYSOTILE IN SAMPLE 6……..61

FIGURE 3.31: TEM IMAGES OF CHRYSOTILE IN SAMPLE 7……63

FIGURE 3.32: EDS SPECTRA OF CHRYSOTILE IN SAMPLE 7……64

FIGURE 3.33: TEM IMAGES OF LIZARDITE IN SAMPLE 7……65

FIGURE 3.34: EDS SPECTRA OF LIZARDITE IN SAMPLE 7……66

FIGURE 3.35: TEM IMAGES OF CHLORITE IN SAMPLE 7……..67

FIGURE 3.36: EDS SPECTRA OF CHLORITE IN SAMPLE 7……68

FIGURE 3.37: TEM IMAGES OF CHRYSOTILE AND ANTIGORITE IN SAMPLE 8……..69

FIGURE 3.38: EDS SPECTRA OF CHRYSOTILE AND ANTIGORITE IN SAMPLE 8……70

FIGURE 3.39: TEM IMAGES OF SILVER NANOPARTICLES IN SAMPLE 9……...71

FIGURE 3.40: EDS SPECTRA OF SILVER NANOPARTICLES IN SAMPLE 9……...72

FIGURE 3.41: TEM IMAGES OF AMORPHOUS SILICA IN SAMPLE 9……..74

FIGURE 3.42: EDS SPECTRA OF AMORPHOUS SILICA IN SAMPLE 9……..75

FIGURE 3.43: TEM IMAGES OF KAOLINITE-LIKE PHASE IN SAMPLE 9……76

FIGURE 3.44: EDS SPECTRA OF KAOLINITE-LIKE PHASE IN SAMPLE 9…….……77

FIGURE 3.45: TEM IMAGES OF CHRYSOTILE AND ANTIGORITE IN SAMPLE 9…….……..78

FIGURE 3.46: EDS SPECTRA OF ANTIGORITE IN SAMPLE 9…….……79

FIGURE 3.47: TEM IMAGES OF CHLORITE AND TALC IN SAMPLE 10…….……...81

FIGURE 3.48: EDS SPECTRA OF TALC IN SAMPLE 10…….……..82

FIGURE 3.49: TEM IMAGES OF ANTIGORITE AND CHRYSOTILE IN SAMPLE 10…….……83

FIGURE 3.50: EDS SPECTRA OF ANTIGORITE IN SAMPLE 10…….……...84

LIST OF TABLES

CHAPTER 2: METHODOLOGY

TABLE 2.1 DESCRIPTIONS OF SAMPLES USED IN INVESTIGATION…….……...22

CHAPTER 4: DISCUSSION

TABLE 4.1: SUMMARY OF PHYLLOSILICATE PHASES OBSERVED USING XRD AND TEM WITH EDS……..……...103

1. INTRODUCTION AND BACKGROUND

1.1 General Information

Hydrous nickel-bearing phyllosilicates, a group of minerals colloquially referred to as 'garnierite', form through the serpentinization and tropical weathering of obducted ultramafic rocks. 'Garnierite' species comprise nickeliferous analogues of several species of phyllosilicates including but not limited to serpentine, talc, chlorite, and sepiolite. Detailed transmission electron microscopy (TEM) studies of Ni-phyllosilicates are few (Villanova-de-Benavent et al., 2011, 2015; Soler et al., 2008) and none have been undertaken in detail on the Ni-laterite deposits in New Caledonia. Little is known regarding 'garnierite' complexity with respect to structural intermediates, mineral transformation reactions, and the nature and diversity of poorly crystalline phases amongst this mineral group.

1.2 Geologic and Tectonic Setting

New Caledonia (Fig. 1.1) is a narrow, elongate island 400 km long and 40 km wide located roughly midway between Australia and the Fijian Islands (Lillie and Brothers, 1969). The island consists of a large, allochthonous sheet of oceanic lithosphere (the ultramafic nappe occupying 5,600 km^2 or 30% of the island's surface area (Losfield et al., 2015)) thrust over continental basement as a result of the closure of back-arc and forearc ocean basins during the late Eocene (Avias, 1967; Paris, 1981; Aitchinson et al., 1995; Cluzel et al., 2001; Crawford et al., 2003; Schellart et al., 2006). The basement represents a fragment of continental crust that drifted away from Australia due to the break-up of the eastern margin of Gondwana initiated in the late Cretaceous (Yang et al., 2013).

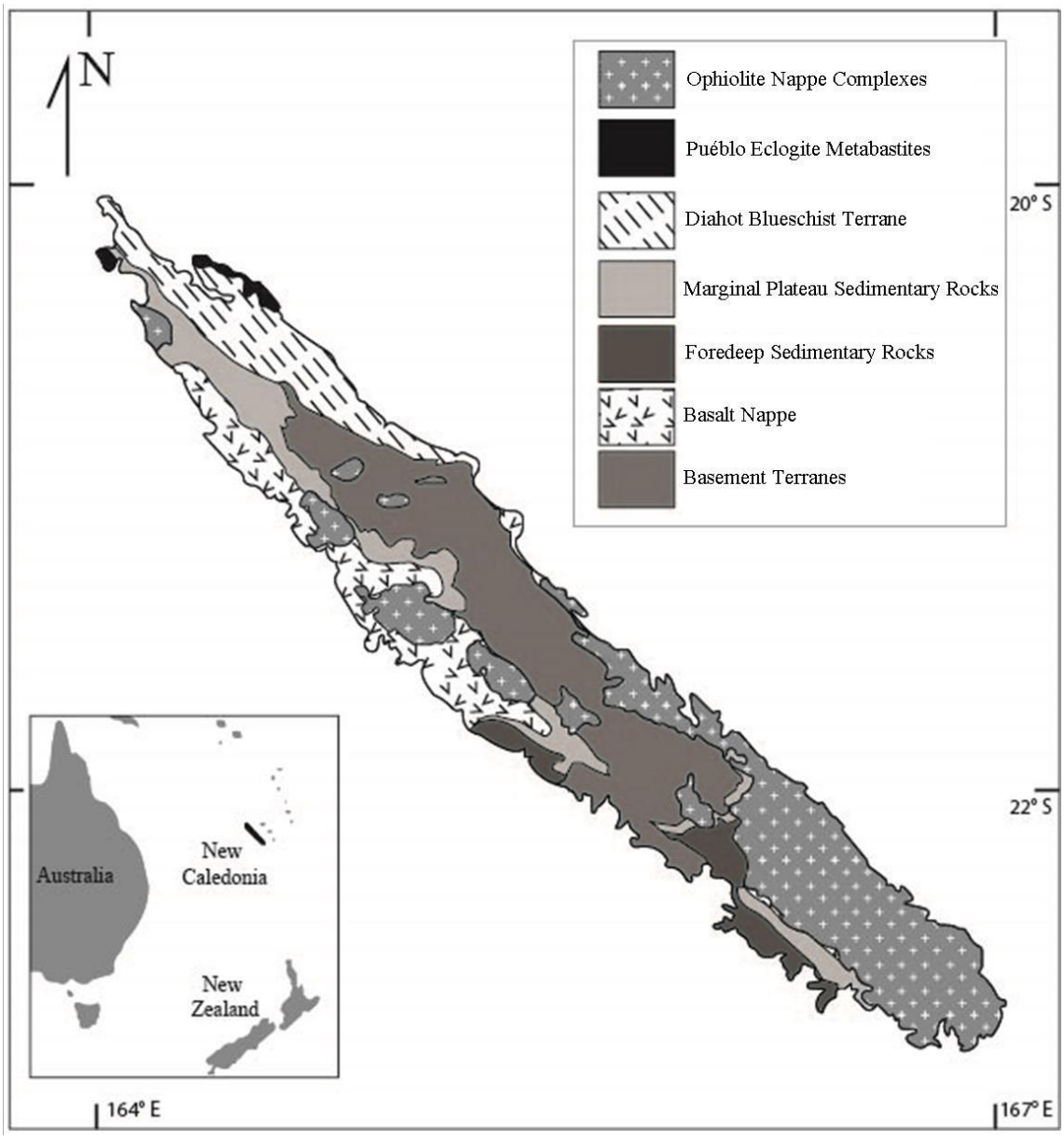

Figure 1.1 Simplified geologic map of New Caledonia, illustrating the major tectonostratigraphic units of the island (after Fitzherbert et al. 2003).

The laterization of the serpentinized ultramafic rocks, mainly of harzburgite and dunite composition, resulted in the supergene enrichment of nickel in the secondary phyllosilicates (Lillie and Brothers, 1969; Wells et al., 2009). Extensional tectonics are thought to have acted upon these units post-obduction, directly impacting their development and distribution by

increasing ground water penetration (LaGabrielle and Chauvet, 2008), however, there is still controversy about the ophiolite units being the product of a rear-force thrust emplacement or a passively emplacement (LaGabrielle et al., 2013).

Figure 1.2 shows a generalized stratigraphic column of the laterite complexes in New Caledonia. With some author to author deviation, the regolith is divided into the following zones from bottom to top: (1) the ultramafic parent rock (may be completely or partially serpentinized); (2) the rocky and earthy saprolite zones containing phyllosilicates (mostly serpentine- and talc-like phases occurring as coatings, boxworks, and vein infills) as the main Ni-host; (3) the transitional laterite (not recognized by all authors) containing smectite and Mn-oxides; and (4) the limonitic laterite zone containing Fe-oxyhydroxides such as goethite as the dominant Ni-host (Manceau and Calas, 1985; Wells et al., 2009; and Dublet et al., 2012). Similar differentiation has been made in other localities where nickeliferous laterites are found, such as in Venezuela (Soler et al., 2008).

The Ni-rich phyllosilicates mined from laterites in New Caledonian appear to have formed in two generations: a high-temperature generation associated with serpentinization of the ocean crust and a low-temperature generation associated with post-obduction tropical weathering; this is evidenced by differences in Ni-distribution in the crystal structures (Dublet et al. 2012; Manceau and Calas, 1985). Differentiation upward from the contact of the ophiolite sheet with the underlying terrane is characterized by decreased Ni-content and the prevalence of oxides over phyllosilicates as a stable host (Dublet et al., 2012). Primary serpentinization has been found to incorporate elements such as chlorine, fluorine, and sulfur from circulating seawater, organic matter, and diverse crustal lithologies into the parent rock (Kendrick et al.,

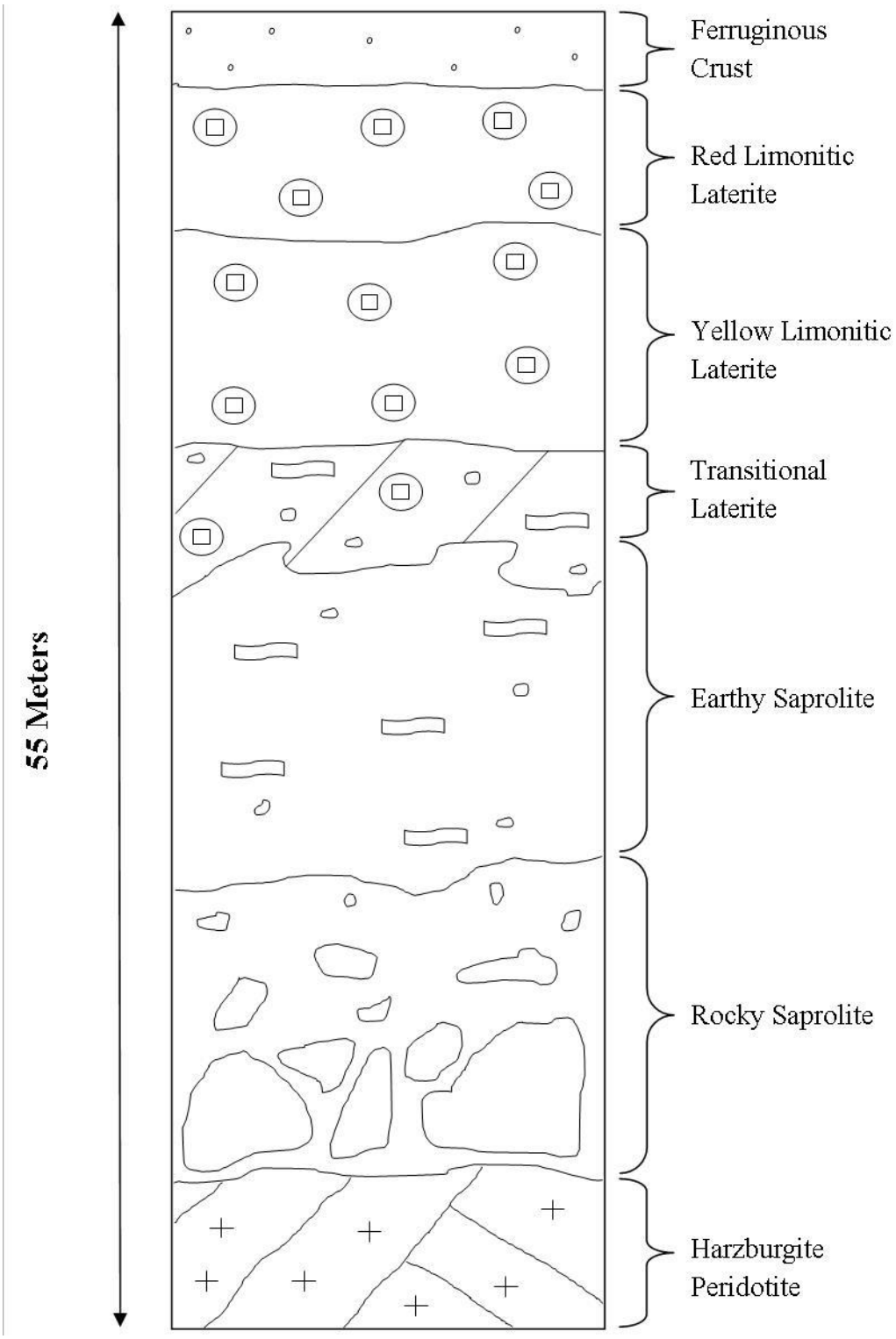

Figure 1.2 Generalized stratigraphic column of the Ni-laterite complexes in New Caledonia (after Manceau and Calas, 1985; Wells et al., 2009; and Dublet et al., 2012).

2013; Debret et al., 2014). The vertical speciation of these components in Ni-laterite units and indeed their relationship with the 'garnierite' is poorly understood.

1.3 Mining in New Caledonia: Importance, History, Environmental Impacts, and Public Health

Nickel laterite deposits are extremely important economically. New Caledonia is the fifth largest nickel producer worldwide after Russia, Indonesia, Canada, and Australia with an annual production of 107,000 tonnes in 2009 and a reserves estimate of 7,100,000 tonnes (U.S.G.S. Mineral Commodity Summary, 2010). The share of the island's gross domestic product (GDP) was on average 8.6 % (±3.6 %) over 1999-2008 and reached a record high above 30 % in 1968 (Losfield et al., 2015). Over the same time span, exports of nickel (including ores and refined products) accounted for an average 93 % (±3.2 %) of the total value of exports from New Caledonia (Losfield et al., 2015). Major uses of nickel include stainless steel production (58 %), Ni-based alloys (14 %) casting alloys and steel (9 %), and rechargeable batteries (5 %) (Mudd, 2010).

Nickel mining began in New Caledonia in the 1870's. At first, operations were mainly carried out underground following high grade lodes, but over time, open-cast mining became dominant as ore grade decreased. Mechanization after World War II, increased the ability to exploit low-grade ores at a larger scale than previously attained using labor force (Losfield et al., 2015). These ores were treated using blast furnaces from 1910 to 1957 and rotary kiln electric furnaces (RKEF) were introduced in 1958 and are still in use today (Mudd, 2010).

Up until the mid-1970's mining was a reckless pursuit with little thought to the consequences of poor extraction techniques and spoil management; unheeded, environmental

effects accumulated. The resulting perturbed water flow and dramatic soil erosion due to scraping out the soil to access the ore caused metal-rich sediment to be transported downstream into rivers and lagoons where bioaccumulation and toxicity to marine organisms, not to mention the destruction of habitat for terrestrial species, was severe (Bird et al., 1984; Dupon, 1986; Latham, 1971; Ambastian et al., 1997; Fernandez et al., 2006; Mignon et al., 2007; Dullion et al., 2010; Bustamante et al., 2000; Hédouin et al., 2007; Florence et al., 1994).

New Caledonia is widely recognized as a hot spot for biodiversity; however, the island's ecology is under increasing anthropogenic pressure due to mining. The marine environment in particular is highly regarded and the lagoons are now listed as World Heritage Sites (UNESCO, 2013). Environmental issues related to mining are high on the political agenda in New Caledonia (Jaffré et al., 2010; L'Huillier et al., 2010; Pascal et al., 2008; Wulff et al. 2013).

Mining practices are improving and where impacts are inescapable, ecological restoration is now considered. Novel techniques to battle environmental impacts, such as phytoremediation, are on the horizon. Continuous accumulation of metal rich sediment caused phototoxicity and accumulation in cultivated plants and thus the loss of fertile lands (Danloux and Laganier, 1991; Dupon, 1986; Jaffré et al., 1977). With phytoremediation, plants that have become accustomed to high metal concentrations in the soil, called metallophytes, are used to remediate and then as metal rich biomass for ecocatalysis (Lossfield et al., 2015; Cunningham and Berti, 1993).

Although the mining companies appear to be addressing environmental concerns, there is great political unrest in New Caledonia related to the topic. Indigenous environmental groups commit violent protests in response to the handling of the mining industry by the government (Horowitz, 2009). The source of the trouble is the nonexistence of formal French or European

Union environmental regulations on mining practices, leaving mine operations themselves as the responsible party (Ali and Grewal, 2006).

High incidences of malignant mesothelioma (MM) have been observed in New Caledonia. Langer et al. (1980) identified chrysotile asbestos as a cofactor in carcinogenesis among nickel-processing workers on the island. Luce et al. (2000) attributed the high rates of MM to tremolite-containing whitewash that the residents use for their homes. Baumann et al. (2011) further delineated the cause of high MM incidence by studying human proximity to sources of amphibole and serpentine asbestos and found a stronger association with the serpentines than with the amphiboles, indeed, they identified that the presence of serpentine on the roads is a major environmental risk fact for MM in New Caledonia.

Much of the literature on the mineralogical nature of the nickel phyllosilicates in New Caledonia states that the samples, based on XRD analysis, are largely comprised of lizardite and talc-like phases, with the presence of chrysotile being noted, but underplayed in terms of quantity. It is abundantly clear from the medical literature that chrysotile exists in significant amounts in the laterite deposits but to what degree they comprise them is poorly understood.

1.4 Mineralogy and Nomenclature

Nickel phyllosilicates from New Caledonia (referred to as ‘garnierite’ in the same sense as ‘bauxite’ and ‘limonite’) are comprised largely of intimate mixtures of talc- and serpentine-like phases, characterized by approximately 10 Å and 7 Å basal spacings, respectively (Wells et al., 2009; Kato, 1961; Brindley and Hang, 1973; Maksimovic, 1973; Brindley and Wan, 1975; Maksimovic, 1966; Brindley et al., 1979). Minor amounts of chlorite (Kato, 1961; Montoya and

Baur, 1963), sepiolite (Cluzel and Vigier, 2008; Springer, 1976; Manceau et al., 1985), and smectite (Manceau et al., 1985; Wells et al., 2009) are also found associated with these phases.

These minerals are easily recognizable by their bright green color which is a function of nickel content (Pecora et al., 1949; Brindley and Hang, 1973). Higher nickel content is also associated with higher specific gravity and higher mean index of refraction when compared to the magnesium end members (Pecora et al., 1949; Brindley and Hang, 1973). No correlation has been observed between the weight per cent NiO and phase morphology, meaning Ni^{2+} ions replace Mg^{2+} ions without a major effect on the crystal structure; however, Ni has been noted to decrease the quality of crystallization in serpentines once Ni exceeds 1.5 atoms per formula unit (*apfu*) (Uyeda et al., 1973; Brindley and Wan, 1975). One could speculate that nickel decreases structural stability in large concentrations due to being slightly smaller in size than magnesium, however, formation conditions likely play a large role in this correlation.

The talc-like component of the 'garnierite' ore is referred to as 'talc-like' due to the presence of great amounts of crystallographic disorder, which leaves ambiguity in terms of the identification of a specific phase. This disorder is in addition to the already intermixed state this material exists in with serpentine phases. Indeed, the intimacy of the talc-like and serpentine phases is such that monomineralic material by mechanical separation is difficult to obtain (Manceau and Calas, 1985; Brindley et al., 1979). The great amount of structural disorder in the talc-like phase is referred to as turbostratic stacking (Fig. 1.3) and the structural phenomenon as a whole is often referred to as a random layer lattice. Random layer lattices are ones in which the layers are arranged parallel to one another about the normal but at random in translation parallel

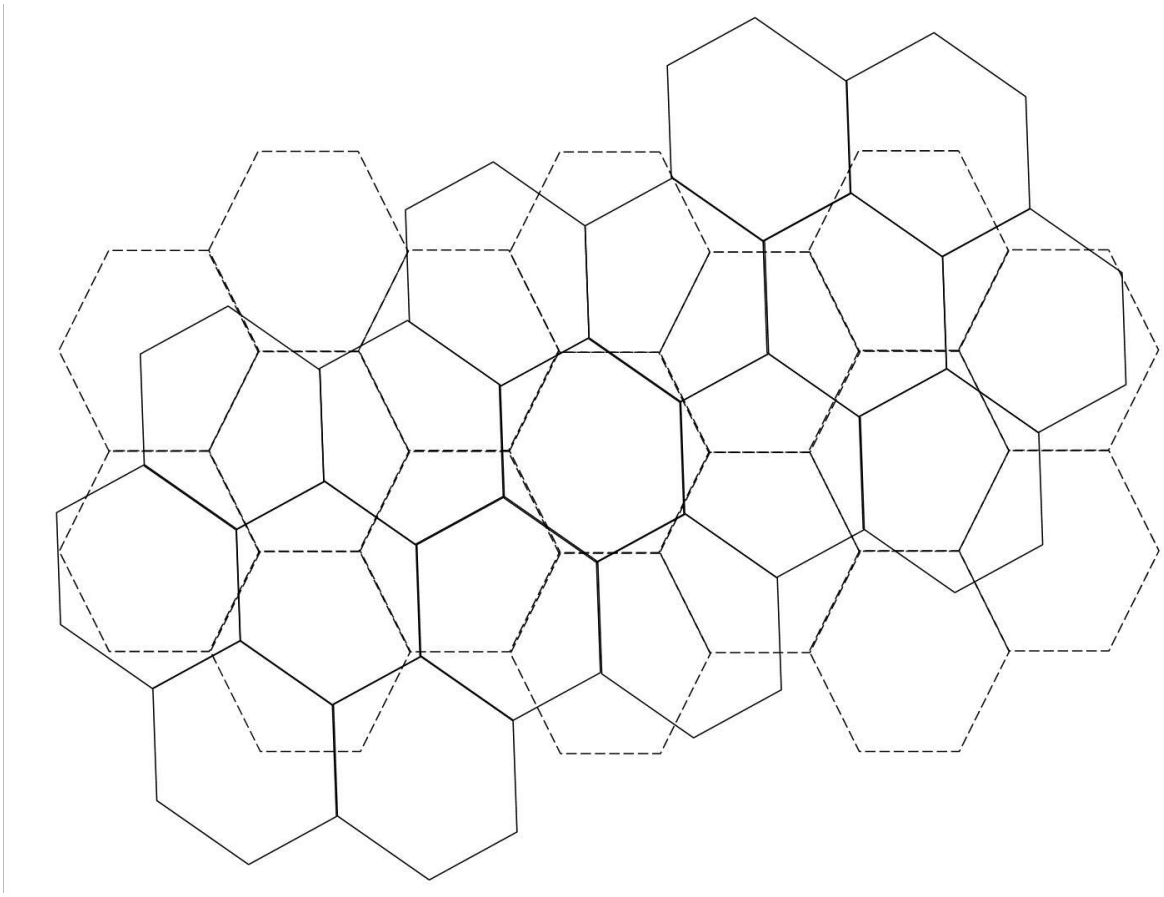

Figure 1.3 Simplified depiction of turbostratic stacking.

to the layer (Warren, 1950); carbon allotropes also commonly display turbostratic stacking. This phenomenon is fundamentally different from polytypism in which layers of fixed chemical composition are stacked in sequences with a specific periodicity, discussed at length for phyllosilicates by Bailey and Banfield, (1995), Bailey, (1988), Banfield and Bailey, (1996), Bailey, (1969), and Kogure et al. (2006).

Kerolite and pimelite ($Mg_3Si_4O_{10}(OH)_2•H_2O$ – $Ni_3Si_4O_{10}(OH)_2•H_2O$) are used as varietal terms by Brindley and Maksimovic (1974), Brindley et al. (1977), and Brindley et al. (1979) as well as more recent authors (Manceau and Calas, 1985; Wells et al., 2009) to describe talc and

willemseite ($Mg_3Si_4O_{10}(OH)_2$ – $Ni_3Si_4O_{10}(OH)_2$) with turbostratic stacking of the layers and additional surficial 'water' in the form of either OH or molecular H_2O. It is important to note that kerolite and pimelite are not swelling minerals as much of the older literature suggests but rather the additional water in the formulae corresponds to water held by external surfaces and not in the interlayer (discussed in detail by Brindley and Maksimovic (1974) and Brindley et al. (1979)). Kerolite and pimelite are in the talc-willemseite group and not member of the smectite group (Brindley et al. 1977). Accounts of partial swelling of kerolite-pimelite minerals exist, but they are likely due to small amounts of interstratified expandable clays (Schmidt, 1884; Spangenberg, 1938; Faust, 1966) as well as the decrease of van der Waals and electrostatic attraction between the layers as a result of weakly bonded layers in kerolite in comparison to talc (Brindley et al., 1977).

Talc-like minerals fall into the structural classification of 2:1 layer phyllosilicates (Fig. 1.4) meaning that there is one octahedral sheet (O) sandwiched between two tetrahedral sheets (T). Smectite is isostructural with talc; however unlike talc, smectite is a swelling or expandable clay, meaning that it will incorporate water and other organic fluids between the interlayers. Chlorite is also a 2:1 phyllosilicate, however it has an additional brucite ($Mg(OH)_2$) layer between the T-O-T sheets, bringing the basal spacing up to ~14 Å. Sepiolite is a fibrous 2:1 phyllosilicate that is fundamentally different from other layer minerals in that the octahedral sheets extent only in one dimension and the tetrahedral sheets are divided into ribbons by periodic inversions of the tetrahedral layer known as modulation. This inversion creates units known as polysomes.

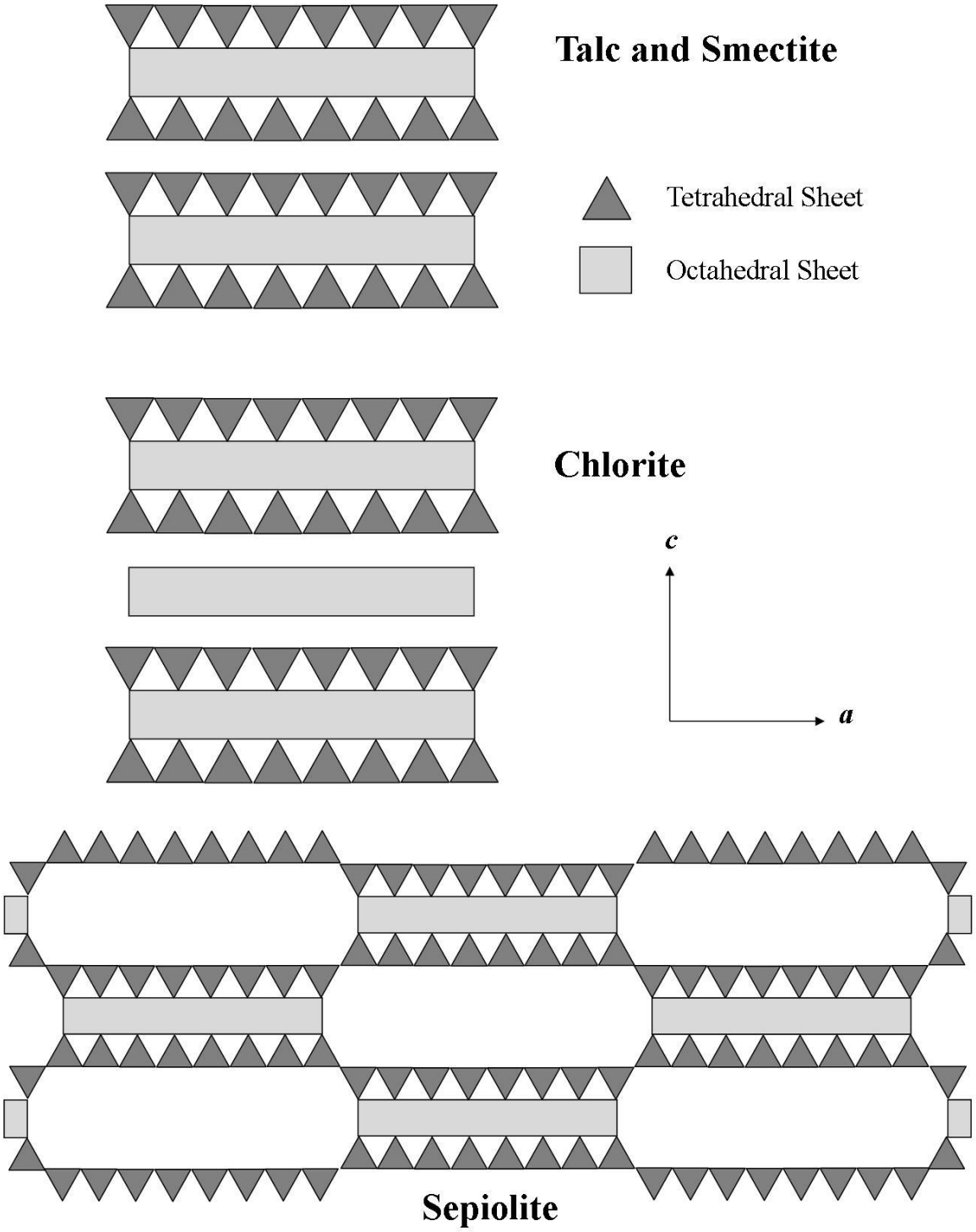

Figure 1.4 Simple polygonal models depicting the structural arrangement of the tetrahedral and octahedral sheets in the 2:1 layer phyllosilicates talc and smectite (the latter is swelling and the former is not), chlorite (2:1 + brucite layer), and sepiolite (modulated structure).

Serpentine ($Mg_3Si_2O_5(OH)_4$) classification is based on variable tetrahedral-octahedral (1:1) composite layers (Fig. 1.5) (Whittaker and Zussman, 1956). Lizardite is characterized by flat layers, chrysotile by curled layers, and antigorite by corrugated layers (Wicks and Whittaker, 1975). Chrysotile and antigorite lattice curvature is thought to result from the greater basal dimension of the octahedral sheet (Wicks and O'Hanley, 1988). Chrysotile accommodates this misfit between the tetrahedral and octahedral sheets by forming hollow core fibers with a cylindrical lattice whereas antigorite accommodates the misfit by modulating the tetrahedral sheet, flipping it 180 degrees periodically along the (100) direction. This modulation is referred to as a superstructure, a supercell, or as having superlattice periodicities; these modulations can vary widely from 16 to 110 Å in length (Dodony et al. 2002; Uehara, 1998; Zussman et al., 1957).

A fourth main layer type configuration in 1:1 layer silicates is known as polygonal or Povlen-type serpentine. In polygonal serpentine, fifteen or thirty flat radial sectors are arranged about a chrysotile fiber, representing partial dislocations per turn as required for serpentine polytype translational operators. This geometry is considered to represent a structural intermediate between chrysotile and lizardite (Baronnet, et al., 1994, Baronnet and Devouard, 2005; Millini, 1986).

Nickel analogues of lizardite and chrysotile ($Ni_3Si_2O_5(OH)_4$) are known as nepouite and pecoraite, respectively; a nickel antigorite has not yet been observed in New Caledonia (Brindley and Wan, 1975; Uyeda et al., 1973). One must tread carefully when searching for accounts of nickel-bearing antigorite in the strict sense of a mineral with a long superlattice *a* parameter.

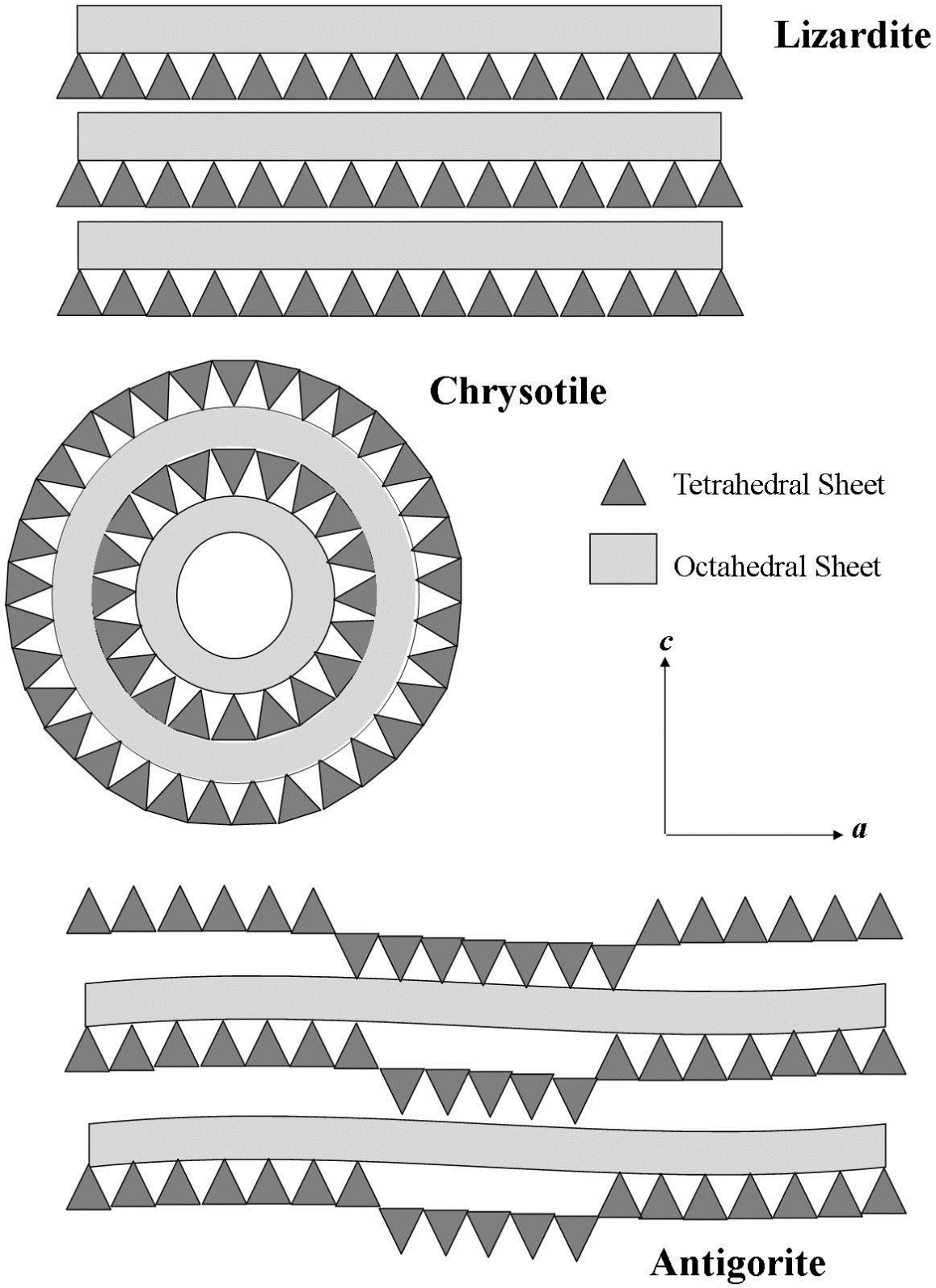

Figure 1.5 Simple polygonal model depicting the structural arrangement of the 1:1 layer serpentine polymorphs lizardite (flat sheets), chrysotile (curled tubes), and antigorite (modulated structure).

Older literature refers to lizardite found in New Caledonia, the serpentine with platy morphology, as antigorite and works published outside of the mineralogy field, notably

environmental and medical research, refer to all fibrous serpentine (or any serpentine) as antigorite when chrysotile was likely the phase present.

1.5 TEM Studies of Nickel Phyllosilicates

There are few studies of nickel phyllosilicates that employ transmission electron microscopy (TEM) as an analytical technique. A possible reason for this paucity is the difficulty associated with TEM work in phyllosilicates. Due to their high water content and structural delicacy, phyllosilicates rapidly become amorphous under the electron beam, making quality imaging an oftentimes frustrating enterprise.

The earliest nanoscale images of 'garnierite' were electron micrographs obtained by Uyeda et al. (1973). A garnierite sample from New Caledonia was one of over forty samples selected for characterization using electron optical microscopy in their three-part study (the other parts are Brindley and Hang, 1973 (part I) and Hang and Brindley, 1973 (part III)). The sample displayed predominantly 10 Å talc-like forms but also contained regions with approximately 7 Å spacing (identified as lizardite and chrysotile). TEM images of New Caledonian Ni-phyllosilicates were also obtained by Pelletier (1983) and broadly show them to be comprised of 10Å talc-like phases and 7 Å serpentines identified as lizardite and chrysotile associated with silica gel.

Villanova-de-Benavent et al. (2011) and Villanova-de-Benavent et al. (2015) examined material from a Ni-laterite in the Dominican Republic. Their ion-milled samples were comprised

of kerolite-pimelite minerals with 9.5 to 10 Å basal spacings occurring in bundles and platy aggregates and serpentine phases with cylindrical (chrysotile) and well-developed 15-sectored polygonal morphologies with ~7 Å basal spacings. Soler et al. (2008) performed TEM on a

'garnierite' sample from a Ni-laterite deposit in Venezuela; their grain-mount showed a mixture of 7 Å and 10 Å phases, the former displaying a tendency toward curved and polygonal structural varieties and the latter having poor crystallinity consistent with kerolite-pimelite minerals. Suarez et al. (2011) captured excellent TEM images and selected area electron diffractions (SAED) in their examination of chlorite and serpentine from a weathered sulfide deposit in Spain using TEM. They were assessing these phases as effective Ni-Cu sinks during the weathering process. Their ion-milled samples showed chlorite in well-defined 14.0 to 14.2 Å packets inter-grown with smectite, talc-like phases, saponite, and flat-layered serpentine.

Bloise et al. (2010), Bentabol et al. (2007), and McDonald et al. (2009) captured excellent TEM images in their characterizations of synthetic 1:1 nickel phyllosilicates. Their products were well-ordered and prove useful to the study of natural analogues as they show the 'ideal' structures.

Nanoscale imaging using TEM has proved vital to the complete understanding and characterization of the phyllosilicates found in Ni-laterites. Their extremely fine-grained nature and heterogeneity often make traditional identification techniques difficult to employ. Indeed, TEM should be used in conjunction with other techniques such as XRD in order to fully understand the crystal structures of Ni-phyllosilicates.

As the economy and wellbeing of New Caledonia rely heavily on the exploitation of these Ni-rich deposits, a detailed characterization is necessary as components may exist

unrecognized by other analytical techniques, the identification of which could drastically affect mining practices.

1.6 Objective

The purpose of this investigation is to improve our understanding of the phase diversity of nickel phyllosilicates from New Caledonia. Earlier investigations of the deposits reveal a complex mineral suite that would benefit from the improved characterization that has been achieved in Ni-phyllosilicates from other localities using transmission electron microscopy. At the nanoscale, features such as transformation reactions, structural intermediates, and poorly crystalline phases can be explored that are not always apparent with traditional analytical techniques. Different phases and their relationships with one another may reveal information about their formation history and, therefore, inform interpretations of New Caledonian tectonics, which are still a great source of controversy. Finally, nickel mining is the major driver of the island's economy, with strong effects on country planning, policy, population growth, livelihoods, ways of life, and the environment. An enhanced understanding of these important deposits has the ability to impact multiple facets.

2. METHODOLOGY[1]

2.1 Sample Acquisition and Selection

Seventy-five pounds of garnierite-containing rock (identified by the characteristic green color) were collected from freshwater streams throughout the island of New Caledonia. A binocular microscope was used to select study material; ten green clay-like samples, shown in Figure 2.1 and described in Table 2.1, were hand-picked based on variations color, texture, and morphology in order to maximize the chances of observing large phase diversity among the study material. Material was carefully removed from the host rock using an X-ACTO knife and steel probe under a binocular microscope.

2.2 Powder X-ray Diffraction (XRD) Analysis

X-ray diffraction was performed using a Rigaku Miniflex 600 with CuKα radiation (λ = 1.5418 Å) operated at 15 mA and 40 kV. Patterns were obtained by scanning 2θ = 2° to 35° in step-scan mode at a 0.01 step size with a 1.0 second dwell time.

The powders were prepared by gentle up-and-down and 'rocking' hand-crushing in an agate mortar and pestle. This method is key to preserving the crystal structure of the clay minerals, which can be damaged by manual or mechanical grinding. In order to maximize reflections needed to identify clay phases, the samples were applied to glass slides using ethyl alcohol to smear, inducing a preferred orientation with the (001) face of the crystals parallel to the slide.

[1] All figures and tables are located at the end of this chapter.

One of the sample treatments, glycerol solvation, ended up being problematic. The glycerol was applied by hand rather than by vapor-deposition; this often led to greatly diminished patterns due to oversaturation. It also produced a 'ramping' effect in the pattern toward the two-dimensional *hk* diffraction bands ~20 (2θ) which is interpreted as the large glycerol molecule coating the surface and 'blurring' the turbostratified crystals (see Chapter 3.1).

The samples were run untreated air-dried, solvated with glycerol, solvated with ethylene glycol at 60°C for a minimum of 8 hours, heated to 350°C for 1 hour, and heated to 550°C for 30 minutes. The XRD patterns were processed and identified using MDI Jade 7, criteria of Moore and Reynolds (1997), and comparison to published values.

2.3 Transmission Electron Microscopy (TEM) and Energy Dispersive Spectroscopy (EDS) Analysis

Samples were prepared for TEM analysis using a method modified from Kim et al. (1995) and used with success by Krekeler et al. (2004) and Krekeler and Guggenheim (2008) to preserve texture and increase phyllosilicate resistance to beam damage related to the water mobility in the sample from the vacuum and electron-beam heating.

Small chips of each sample were placed in small glass vials for immersion and exchange under refrigeration. The samples were immersed in methyl alcohol for 1 week, then a solution of 25% London Resin White (LRW) medium and 75% methyl alcohol for 1 week, then a solution of 50% LRW and methyl alcohol for 1 week, then a solution of 75% LRW and 25% methyl alcohol for 1 week, and finally chips were immersed in 100% LRW for 1 week. Two to three drops of LRW accelerator were then added to each vial at room temperature in a cool water bath

to dissipate heat. Polymerization occurred within 5–10 minutes. Samples were then allowed to cure for 24 hours.

After curing, sample plugs were broken free of the glass vials and sliced into 1 to 2 mm slices using a diamond-coated blade; these slices were then adhered to frosted glass slides using Crystalbond. After cooling, the sample mounts were hand-polished using 600 silicon carbide grit and 1 μm aluminum oxide grit until samples were very thin and barely visible; the slides were then cleaned in a sonic bath between and after polishing in order to remove excess grit that might have potentially embedded itself into the sample. 3 mm copper grids were mounted onto the polished samples using super glue. After the glue hardened, in order to facilitate removal, a steel probe was used to scrape around each grid. Finally, the sample-laden grids were removed by heating the glass thin section and melting the Crystalbond. The grids were ion milled to produce perforations at a glancing angle of 4° using a Gatan ion-mill.

Grain-mounted samples were also prepared. The material was crushed into a fine-powder, suspended in ethyl alcohol, and applied to 3 mm lace carbon grids. Although this preparation method serves to make image acquisition more challenging, it advantageous due to rapidity of preparation.

Samples were analyzed using a JEOL JEM-2100 TEM equipped with a Gatan 833 Orius camera and an energy dispersive spectroscope (EDS) which collects elemental abundances for a selected area. The TEM images were collected in brightfield at a 200kV accelerating voltage. In order to further increase image quality and reduce radiation damage to the sample, spot sizes 2-4 were often used to decrease electron flux as well as additional careful operation of brightness adjustment during analysis.

Selected area electron diffraction (SAED) was used to produce diffraction patterns using parallel electron beams; these patterns enhance TEM crystal structure identification in addition to morphological identification and lattice profiling using the Gatan software.

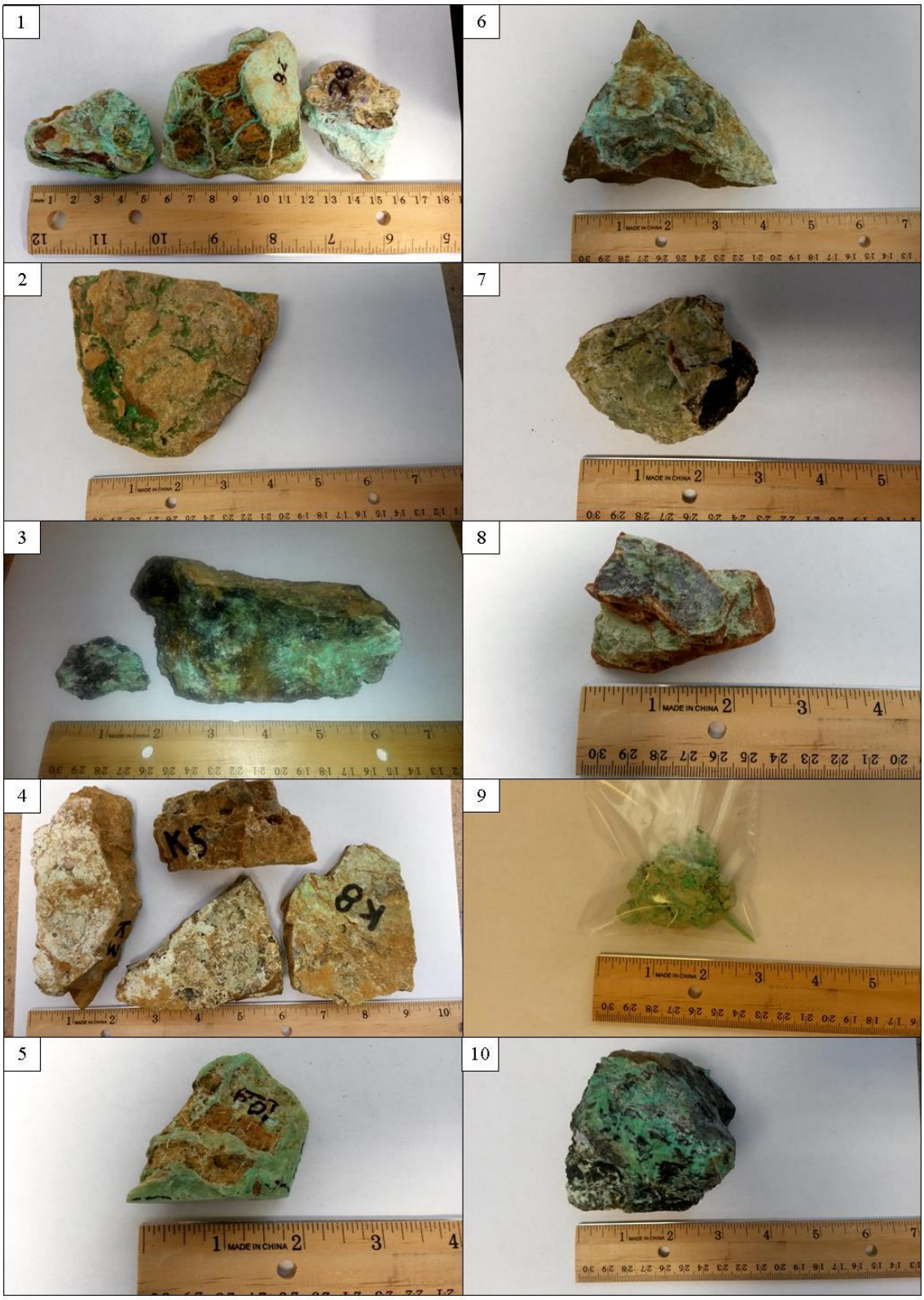

Figure 2.1 Photographs of the hand specimens selected for the investigation.

Table 2.1 Description of bulk samples collected for examination.

Sample	Description
1	Buff to orange-brown rock hosting veins and encrustations of mint- to olive-green phyllosilicates and orange quartz.
2	Buff colored rock hosting discrete layers and cavity in-fills of bright mint-green phyllosilicates with lighter green banding.
3	Orange-brown to dark gray rock with a high specific gravity containing earthy-lustered bright mint-green and greasy-lustered dark olive green phyllosilicates encrusting on it and embedded within it. Moderately magnetic.
4	Orange-brown rock with pale gray-green phyllosilicates encrusting the surface and occupying discrete layers as well as veins of quartz. Black arborescent growths are present on the phyllosilicates.
5	Orange-tan rock with mint-green phyllosilicate encrusting the surface and occupying discrete layers as well as lacy veins of quartz crossing the surface.
6	Orange-brown rock with pale green and powder phyllosilicates and drab olive-green dull-lustered phyllosilicates encrusting the surface.
7	Buff to black and oxidized rock with quartz in 2 mm veins covering the surface as well as encrusting within hollows. The phyllosilicate is light olive-green with a dull luster and encrusts and occupies discrete layers within the rock.
8	Burnt-orange rock containing two 0.2 to 0.5 cm cavities filled with orange quartz crystals as well as pale olive-green, sub-vitreous phyllosilicates encrusting on the surface and occupying discrete layers. The phyllosilicate is fibrous in habit.
9	Delicate, crumbly mint-green phyllosilicate in association with quartz. Some dark gray arborescent growths are present.
10	Dark gray-brown rock with several distinctive minerals present, including a bronze metallic-looking mineral, white amorphous-looking silica, mint-green waxy phyllosilicates, and dark green-black-brown pyroxene. Moderately magnetic.

3. RESULTS

3.1 Powder X-ray Diffraction (XRD)[2]

3.1.1 Sample 1

Sample 1 (Fig. 3.1) is a mixture of talc-like and serpentine phases. The intensity of the talc (001) reflection, with a d-spacing of 10 Å and a full width at half maximum (FWHM) of 1.4°, increases upon heating indicating that the extremely fine-grained material improves in crystallinity, however, the interlayer disorder does not improve significantly as indicated by the reflection broadness; this and the broadness of the serpentine (002) reflection, with a d-spacing of 7.4 Å and a FWHM of 0.4°, are a function of interstratification between the two phases. The prominent talc (02,11) band indicates intralayer disorder. Overlapping the talc (02,11) reflection is the serpentine (100) or (020) reflection; the former is the index consistent with lizardite whereas the latter represents the index for chrysotile and antigorite for that interval.

Upon glycerol solvation, all of the samples gain a poorly defined reflection between approximately 15° to 19.5° (2θ) leading up to reflections in the approximately 20° (2θ) range. The serpentine (002) reflection and the serpentine (004), with a d-spacing of 3.7 Å and a FWHM of 0.4°, do not collapse at 550°C. The talc (003) reflection, with a d-spacing of 3.2 Å and a FWHM of 1.6°, occurs in the untreated pattern as a shoulder off the right side of the quartz (011) reflection and becomes obscured upon glycerol solvation due to apparent over-saturation with glycerol or pooling on the surface of the clay material; this occurs in many of the samples. A

[2] All XRD patterns are located at the end of section 3.1

portion of the talc (13,20) band and the serpentine (201) reflection is present beginning at ~34° (2θ).

3.1.2 Sample 2

Sample 2 (Fig. 3.2) consists of a mixture of talc-like and serpentine phases. The talc (001) reflection, with a d-spacing of 10 Å and a FWHM of 1.8°, increases in intensity upon heating, indicating increased crystallinity. The serpentine (002), with a d-spacing of 7.2 Å and a FWHM of 0.8°, and (004), with a d-spacing of 3.6 Å and a FWHM of 1.1°, reflections collapse entirely at 550°C. The talc (02,11) diffraction band, with the overlapping serpentine (100,020), is present indicating turbostratic intralayer stacking. The talc (003) reflection, with a d-spacing of 3.3 Å and a FWHM of 2°, shifts and intensifies with heating as a function of increased crystallinity. Also present is the talc (13,20) band and serpentine 201 reflection beginning at ~34° (2θ). The glycerol-solvated pattern for this sample greatly diminished the reflections due to error during preparation. Ethylene glycol solvation produced no change in the pattern indicating the absence of expandable phases.

3.1.3 Sample 3

Sample 3 (Fig. 3.3) is comprised of a mixture of serpentine, chlorite, and a very fine-grained talc-like phase. The chlorite (001) is a broad 14.1 Å reflection at 6.3° (2θ) with a FWHM of 0.4°. Other chlorite reflections indexed include the (003), with a d-spacing of 4.7 Å and a FWHM of 0.5°, and the (005), with a d-spacing of 2.8 Å and a FWHM of 0.6°, which are slightly sharper in intensity. The chlorite (001) reflection increases significantly in intensity at 550 °C;

the d-spacing also changes to 14.8 Å. The chlorite (003) and (005) reflections do not vary greatly upon heating.

The talc (001) reflection, with a d-spacing of 10.1 Å and a FWHM of 1.5°, is not visible until heated to 550 °C due to extremely fine grain size. The talc (003) reflection is barely distinguishable as a very broad swell in the approximately 28° (2θ) range in the 550°C run. The serpentine (002), with a d-spacing of 7.1 Å and a FWHM of 0.5°, and (004), with a d-spacing of 3.5 Å and a FWHM of 0.5°, reflections are present and sharpen in intensity at 550°C. The serpentine (100,020) reflection is present and followed by a poorly-defined reflection between 19.5 and 22° (2θ) interpreted to represent interlayer disorder. The serpentine (201) reflection is visible beginning to be expressed at ~34° (2θ). Glycerol solvation produced a greatly diminished pattern due to error in preparation and ethylene glycol solvation produced no noticeable change to the pattern.

3.1.4 Sample 4

Sample 4 (Fig. 3.4) consists entirely of serpentine. The serpentine (002) reflection, with a d-spacing of 7.3 Å and a FWHM of 0.4°, collapses almost entirely at 550°C. At 550°C, a broad 14.7 Å reflection at 6° (2θ) appears. The serpentine (020,100) reflection has a two-dimensional diffraction band indicating a degree of disorder. The serpentine (004) reflection, with a d-spacing of 3.7 Å and a FWHM of 0.4° collapses almost entirely with the (002) reflection. The (201) reflection is partially present beginning at ~34° (2θ). Error in preparation in glycerol solvation produced a pattern with diminished intensity and a poorly-defined reflection leading up to the serpentine (100,020) reflection. Ethylene glycol solvation produced no change indicating the absence of expandable phases.

3.1.5 Sample 5

Sample 5 (Fig. 3.5) is largely composed of a mixture of quartz with minor talc-like and serpentine phases, given the relative intensities. The intensity of talc (001) reflection, with a d-spacing of 9.7 Å and a FWHM of 1.3°, does not change significantly with heating. The serpentine (002) reflection, with a d-spacing of 7.2 Å and a FWHM of 0.3°, appears to have collapsed at 350°C, although the quality of the pattern may be diminished due to a height discrepancy where reflections were not properly detected (this also occurred in sample 7's ethylene glycol run). The serpentine (002) reflection and the (004) reflection, with a d-spacing of 3.6 Å and a FWHM of 0.5°, collapse entirely at 550 °C.

The talc (02,11) band is present indicating intralayer disordered stacking. The talc (021) reflection, with a d-spacing of 4.1 Å is visible as a shoulder off the quartz (100) reflection and becomes obscured by the (02,11) band upon heating. The talc (003) reflection, with a d-spacing of 3.2 Å and a FWHM of 1.6°, increases slightly in intensity and position as a function of increasing crystallinity. The talc (13,20) band and serpentine (201) reflection are visible beginning ~34° (2θ). Glycerol solvation produced poorly-defined reflections leading up to the talc (02,11). Ethylene glycol solvation produced no change in the pattern indicating the absence of expandable phases.

3.1.6 Sample 6

Sample 6 (Fig. 3.6) is composed entirely of serpentine. The serpentine (002), with a d-spacing of 7.2 Å and a FWHM of 0.4°, and (004), with a d-spacing of 3.6 Å and a FWHM of 0.5°, reflections do not collapse at 550 °C. The serpentine (020,100) reflection possesses a two-

dimensional diffraction band, indicating disorder and the serpentine (201) reflection begins to form at ~34° (2θ). Upon glycerol solvation, reflections with d-spacings ranging from 22 to 27 Å appear in the 3.2 to 4° (2θ) range. These reflections are not visible in the ethylene glycol solvation nor in the heat treated samples; they likely represent small amounts of interstratified smectite-like material.

3.1.7 Sample 7

Sample 7 (Fig. 3.7) appears to be entirely serpentine. The serpentine (002), with a d-spacing of 7.2 Å and a FWHM of 0.6°, and (004), with a d-spacing of 3.6 Å and a FWHM of 0.5°, reflections sharpen significantly in intensity at 350 °C as a result of increasing crystallinity before collapsing entirely at 550 °C. A broad 14.2 Å reflection appears at 6.5° (2θ) when heated to 550 °C.

The serpentine (020,100) reflection has a two-dimensional diffraction band indicating disorder and the beginning of the serpentine (201) reflection is visible at ~34° (2θ). The serpentine (002) reflection in the glycerol run is more intense than in the untreated run likely due to it being a separately prepared slide. The ethylene glycol run was unsuccessful likely due to a height discrepancy associated with misaligning the sample in the diffractometer; it is included here for completion.

3.1.8 Sample 8

Sample 8 (Fig. 3.8) is composed entirely of serpentine. The serpentine (002), with a d-spacing of 7.5 Å and a FWHM of 0.4°, and (004), with a d-spacing of 3.7 Å and a FWHM of 0.5°, reflections persist at 550 °C. The serpentine (020,100) reflection is barely detectable but is

broad in nature and the beginning of the (201) reflection is visible at ~34° (2θ). Glycerol solvation produced diminished reflections due to error as well as a noticeable shift in the serpentine (002) reflection; however, this is likely due to a height discrepancy. The reflection shift occurring at 550 °C too is likely related to a height discrepancy as the entire pattern shifts.

3.1.9 Sample 9

Sample 9 (Fig. 3.9) is an extremely disordered, fine-grained mixture of talc-like and serpentine phases. The very broad talc (001) reflection, with a d-spacing of 9.2 Å and a FWHM of 1.8°, is nearly indistinguishable until 350 °C and increases significantly in intensity at 550 °C as it improves in crystallinity; this too happens with the talc (003) reflection, with a d-spacing of 3.1 Å and a FWHM of 3.1°. The serpentine (002) reflection, with a d-spacing of 7.4 Å and a FWHM of 0.5°, is not distinguishable until 550 °C where a small broad reflection appears. A very broad serpentine (004) reflection accompanies.

The broad reflection in the untreated sample beginning at ~19° (2θ) resolves upon heating into the talc (02,11) band with the quartz (100) and a 4.2 Å reflection, tentatively interpreted as the antigorite (710), overlapping it. At ~34° (2θ) the beginning of the talc (13,20) and serpentine (201) reflection are observed. Solvation with glycerol and ethylene glycol produced no significant change to the untreated pattern.

3.1.10 Sample 10

Sample 10 (Fig. 3.10) is comprised of very fine-grained talc and chlorite with serpentine. Only upon heating do the broad talc (001), with a d-spacing of 10.0 Å, and the chlorite (001), with a d-spacing of 14.2 Å, reflections become prominent. The serpentine (002), with a d-

spacing of 7.0 Å and a FWHM of 0.8°, and (004) (overlapped by the chlorite 004 reflection) reflections partially collapses when heated to 550°C The serpentine (201) reflection and talc (13,20) band begins to be expressed at ~34° (2θ). Neither glycerol nor ethylene glycol solvation produced any significant pattern shifts.

Minor amounts of enstatite and hornblende are also present; their reflections improve in crystallinity upon heating. The increased prominence of enstatite and hornblende reflections in the glycerol pattern is due to this slide being prepared separately.

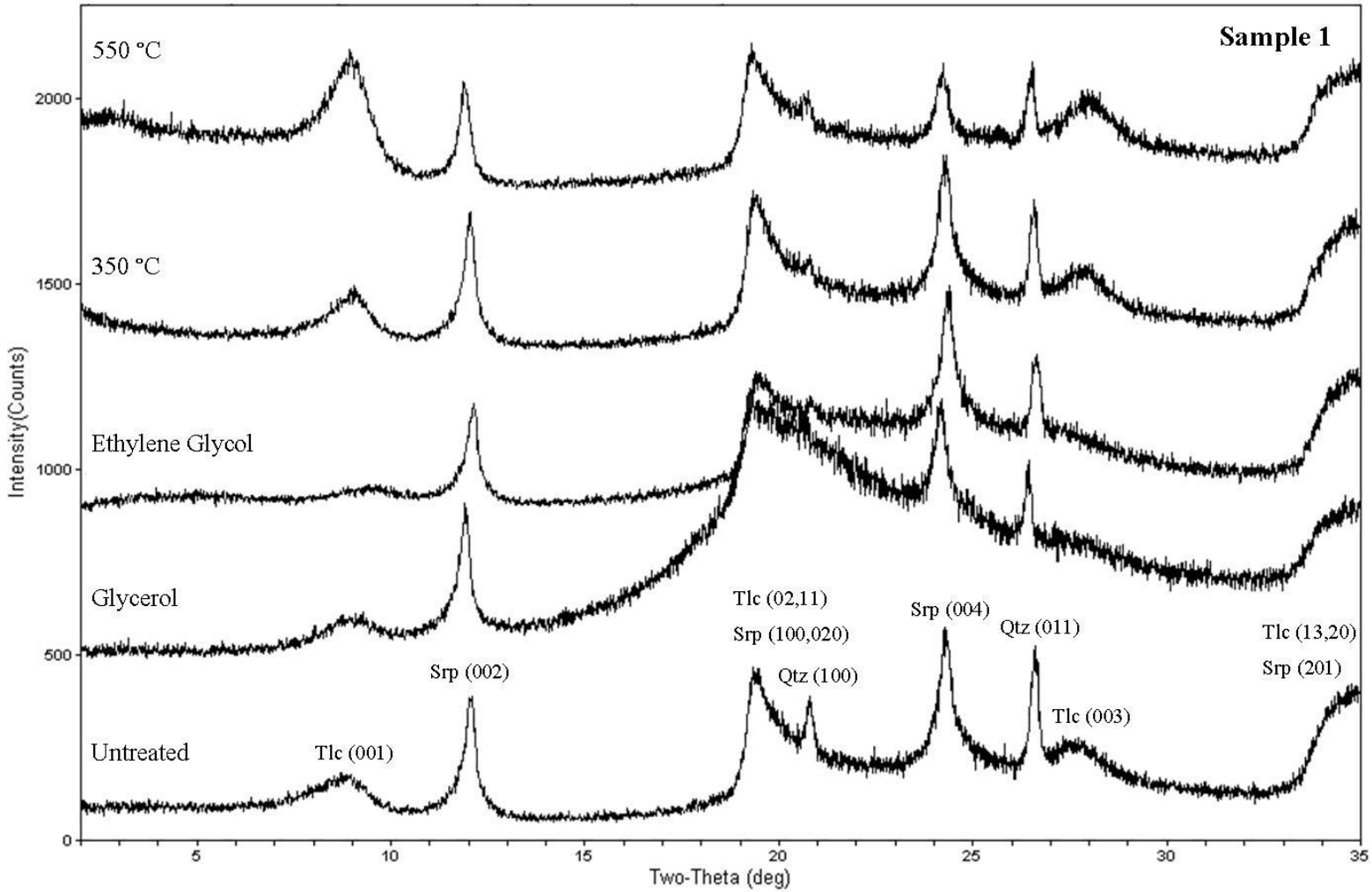

Figure 3.1 XRD patterns (Cu-Kα) of powder mounts of sample 1 untreated and air dried, solvated with glycerol, solvated with ethylene glycol, heated to 350 °C, and heated to 550 °C. Patterns have been vertically offset for clarity. Mineral symbols follow recommendations by Kretz (1983): Tlc = talc, Srp = serpentine, and Qtz = Quartz.

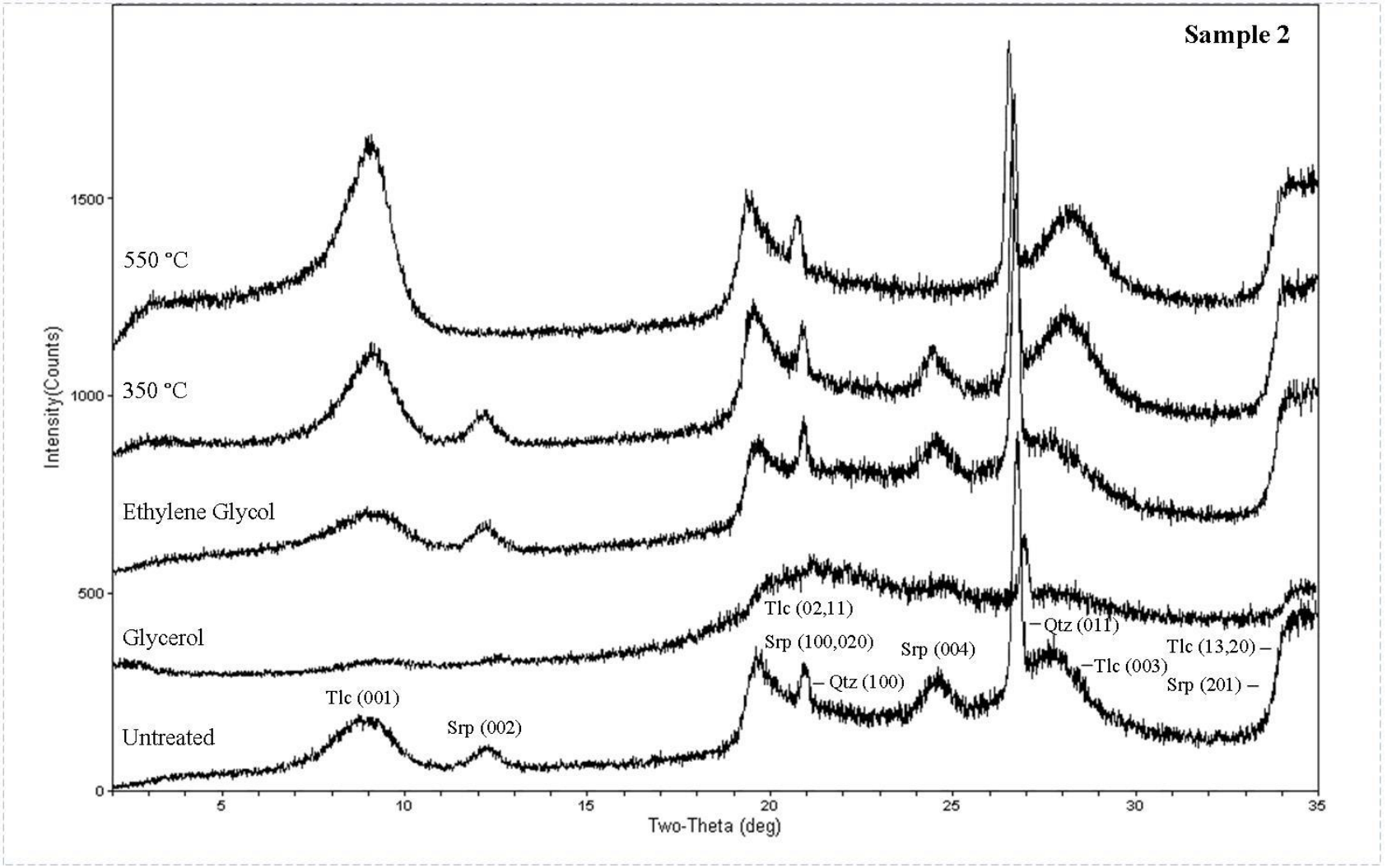

Figure 3.2 XRD patterns (Cu-Kα) of powder mounts of sample 2 untreated and air dried, solvated with glycerol, solvated with ethylene glycol, heated to 350 °C, and heated to 550 °C. Patterns have been vertically offset for clarity. Mineral symbols follow recommendations by Kretz (1983): Tlc = talc, Srp = serpentine, and Qtz = Quartz.

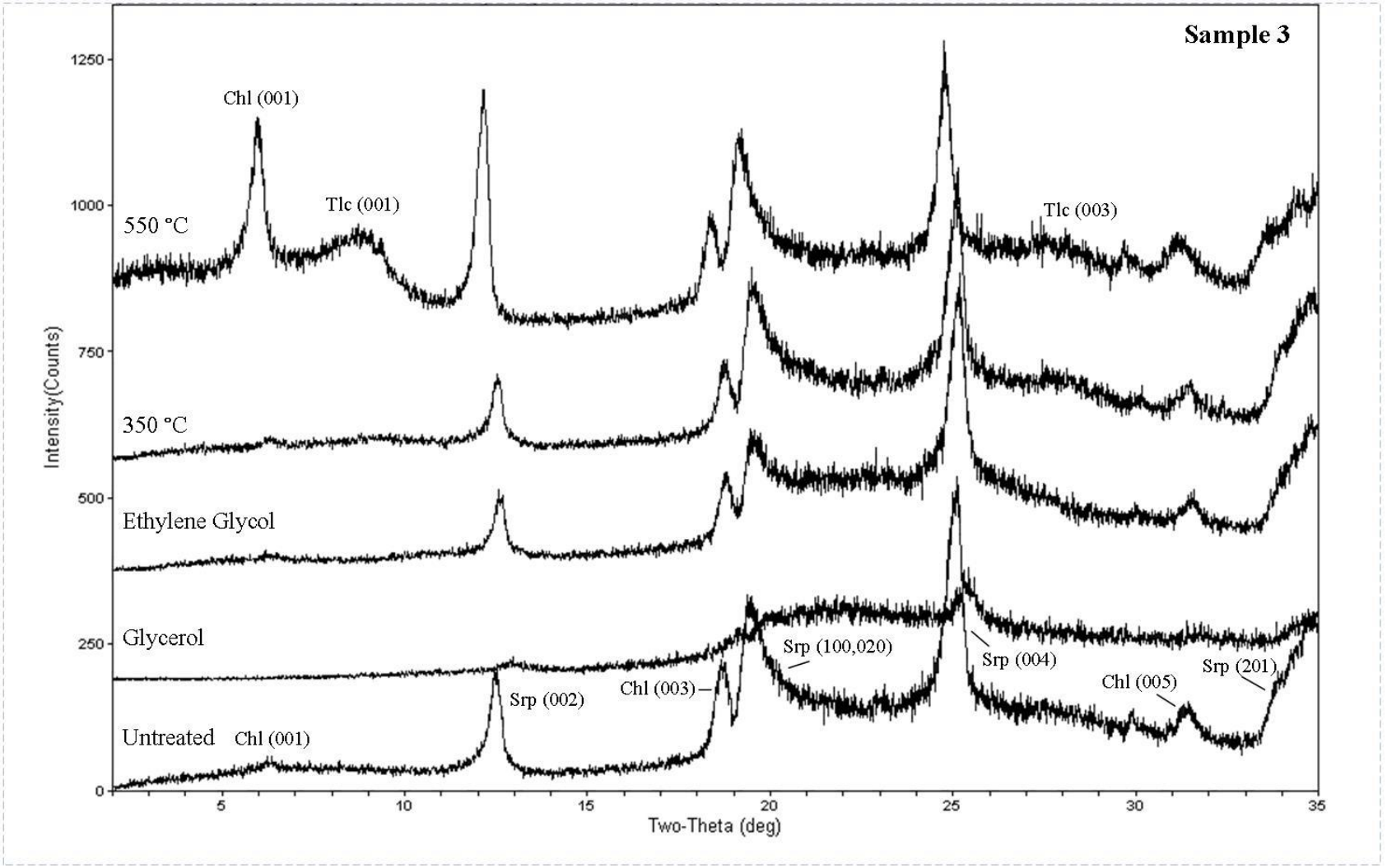

Figure 3.3 XRD patterns (Cu-Kα) of powder mounts of sample 3 untreated and air dried, solvated with glycerol, solvated with ethylene glycol, heated to 350 °C, and heated to 550 °C. Patterns have been vertically offset for clarity. Mineral symbols follow recommendations by Kretz (1983): Tlc = talc, Srp = serpentine, and Chl = chlorite.

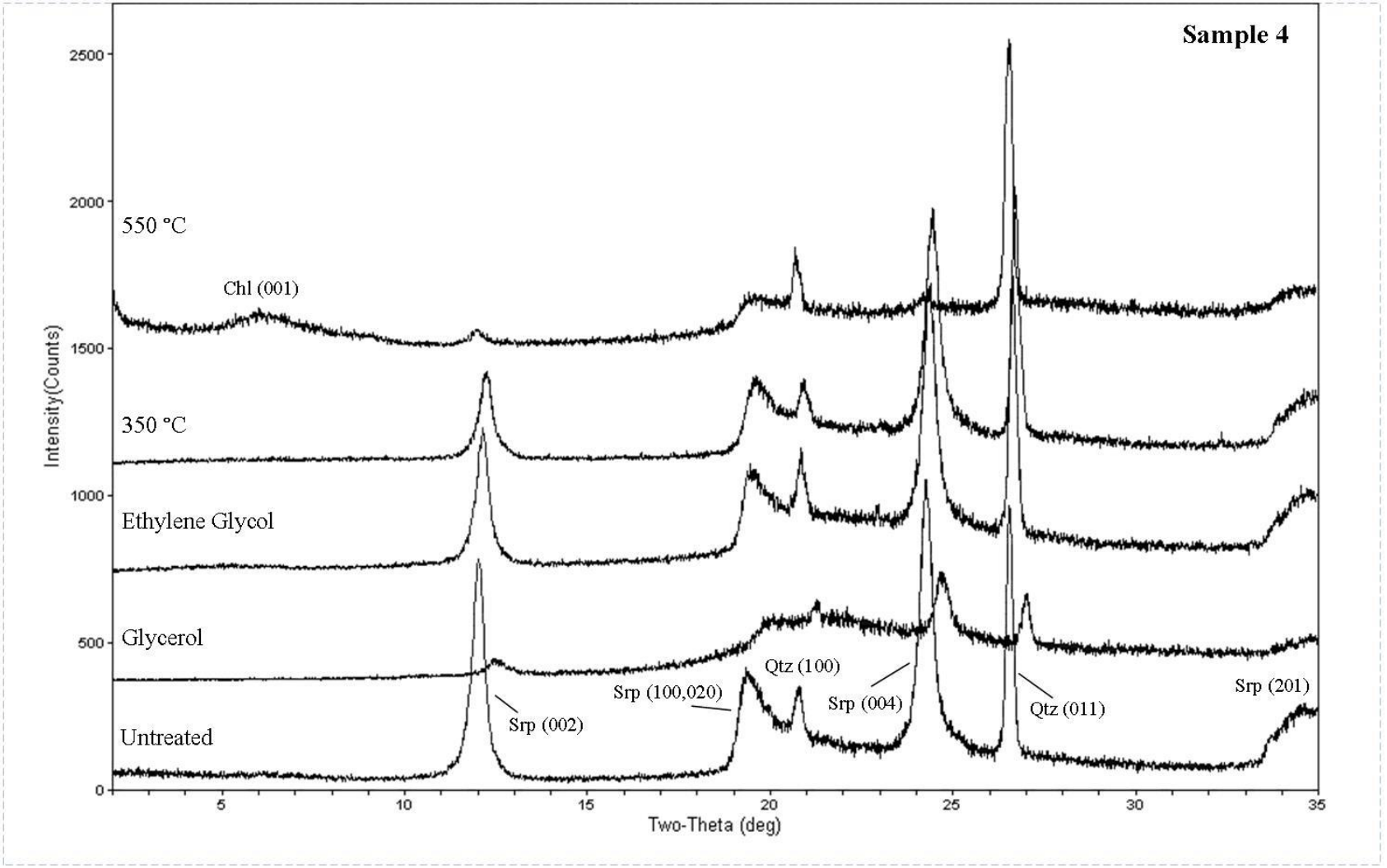

Figure 3.4 XRD patterns (Cu-Kα) of powder mounts of sample 4 untreated and air dried, solvated with glycerol, solvated with ethylene glycol, heated to 350 °C, and heated to 550 °C. Patterns have been vertically offset for clarity. Mineral symbols follow recommendations by Kretz (1983): Tlc = talc, Srp = serpentine, Chl = chlorite. and Qtz = Quartz.

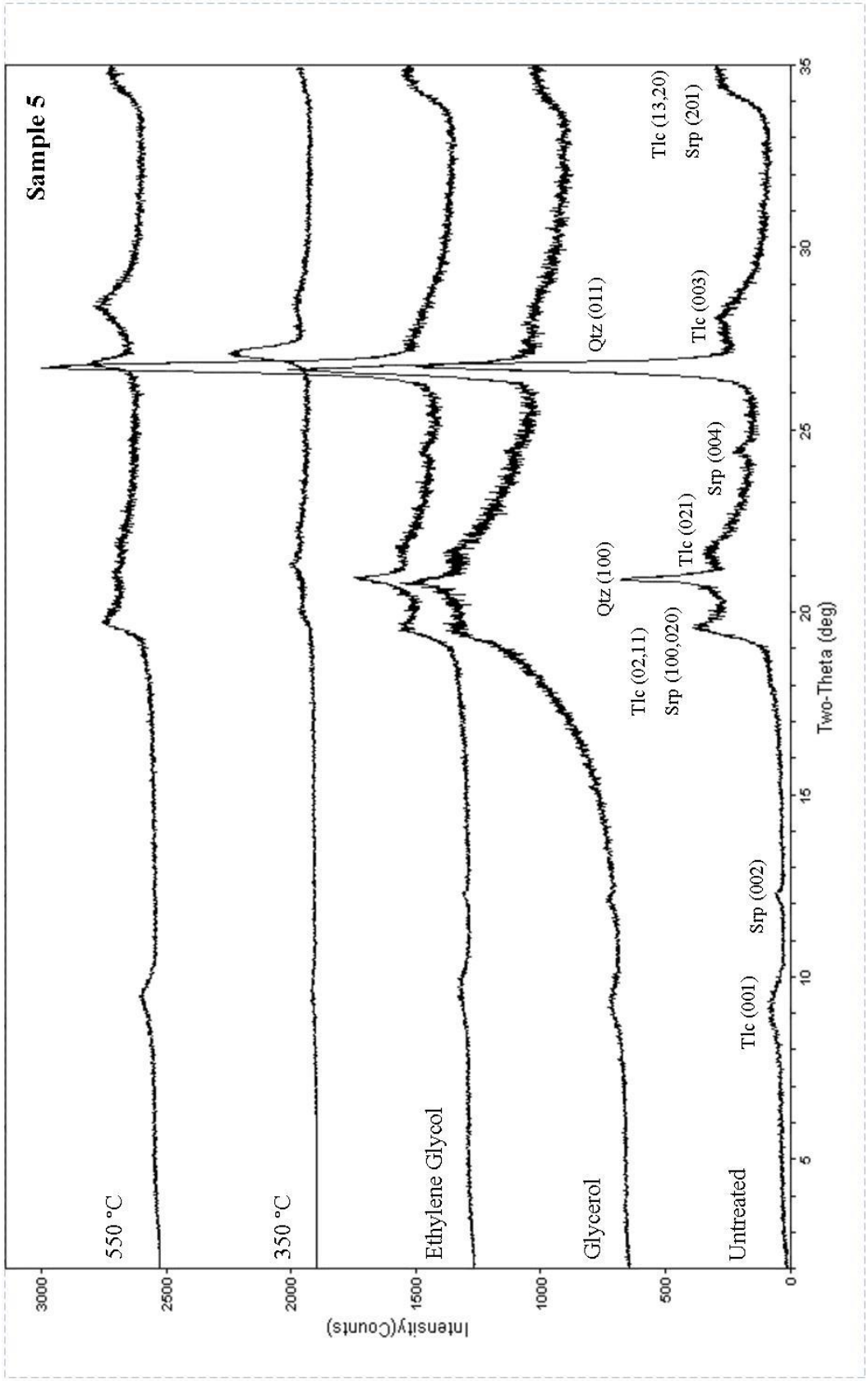

Figure 3.5 XRD patterns (Cu-Kα) of powder mounts of sample 5 untreated and air dried, solvated with glycerol, solvated with ethylene glycol, heated to 350 °C, and heated to 550 °C. Patterns have been vertically offset for clarity. Mineral symbols follow recommendations by Kretz (1983): Tlc = talc, Srp = serpentine, and Qtz = Quartz.

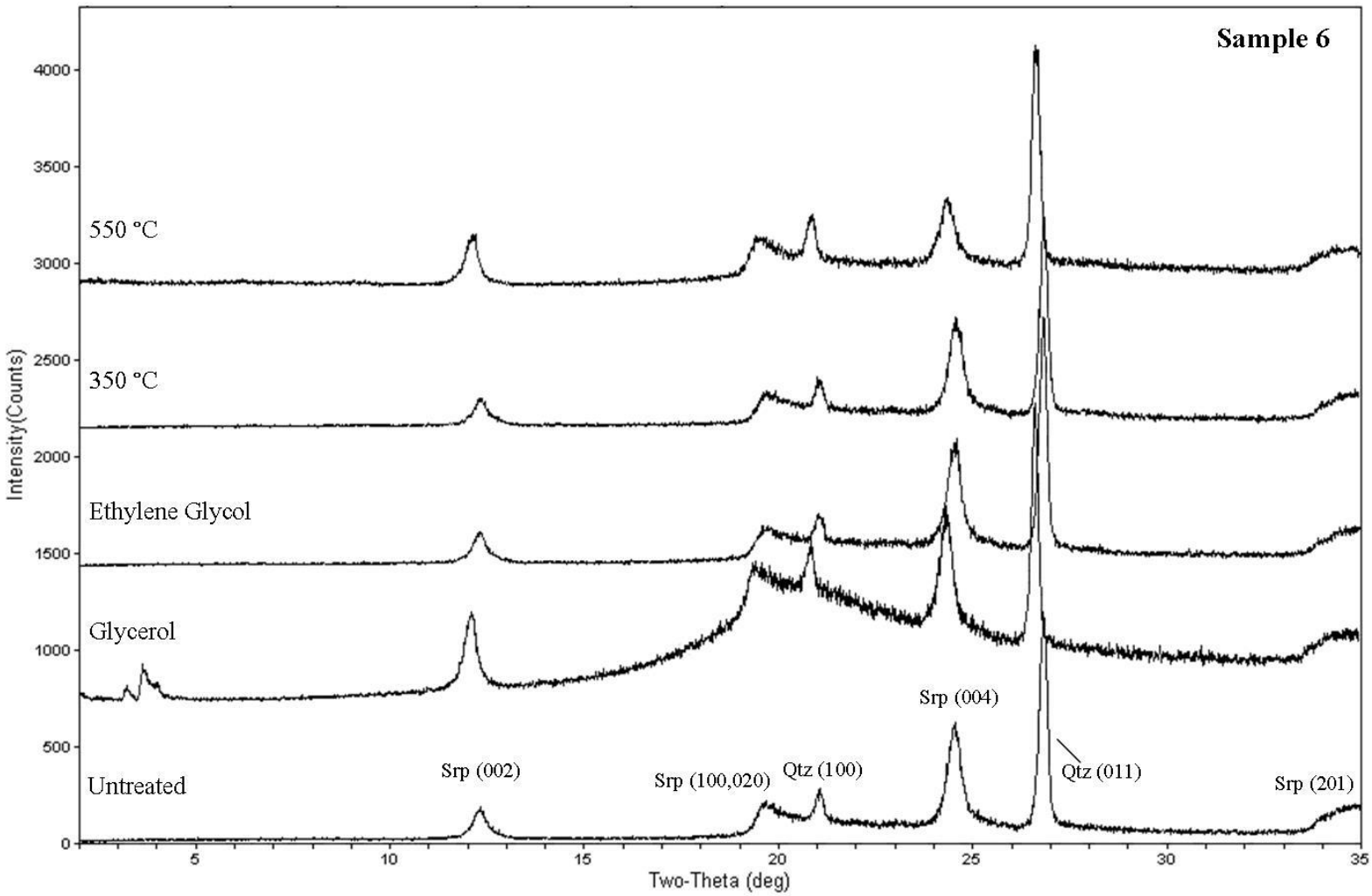

Figure 3.6 XRD patterns (Cu-Kα) of powder mounts of sample 6 untreated and air dried, solvated with glycerol, solvated with ethylene glycol, heated to 350 °C, and heated to 550 °C. Patterns have been vertically offset for clarity. Mineral symbols follow recommendations by Kretz (1983): Srp = serpentine and Qtz = Quartz.

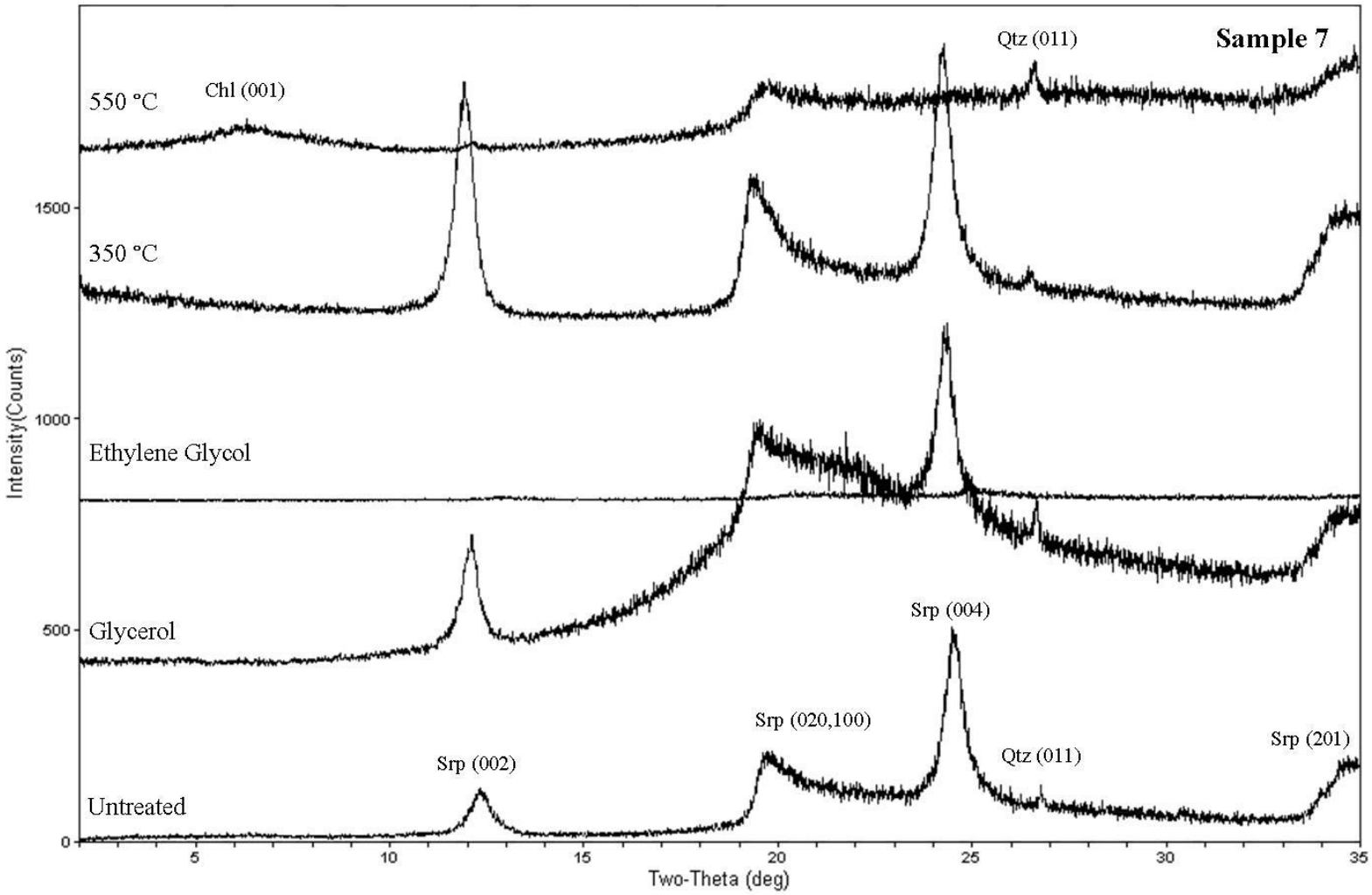

Figure 3.7 XRD patterns (Cu-Kα) of powder mounts of sample 7 untreated and air dried, solvated with glycerol, solvated with ethylene glycol, heated to 350 °C, and heated to 550 °C. Patterns have been vertically offset for clarity. Mineral symbols follow recommendations by Kretz (1983): Tlc = talc, Srp = serpentine, Chl = chlorite, and Qtz = Quartz.

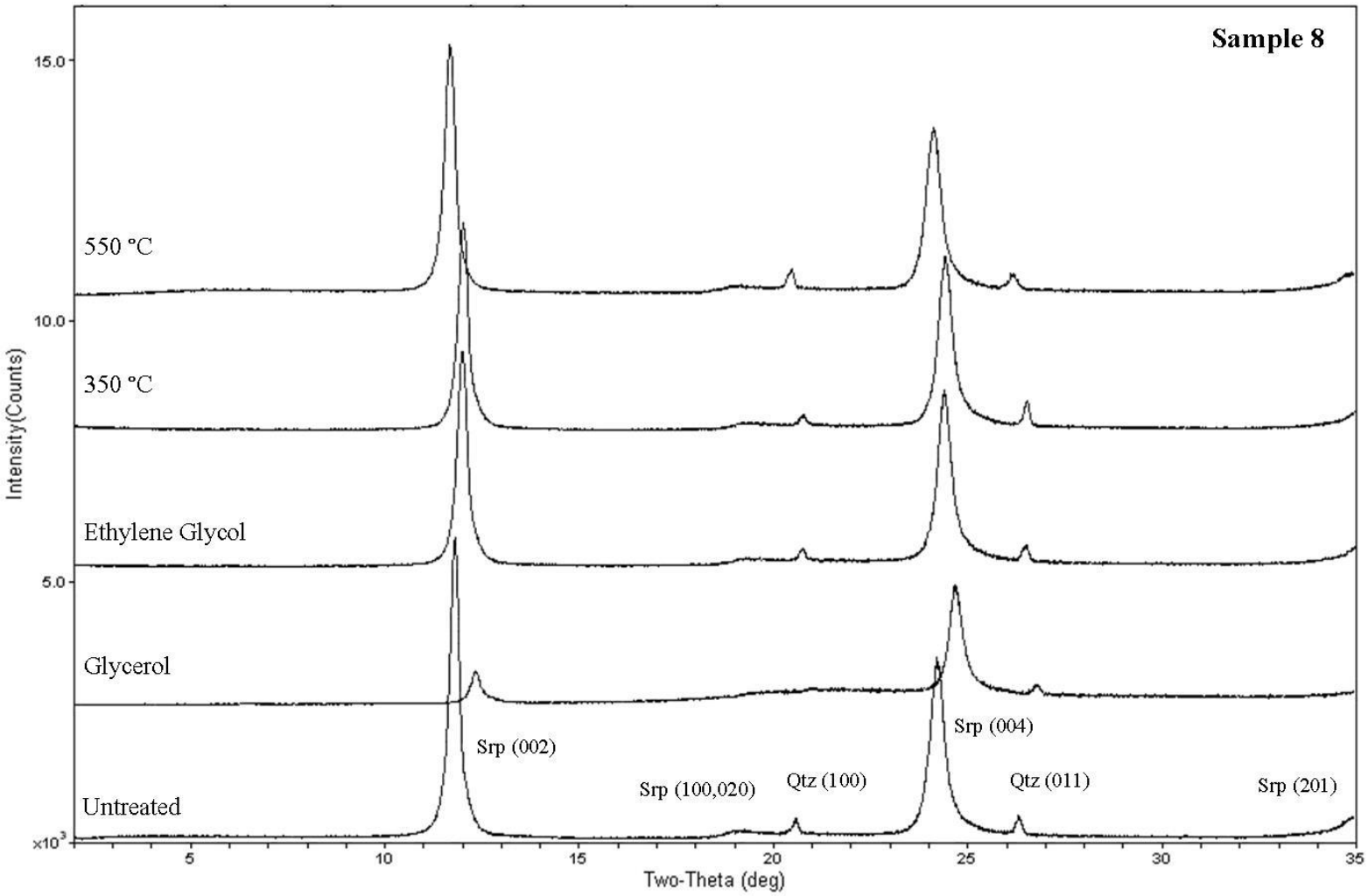

Figure 3.8 XRD patterns (Cu-Kα) of powder mounts of sample 8 untreated and air dried, solvated with glycerol, solvated with ethylene glycol, heated to 350 °C, and heated to 550 °C. Patterns have been vertically offset for clarity. Mineral symbols follow recommendations by Kretz (1983): Srp = serpentine and Qtz = Quartz

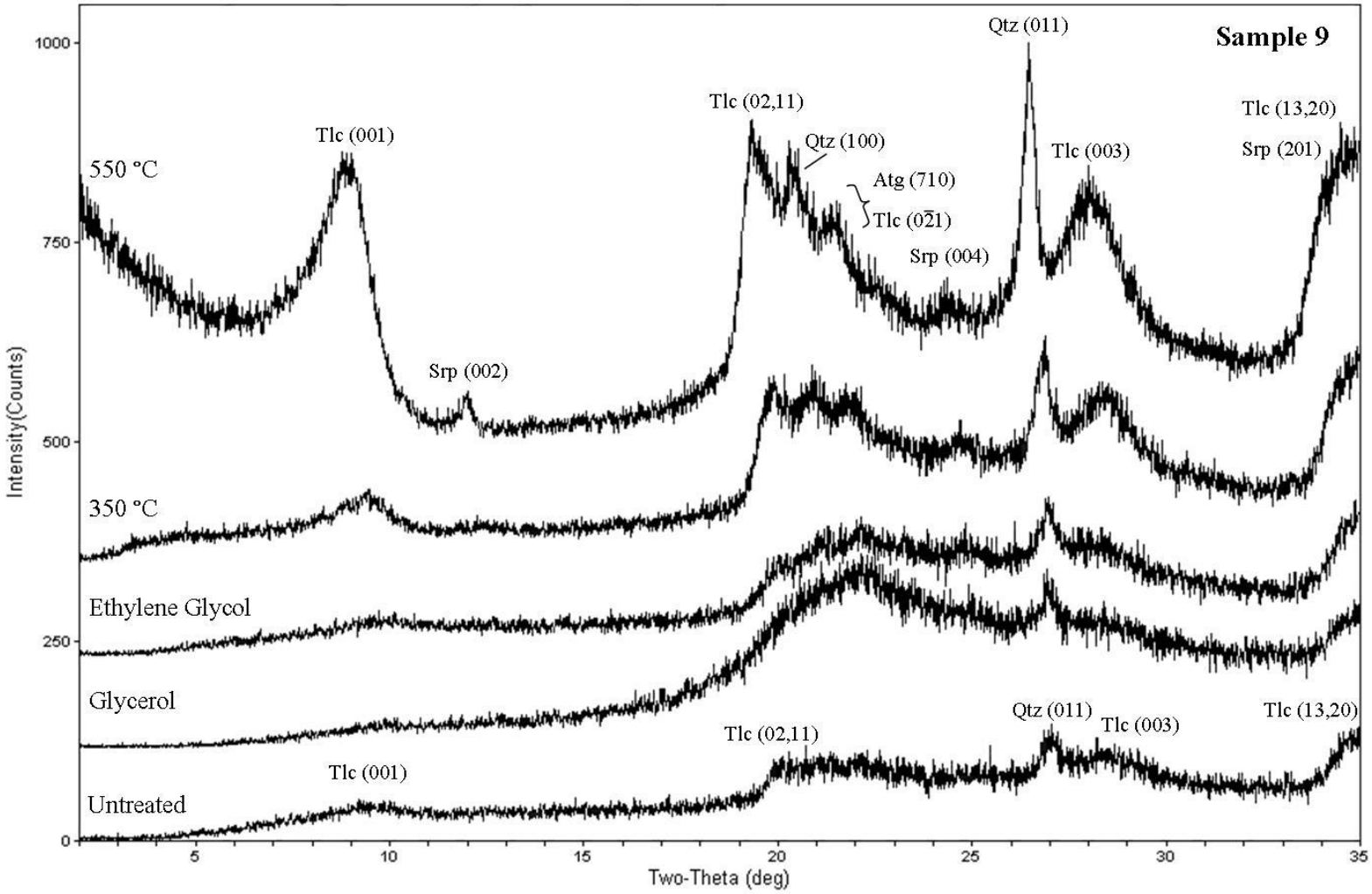

Figure 3.9 XRD patterns (Cu-Kα) of powder mounts of sample 9 untreated and air dried, solvated with glycerol, solvated with ethylene glycol, heated to 350 °C, and heated to 550 °C. Patterns have been vertically offset for clarity. Mineral symbols follow recommendations by Kretz (1983): Tlc = talc, Srp = serpentine, Atg = antigorite and Qtz = Quartz.

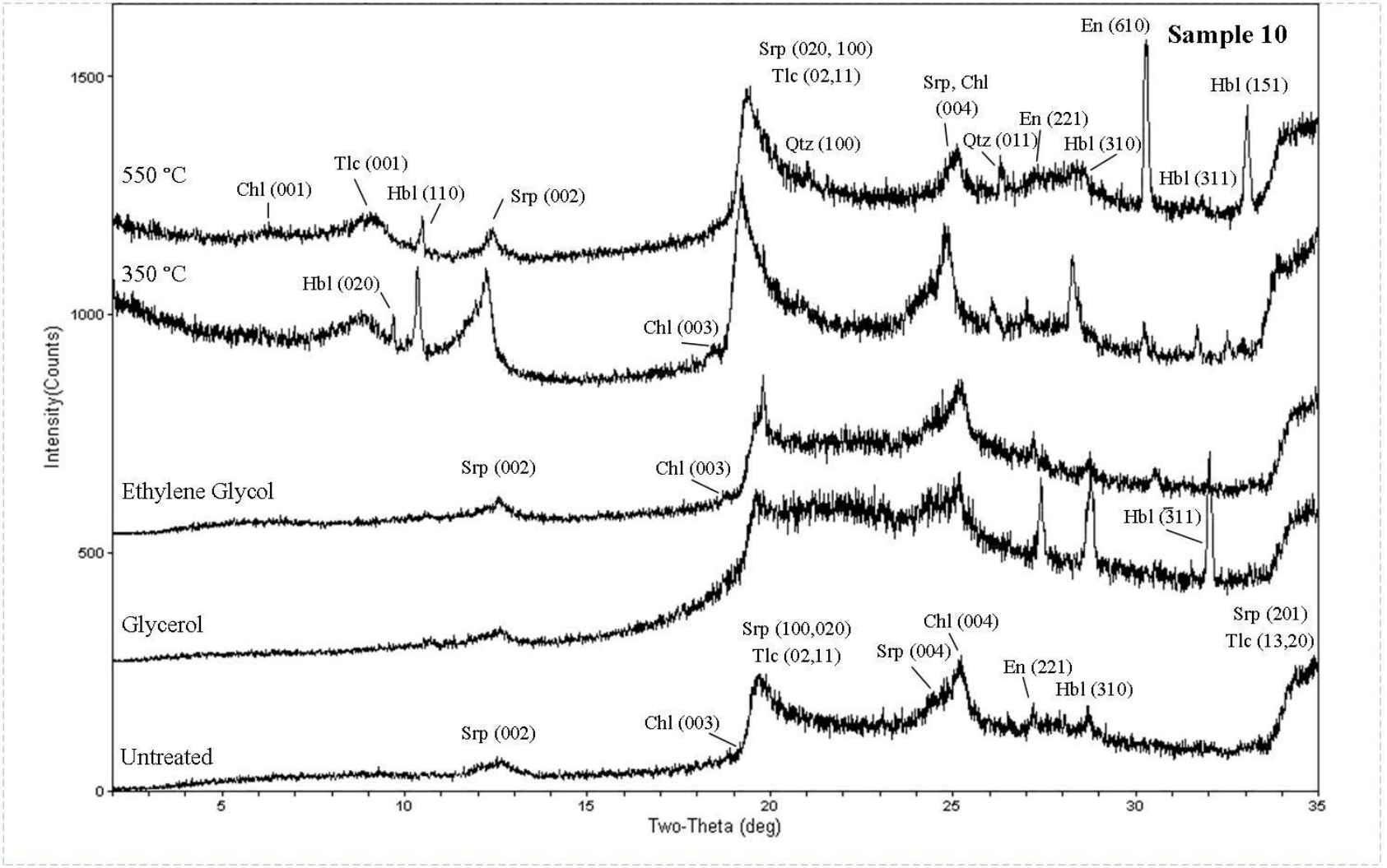

Figure 3.10 XRD patterns (Cu-Kα) of powder mounts of sample 10 untreated and air dried, solvated with glycerol, solvated with ethylene glycol, heated to 350 °C, and heated to 550 °C. Patterns have been vertically offset for clarity. Mineral symbols follow recommendations by Kretz (1983): Tlc = talc, Srp = serpentine, Chl = Chlorite, En = Enstatite, Hbl = Hornblende, and Qtz = Quartz.

3.2 Transmission Electron Microscopy

3.2.1 Sample 1

Sample 1 is comprised of pseudo-lamellar platy aggregates of Ni-rich phyllosilicates, amorphous silica and silver nanoparticles. The phyllosilicates are the dominant texture observed comprising approximately 90% with the amorphous silica and silver nanoparticles comprising 5% and 5%, respectively.

Figure 3.11a shows the general texture of the aggregated phyllosilicate particles. Individual particles vary 50 to 70 nm long and 10 to 30 nm wide. The d-spacing of the lattice fringes is approximately 10 Å and is corroborated by fast Fourier transforms (FFT) of the images; SAED patterns were not obtained owing to beam damage. Pinch-out discontinuities, observed in approximately 80% of the regions examined, were observed to occur over lengths of 5 to 10 nm with 3 to 5 lattices displaced (Fig. 3.11b-c). Lattice curvature was observed in approximately 50% of the particles and was continuous through entire particles, lending quasi-braided textures to aggregates (Fig. 3.11d-e). Regions of continuous lattices were also observed (Fig. 3.11f). These phyllosilicates are comprised of Si, O, Ni, and Mg with minor Cl and S; the approximate peak ratios are consistent with a talc-like mineral. The Ni content is significant however Mg is dominant in 90% of the areas examined. Normalized EDS spot analysis of a region high in Ni shows 21% Ni, 18% Mg, 16% O, and 45% Si (Fig. 3.12); the oxygen percentage is low due to considerable beam-damage by the time analysis was done, which partially dehydrates the sample.

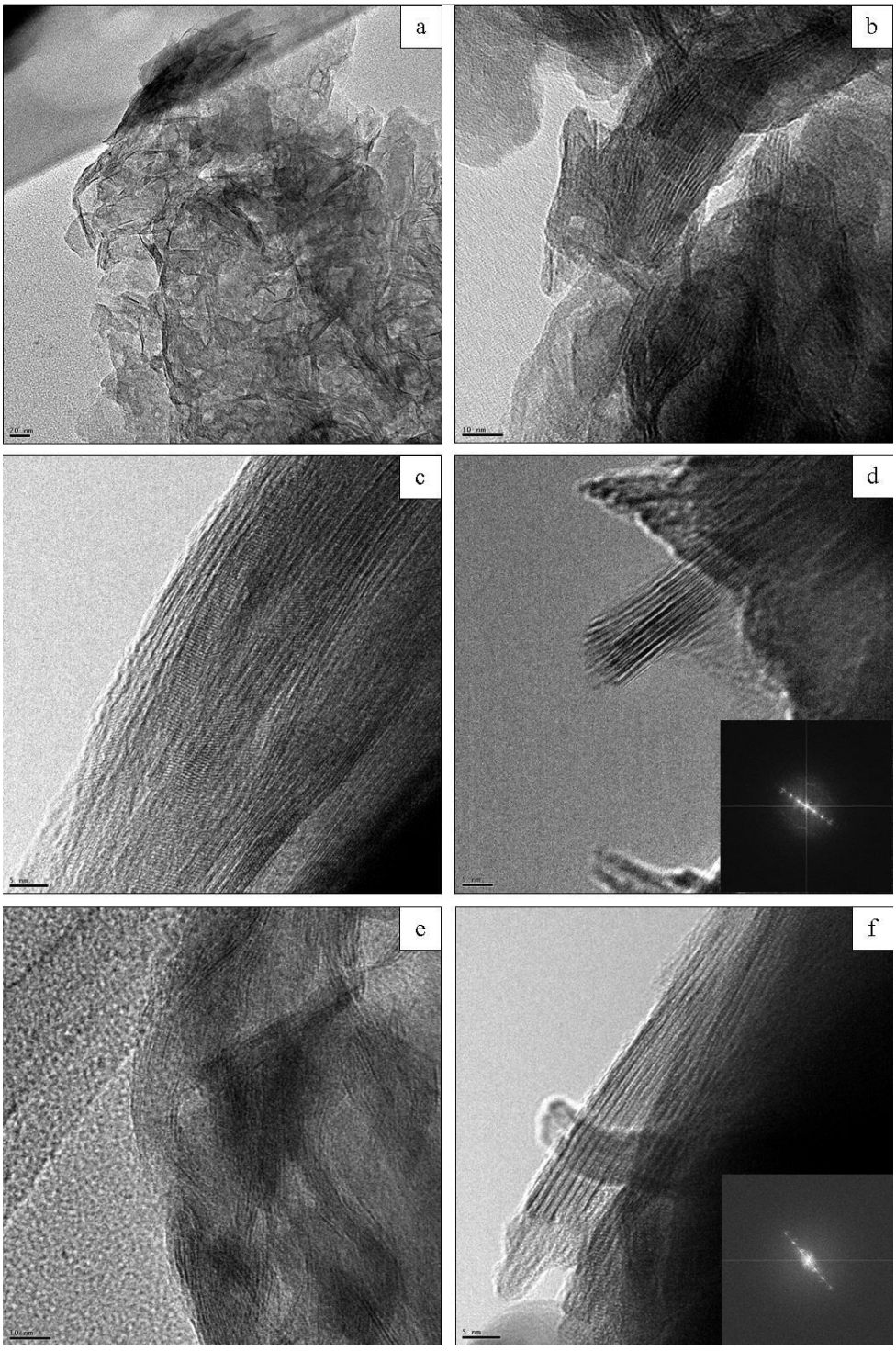

Figure 3.11 TEM brightfield images of Ni-phyllosilicates in sample 1. Image contrast has been altered to improve relief. **(a)** General aggregated texture of the particles. **(b-c)** Regions displaying lattice pinch-outs. **(d)** Lattices diverging at a 30° angle toward particle termination; Inset: Reduced FFT: $d_{(001)}$ = 10.19 Å, $d_{(002)}$ = 5.184 Å, $d_{(003)}$ = 3.408 Å. **(e)** Region showing quasi-braided texture. **(f)** A region of continuous lattices; Inset: Reduced FFT: $d_{(001)}$ = 10.35 Å, $d_{(002)}$ = 5.024 Å, $d_{(003)}$ = 3.181 Å.

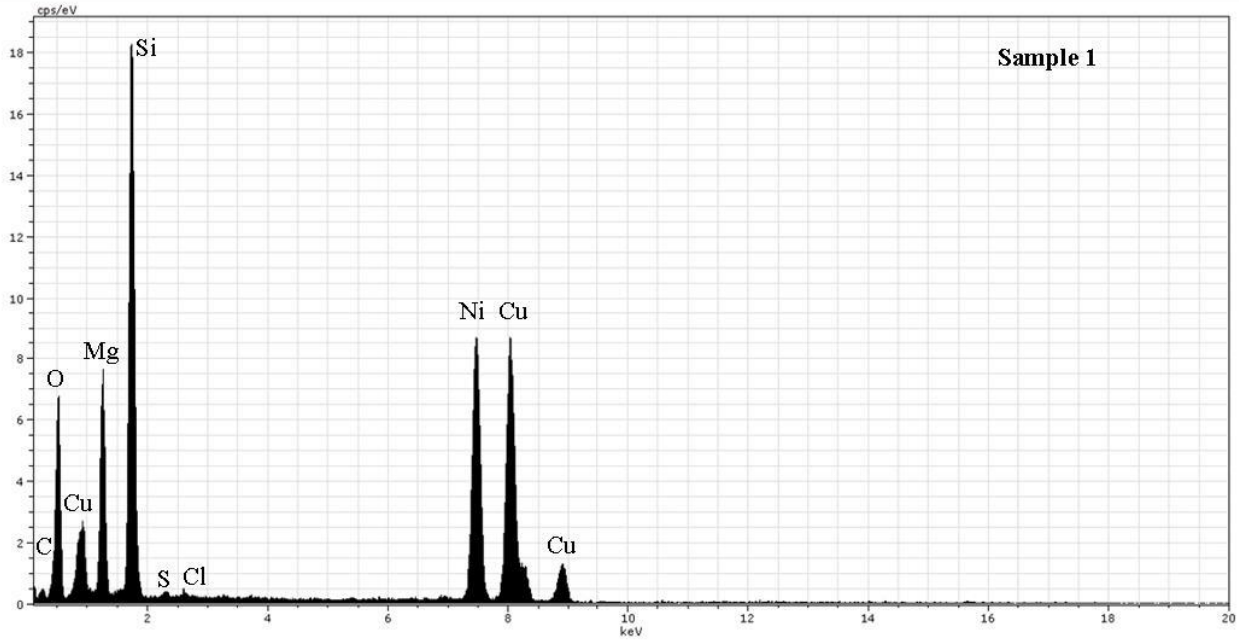

Figure 3.12 EDS spectra of Ni-rich phyllosilicates in sample 1. The spot analysis shown corresponds with Figure 3.11f.

Approximately 20% of the amorphous silica texture forms porous, anastomosing networks of spherules 5 to 40 nm in diameter that are not found in association with other phases (Fig. 3.13a-b). The pores in this texture are irregular in shape, not well-connected, and commonly 50 nm in diameter. This phase is interpreted to represent opal or chalcedony. The other 80% of amorphous silica is associated with Ag-rich nanoparticles.

The Ag-rich nanoparticles are common in certain regions of the sample, locally comprising 10 to 30% of the sample volume and are dispersed in a matrix of amorphous silica (Fig. 3.13c-f). The Ag-rich nanoparticle textures vary in diameter from approximately 5 to 10 nm and are near spherical to irregular oblate in morphology with internal linear features that are interpreted as twin planes, likely on [111]. These nanoparticles commonly aggregate, with textures consistent with Ostwald ripening. The d-spacing of reflections ($d_{(111)}$ = 2.319 Å, $d_{(200)}$ =

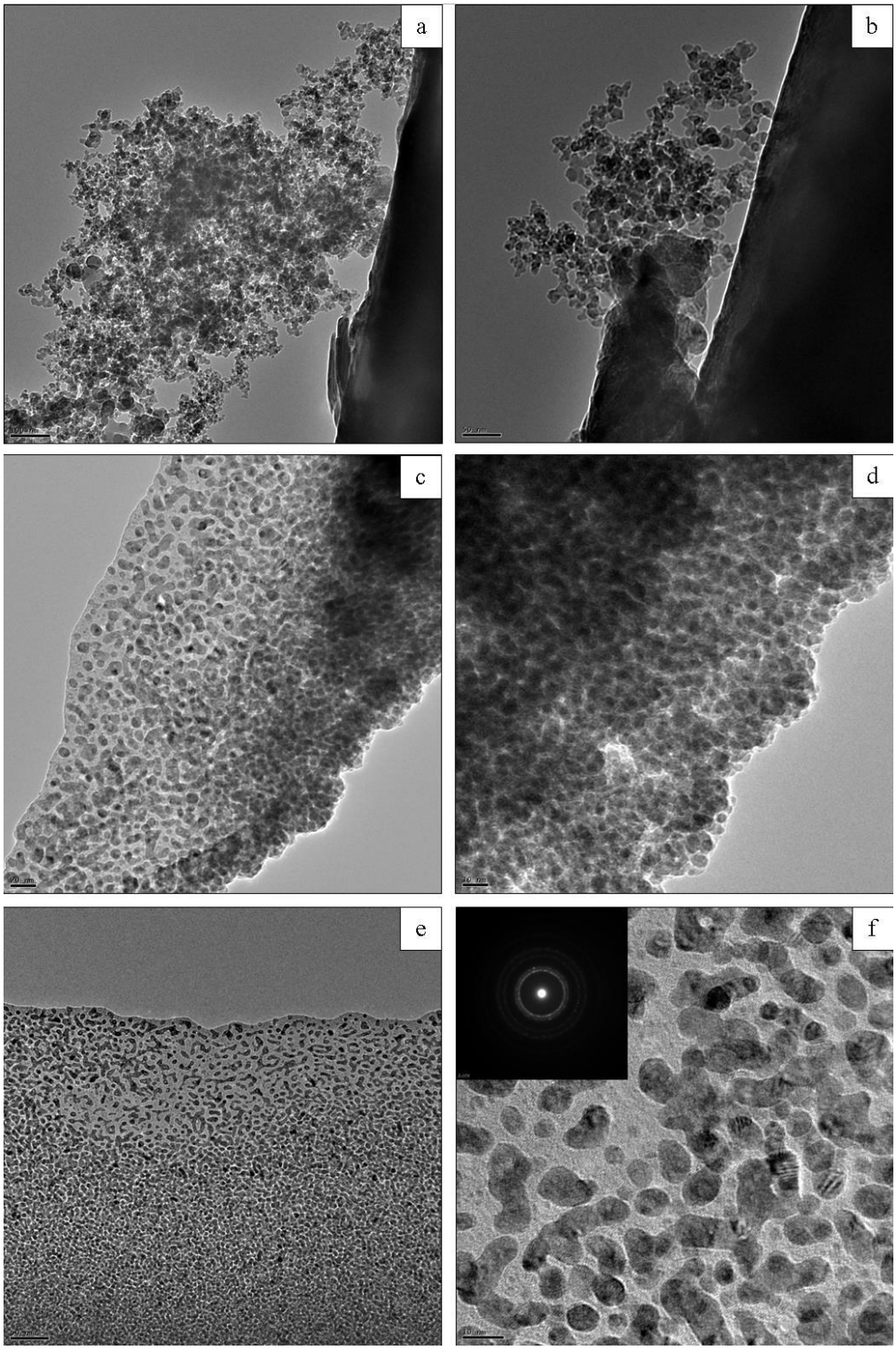

Figure 3.13 TEM brightfield images of amorphous silica and Ag-rich nanoparticles in sample 1. **(a-b)** Regions bearing anastomosing networks of amorphous silica. **(c-f)** Regions showing Ag-rich nanoparticles; Inset (f): SAED pattern of multiple particles.

2.005 Å, $d_{(220)}$ = 1.391 Å, and $d_{(311)}$ = 1.186 Å) as measured from the SAED patterns of regions of Ag-nanoparticles agree well with published values for silver (Wyckoff, 1963; Novgorodova et al., 1981).

3.2.2 Sample 2

Sample 2 is comprised entirely of pseudo-lamellar platy aggregates of Ni-rich phyllosilicates (Fig. 3.14a). There is ubiquitous evidence of turbostratic stacking present. Pinch-out structures are present within approximately 75% of the sample and are observed to occur over lengths of 10 to 15 nm with 1 to 5 lattices displaced (Fig. 3.14b-d). Lattice curvature was observed in 90% of the particles and was continuous through entire particles, lending quasi-braided textures to aggregates (Fig. 3.14e-f).

EDS spot analysis of the phyllosilicates show they are comprised of Si, O, Ni, and Mg with minor Ca and Fe, consistent with a talc-like mineral. In all regions analyzed, Ni-content greatly exceeds Mg-content with normalized EDS spot analysis showing 33% Ni, 7% Mg, 46% Si, and 14% O (Fig. 3.15).

3.2.3 Sample 3

Sample 3 is composed of approximately 50% chlorite, 40% antigorite and 10% talc-like mineral. The chlorite and talc-like phases occur together as aggregates of platy pseudo-curving, pseudo-lamellar particles. The particles themselves, which are an average of 100 nm in length, do not curve upon close inspection (Fig. 3.16a). The chlorite particles have a d-spacing of 14 to 14.5 Å with largely continuous lattices (Fig. 3.16b-d). EDS spot analyses of chlorite-bearing

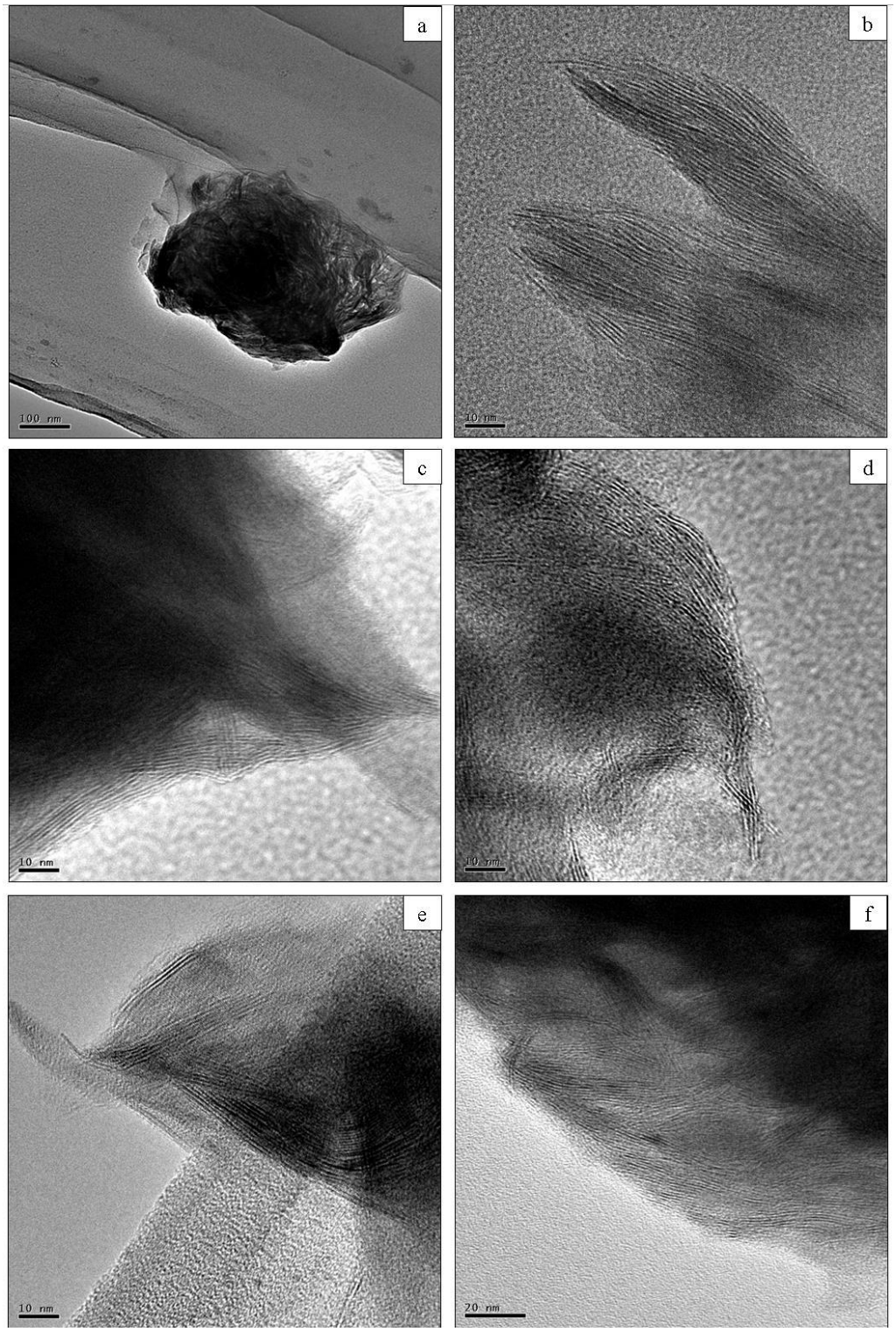

Figure 3.14 TEM brightfield images of Ni-rich phyllosilicates in sample 2. Image contrast has been altered to improve relief. **(a)** General aggregated texture of the particles. **(b-d)** Regions of lattices with 10 Å d-spacing showing lattice pinch-outs. **(e-f)** Regions showing lattice curvature and quasi-braided textures.

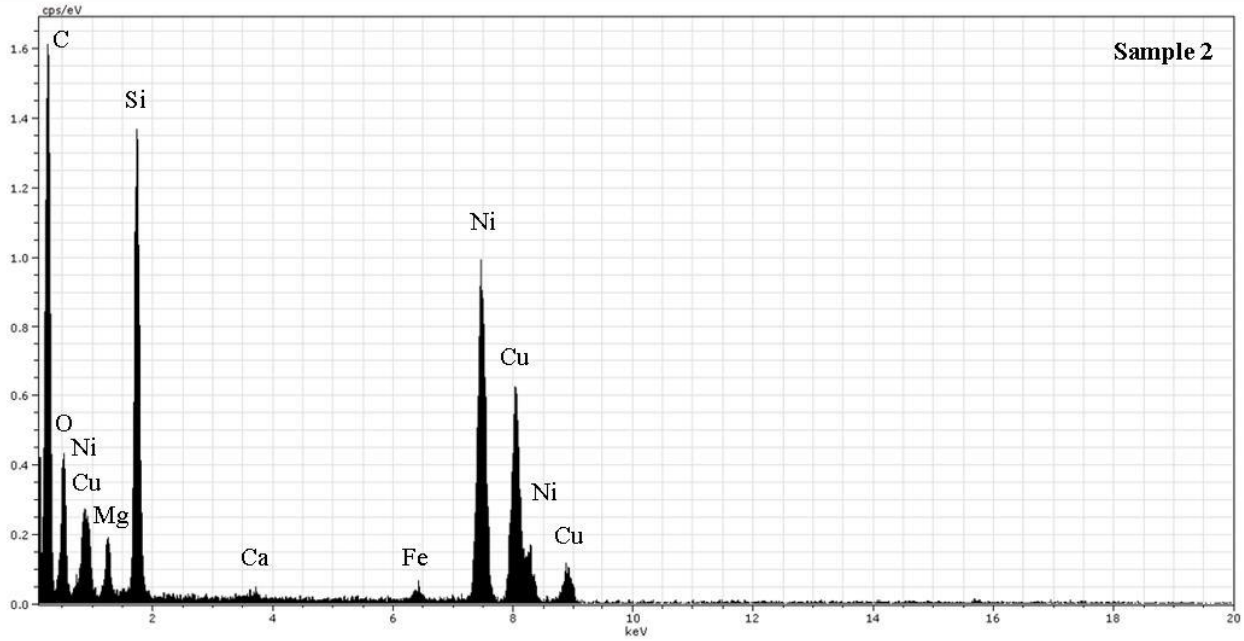

Figure 3.15 EDS spectra of Ni-rich phyllosilicates in sample 2. The spot analysis shown corresponds with Figure 3.14b.

regions show them to be comprised of O, Si, Mg, Ni, Al, and Fe with minor Cr and Au, consistent with a chlorite mineral. Normalized EDS spot analysis of a chlorite-bearing region had 39% O, 27% Si, 19% Mg, 6% Al, 5% Ni, and 4% Fe (Fig. 3.17).

Unlike the chlorite, the talc-like phases display a great degree of crystallographic disorder in all regions observed with lattice pinch-outs that extend an average of 10 nm and displace 1-2 lattices (Fig. 3.16e). Indeed, many of the regions are degraded and poor in crystallinity, making high resolution images of lattices difficult to obtain. EDS spot analyses of talc-bearing regions show them to be comprised of O, Si, Mg, Ni, and Al, consistent with a talc-like mineral. Normalized spot analysis of a region bearing talc-like phases had 38% O, 33% Si, 20% Mg, 7% Ni, and 2% Al (Fig. 3.18).

The chlorite and talc-like phases are never observed interstratified, however, a region of continuous lattices with a d-spacing of 5 Å was observed within a chlorite-bearing region (Fig.

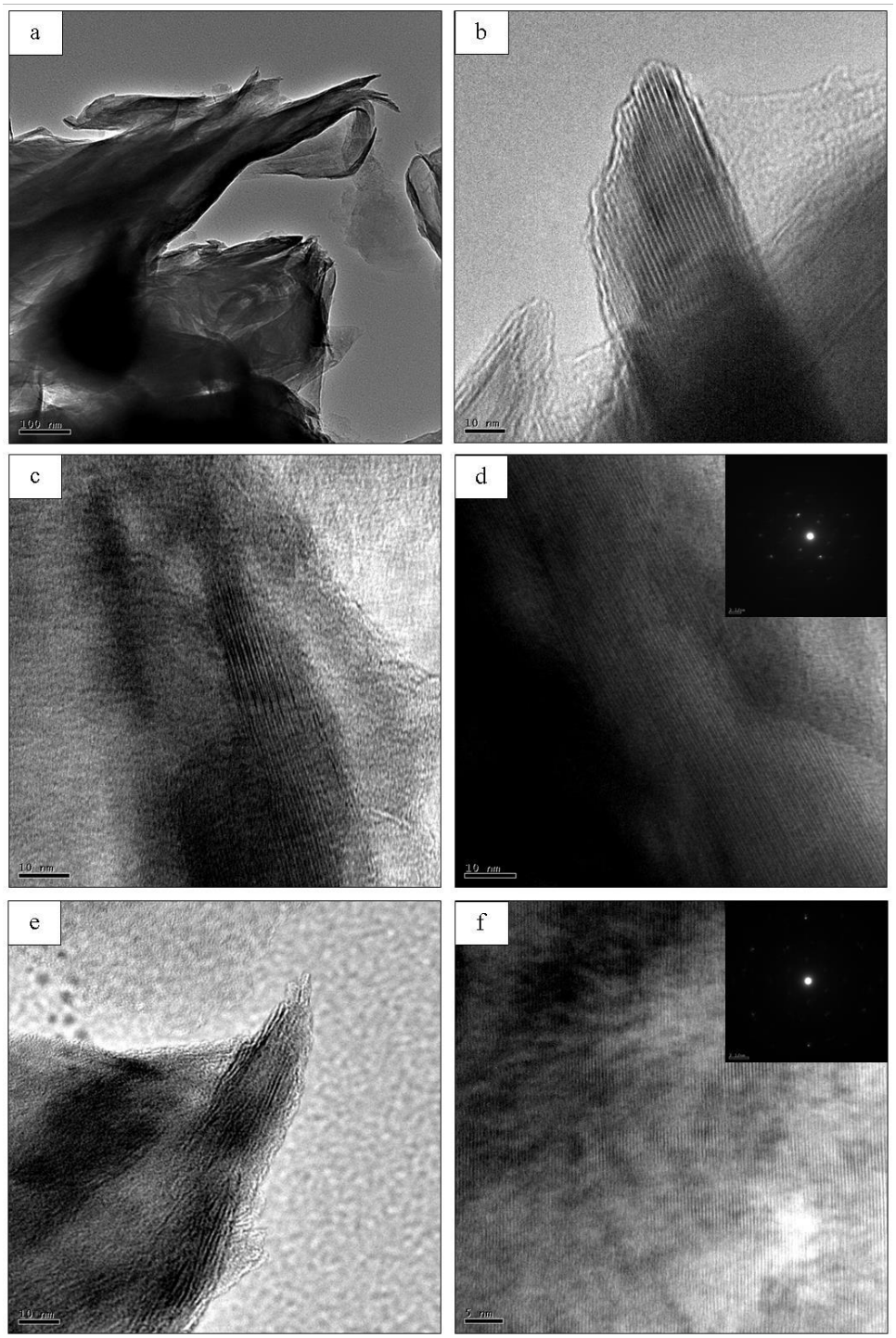

Figure 3.16 TEM brightfield images of regions being chlorite and a talc-like mineral. Image contrast has been altered to improve relief. **(a)** General texture of the aggregates of platy, pseudo-lamellar particles. **(b-d)** Regions of continuous lattices with 14 to 14.5 Å d-spacing interpreted as chlorite. **(e)** A talc-like particle with pinch-out textures. **(f)** Region of continuous lattices with 5 Å d-spacing; Inset: SAED pattern of the region, showing hexagonal closest packing.

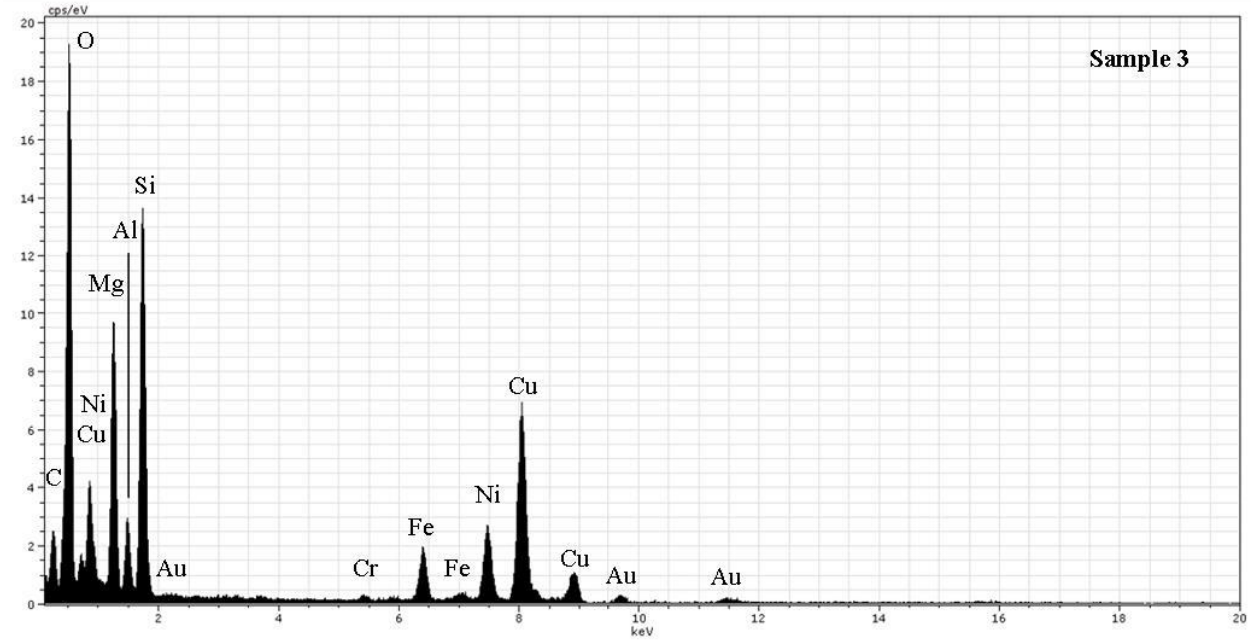

Figure 3.17 EDS spectra of a chlorite-bearing region in sample 3. The spot analysis shown corresponds with Figure 3.16c.

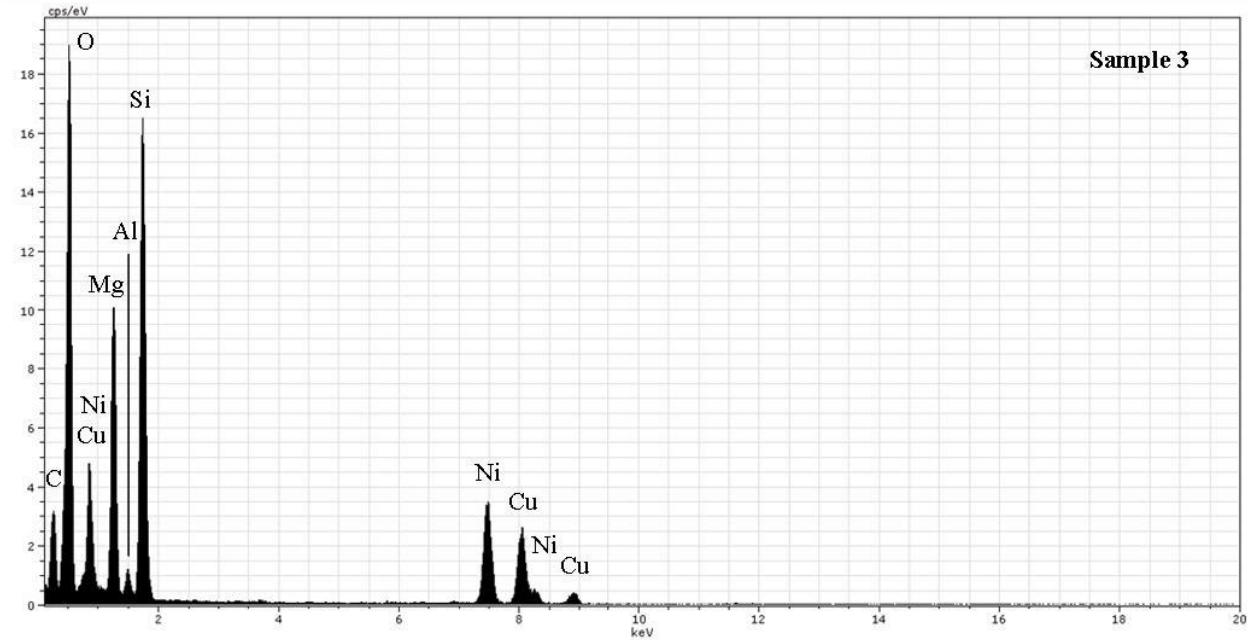

Figure 3.18 EDS spectra of a region bearing talc-like phases in sample 3. The spot analysis shown corresponds with Figure 3.16e.

3.16f). The 5 Å lattice spacing is consistent with two times the thickness of a normal (001) talc spacing and thus may be the (002), observed because of local thickness and chemical

composition variation. A more complex interstratification scheme may also explain the 5 Å lattice spacing where brucite like layers or other oxyhydroxide layer or layers may exist. High resolution images of these regions and were not possible owing to beam damage.

Antigorite occurs separately from the other phases in platy regions possessing no apparent curvature (Fig. 3.19a). Antigorite crystals have a platy morphology with a characteristic corrugated texture on the surface of the crystal representing modulations along the a-axis, similar to noted TEM images of antigorite (e.g. Da Costa et al. 2008; Wunder et al. 2001). Spacing of the modulations as expressed in the brightfield images are variable and are approximately 20 to 40 Å (Fig. 3.19b-e) in 90% of the regions observed with 10% of the regions showing 100 to 150 Å (Fig. 3.19f). EDS spot analyses of the antigorite-bearing regions show them to be comprised of O, Si, Mg, Al, and Fe with minor Ni, Cr, Mn, and Au. Normalized spot analysis of a region bearing antigorite has 37% O, 21% Si, 26% Mg, 10% Al, and 6% Fe; Ni is less than 1%.

3.2.4 Sample 4

Sample 4 is composed of chrysotile and lizardite with minor chlorite. Of the regions analyzed, chrysotile comprises approximately 55% with lizardite and chlorite comprising 35 and 5%, respectively. Also observed was a phase with 5 Å basal spacing, which comprised 5% of the regions examined.

Chrysotile occurs as disarticulated aggregates in 75% of the regions examined and 25% as packages of lineated or semi lineated nanofibers; both are represented in Figure 3.21a. Individual nanofibers vary 150 to 375 nm in length with the average being 225 nm in length, 20 to 60 nm in width with the average being 30 nm in width, 8 to 15 nm in internal pore space, and 6 to 9 nm in wall thicknesses. Figures 3.21b-c and 3.21d show lattice fringe detail of the

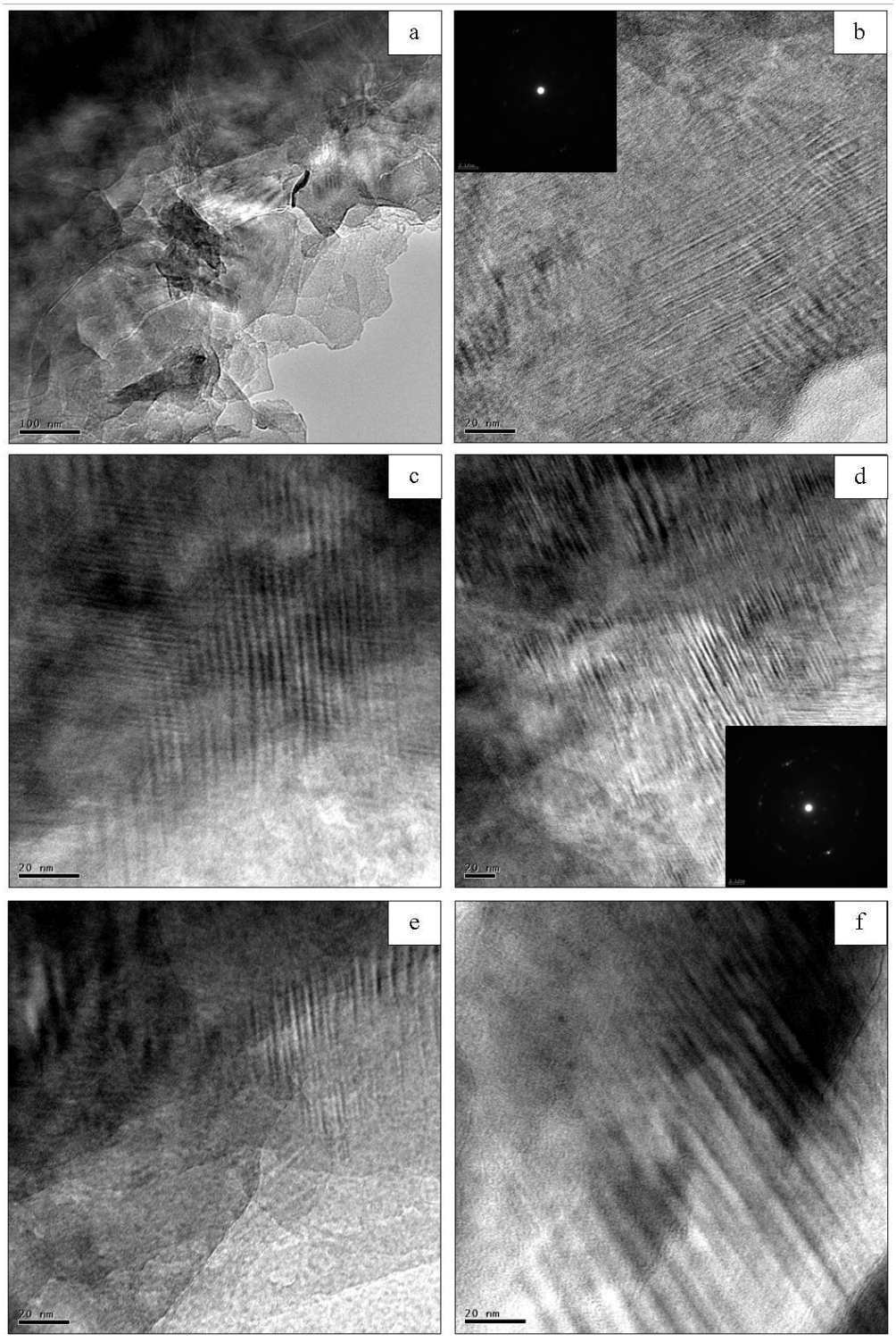

Figure 3.19 TEM brightfield images of antigorite-bearing regions in sample 3. Image contrast has been altered to improve relief. **(a)** General texture of the platy antigorite region. **(b-f)** Regions showing antigorite modulations of variable spacing; Inset SAED patterns (b and d) show hexagonal closest packing.

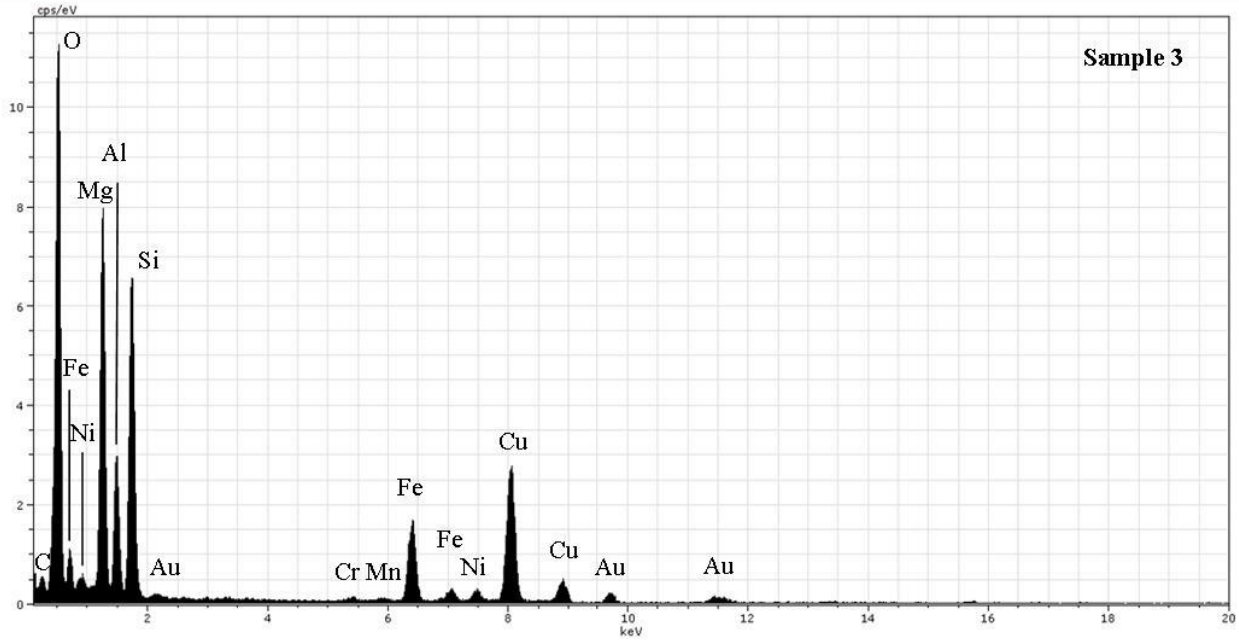

Figure 3.20 EDS spectra of an antigorite-bearing region in sample 3. The spot analysis shown corresponds with Figure 3.19b.

nanofibers perpendicular to and viewing down the fiber axis, respectively. The lattices are continuous and have an approximately 7 Å d-spacing. The chrysotile nanofibers are comprised of O, Si, Mg, Fe, Ni and minor Cl. The normalized spot analysis of a chrysotile-bearing region has 33% O, 27% Si, 28% Mg, 9% Fe, 2% Ni, and 1% Cl, consistent with a serpentine-like mineral (Fig. 3.22).

Chlorite is a minor phase, found in only one region examined. It occurs as aggregates of small, pseudo-lamellar platy crystals (Fig. 3.21e). The particle found was thick therefore lattice-imaging was difficult; however, areas at the particle edge showed lattices with 12 to 14 Å d-spacing. The lattices appear continuous and to have a significant curvature to them, however, detailed examination was not possible due to beam damage.

Lizardite occurs as platy regions within the chrysotile aggregates, comprising approximately 30% of the particle textures. The lizardite (Fig. 3.23a-d) has a basal spacing of

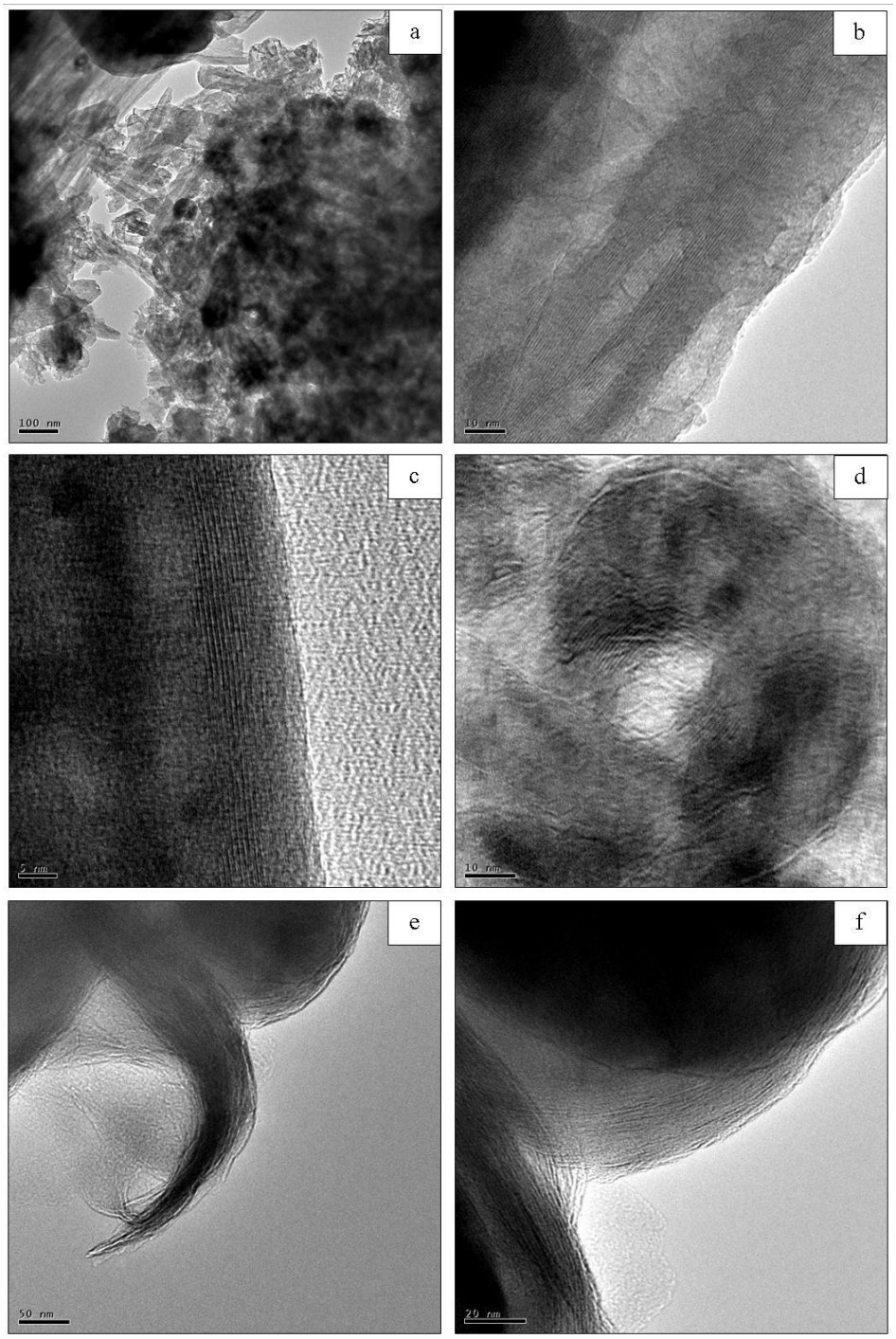

Figure 3.21 TEM brightfield images of chrysotile and chlorite bearing regions in sample 4. Image contrast has been altered to improve relief. **(a)** General texture of the lineated packages (upper left) and disarticulated aggregates (lower right) of the chrysotile nanofibers. **(b-c)** Lattice fringe images of chrysotile nanofibers as viewed perpendicular to the fiber axis. **(d)** Lattice fringe image of a chrysotile nanofibers viewing down the fiber axis. (e) General texture of a chlorite-bearing region. **(f)** Lattice fringe image of a region bearing chlorite.

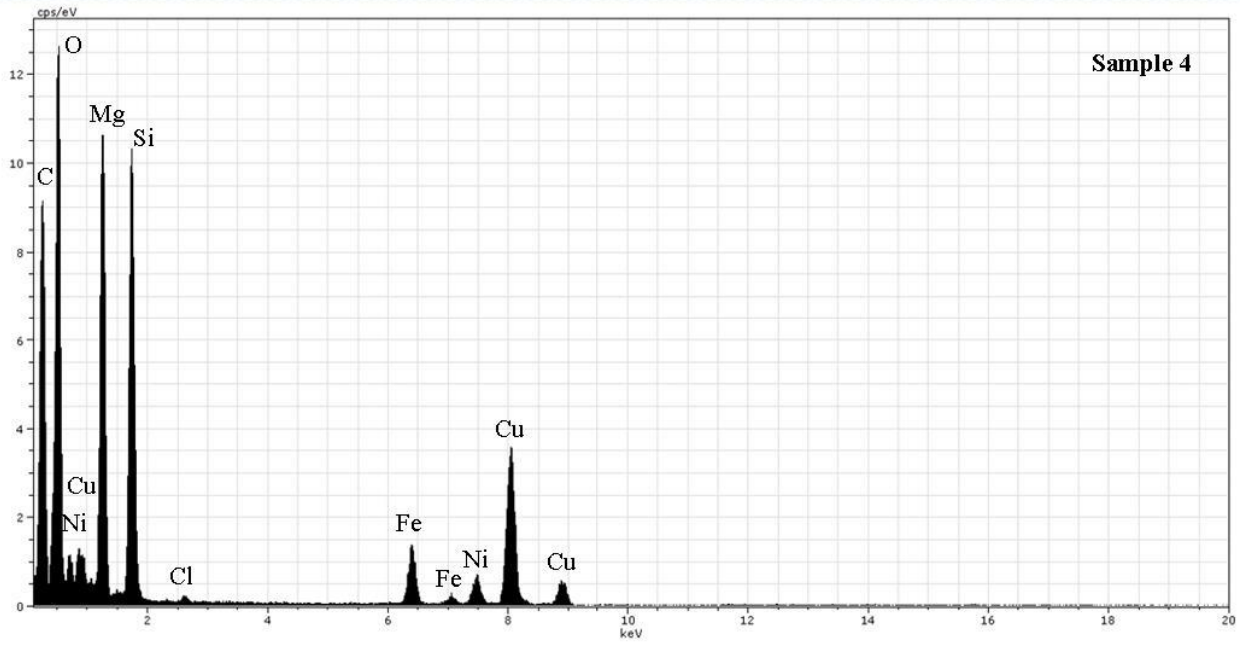

Figure 3.22 EDS spectra of a chrysotile-bearing region in sample 4. The spot analysis shown corresponds with Figure 3.21d.

approximately 7 Å as measured from the images and from SAED patterns collected from these regions, which show $d_{(002)}$ = 7.1 Å, $d_{(004)}$ = 3.6 Å, and $d_{(006)}$ = 2.4 Å (Fig. 3.23b - inset). All of the lizardite lattices are continuous, however, 25% of the regions examined contained lenticular layer separations defects in which two adjacent lattices diverge at 5 to 20° angles and reconvene 10 to 20 nm later, creating slit-shaped voids 2 to 5 nm wide in the crystal lattice (Fig.3.23a). The lizardite is comprised of O, Si, Mg, Fe, and trace Ni. The normalized EDS spot analysis of a lizardite-bearing region has 40% O, 25% Si, 32% Mg, 3% Fe, and <1% Ni (Fig. 3.24).

Found in association with the lizardite are particles that have 5 Å d-spacings (Fig 3.23 e-f). All of the lattices in these particles are continuous; however, they display a slight waviness. These regions may represent half of the normal thickness of a normal (001) talc spacing and thus may be the (002), observed because of local thickness and chemical composition variation. However, since talc-like phases were not observed elsewhere in the sample, an alternative

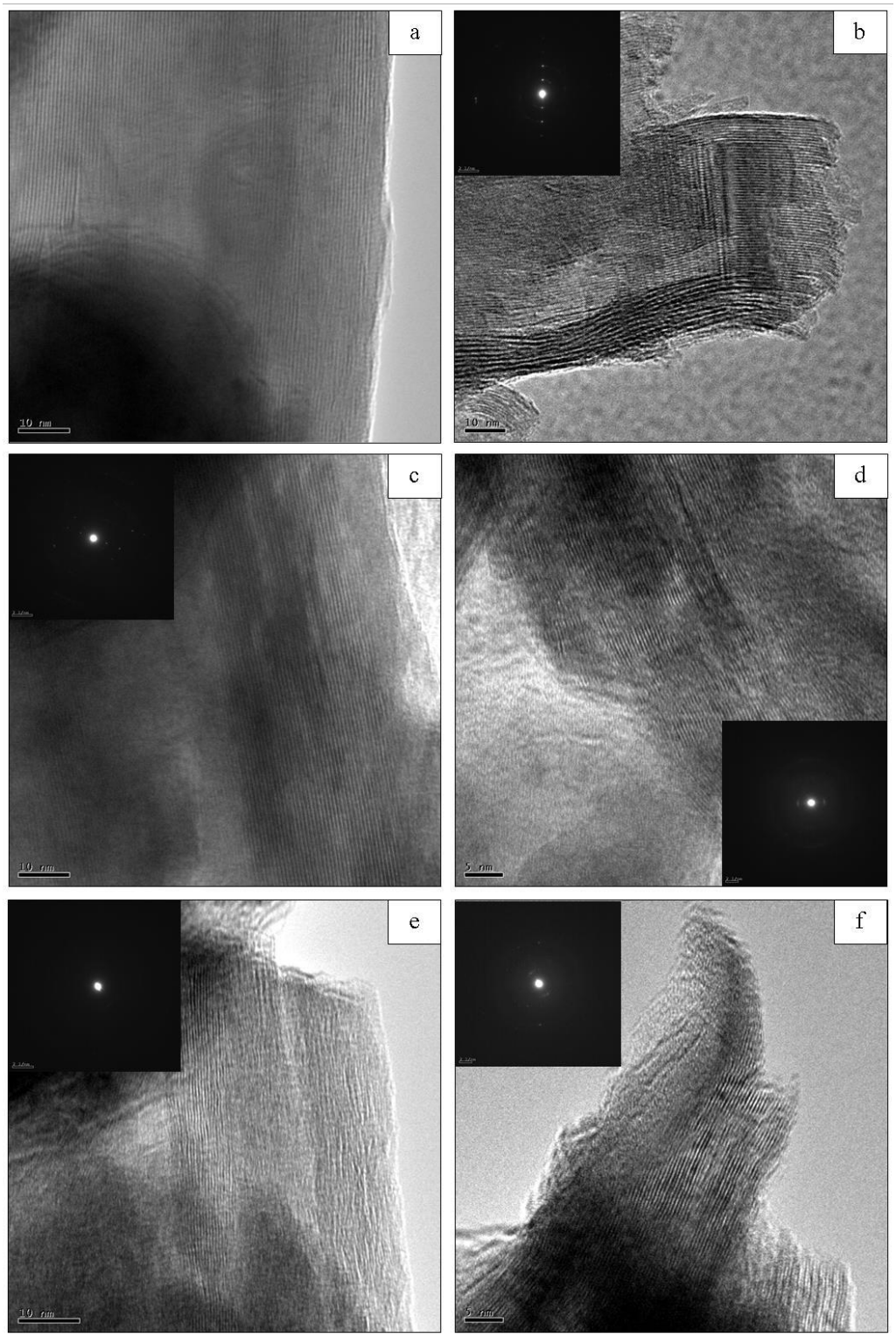

Figure 3.23 TEM brightfield images of lizardite and a phase with 5 Å basal spacing found in sample 4. Image contrast has been altered to improve relief. **(a)** Lattice fringe image of lizardite showing lenticular lattice separations. **(b-d)** Lattice fringe images of lizardite; inset: SAED patterns of the regions. **(e-f)** Regions of wavy, continuous lattices with a 5 Å d-spacing.

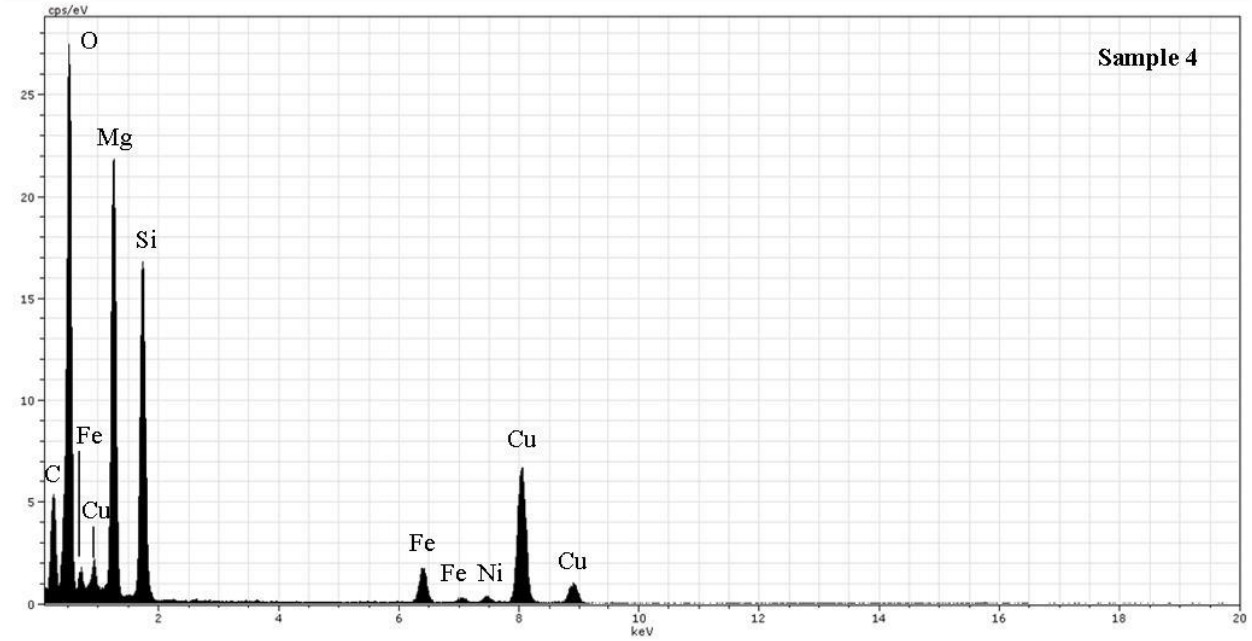

Figure 3.24 EDS spectra of a lizardite-bearing region in sample 4. The EDS spot analysis shown corresponds with Figure 3.23b.

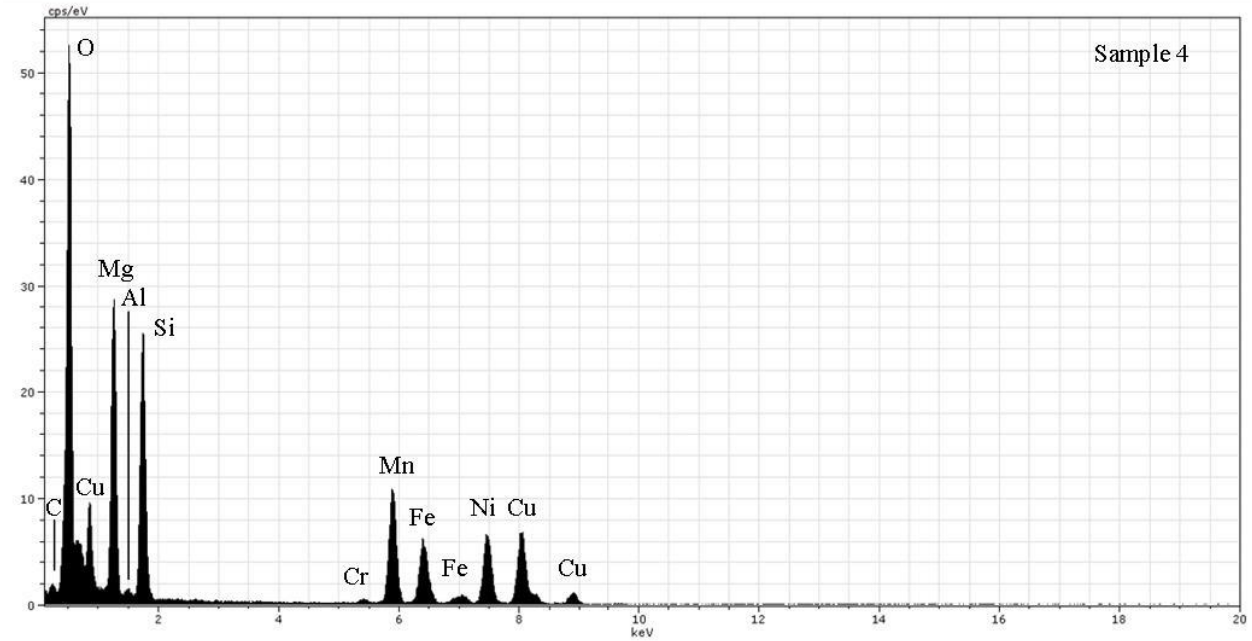

Figure 3.25 EDS spectra of a region of 5 Å lattices in sample 4. The EDS spot analysis shown corresponds with Figure 3.23e.

explanation of a more complex interstratification scheme where brucite-like layers or other oxyhydroxide layers exist may be the case. The composition of these regions show them to

contain O, Si, Mg, Ni, Fe, and Mn, with minor Al and Cr. Normalized EDS spot analyses of a region bearing the 5 Å phase has 52% O, 20% Si, 22% Mg, 5% Ni, 5% Fe, 11% Mn, 0.5% Cr, and 0.5% Al (Fig. 3.25).

3.2.5 Sample 5

Sample 5 is composed of a talc-like phase with minor lizardite, chrysotile, and chlorite. The talc-like phase dominates the sample, representing 95% of the sample whereas the lizardite, chrysotile, and chlorite comprise the other 5% in equal quantities.

The talc-like phase occurs as pseudo-lamellar platy aggregates with associated local chlorite (Fig. 3.26a). Lattice fringe images of the talc-like phase have 10 Å basal spacing and textures consistent with turbostratic stacking, such as pinch-out structures, which occurred in all of the regions examined over 5-10 nm with 1-2 lattices displaced (Fig. 3.26b-c). Lattice curvature is also present in all of the regions examined and was not continuous throughout entire particles, rather only being observed at particle terminations. Toward these terminations, multiple lattices converge due to pinch-outs to a 'peak' of 1 to 2 lattices (Fig. 3.26b). One local region bearing continuous lattices with 14 Å d-spacing interpreted as chlorite was observed in a talc-bearing region (Fig. 3.26d), the phases were not observed to be interstratified. High resolution imaging of the talc-like and chlorite phases was difficult owning to beam damage and particle thickness. The talc and chlorite-bearing regions are comprised of O, Si, Mg, and Ni with minor Fe. Normalized EDS spot analysis of a region bearing these phases shows 29% O, 46% Si, 18% Mg, 6% Ni, and 1% Fe.

Lizardite occurred only in one of the regions analyzed as a particle 170 nm long and 100 nm wide with severe beam-sensitivity. A lattice fringe image obtained from this particle show a

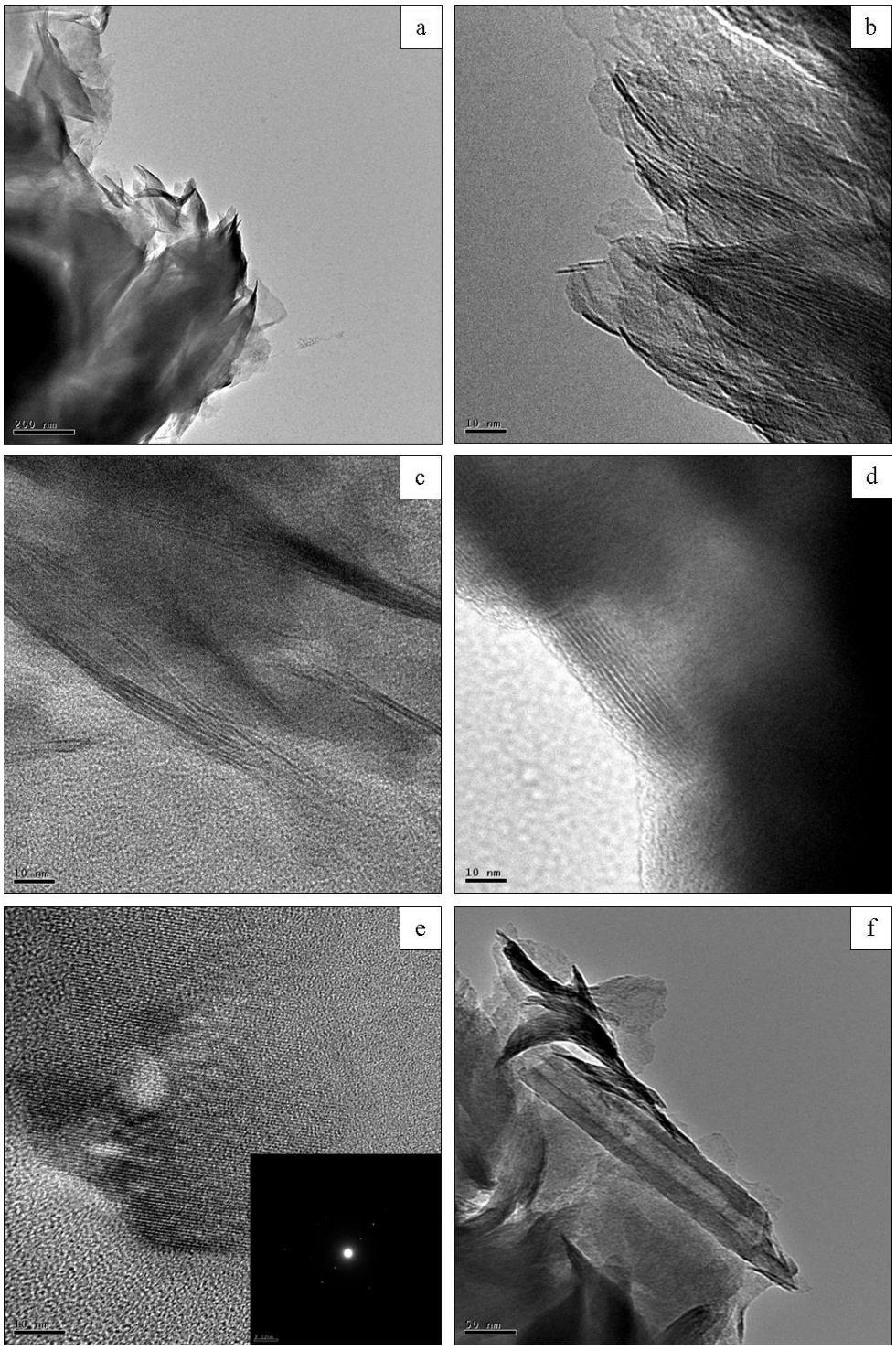

Figure 3.26 TEM brightfield images of the phyllosilicates found in sample 5. Image contrast has been altered to improve relief. **(a)** General texture of the talc and chlorite-bearing regions. **(b-c)** Lattice fringe images of the turbostratified talc-like phase. **(d)** Lattice fringe image of a chlorite-bearing region. **(e)** Lattice fringe image of a lizardite-bearing region; inset SAED pattern. **(f)** Chrysotile nanofiber adjacent to a talc and chlorite-bearing region.

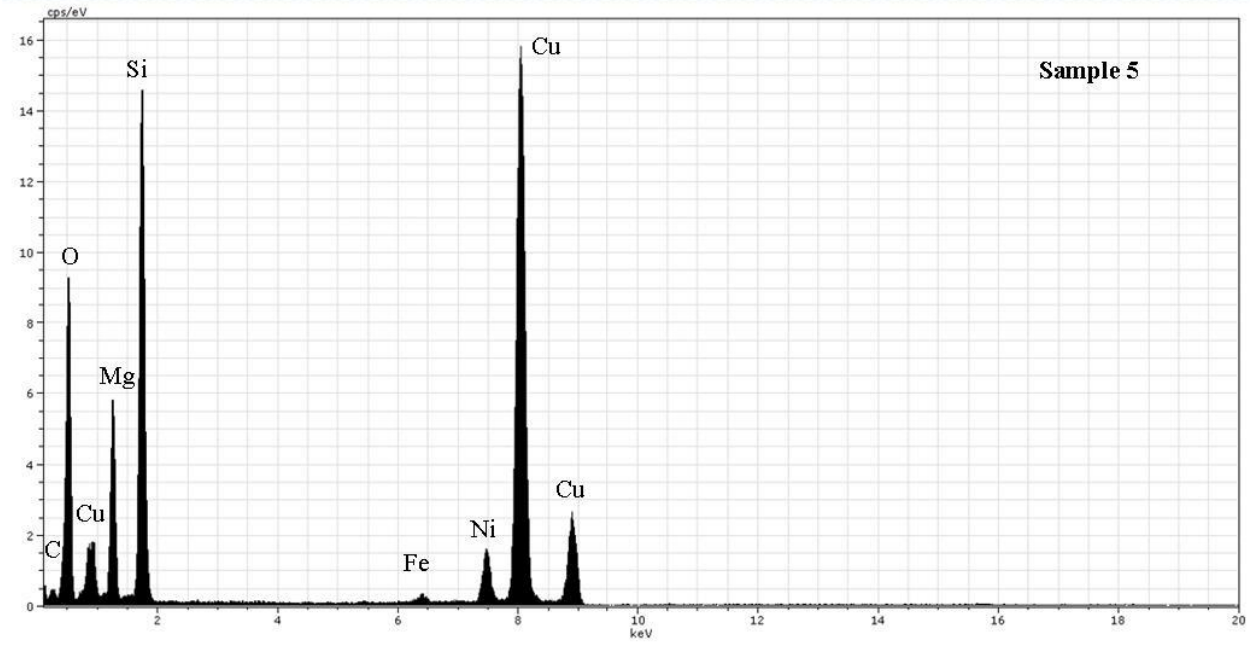

Figure 3.27 EDS spectra of a talc-bearing region in sample 5. The spot analysis shown corresponds with Figure 3.26b.

6 Å d-spacing and the SAED pattern collected shows $d_{(002)}$ = 5.9 Å, $d_{(004)}$ = 3.0 Å, and $d_{(006)}$ = 2.0 Å (Fig. 3.26e). These values are consistent with those of lizardite, however, each is slightly lower from ideal lizardite, which has $d_{(002)}$ = 7.3 Å, $d_{(004)}$ = 3.6 Å, and $d_{(006)}$ = 2.4 Å (Mellini and Zanazzi, 1987). This phase could also represent a degraded or altered chlorite; however, high resolution imaging was not possible due to beam damage.

A single chrysotile nanofiber was observed; it measured 320 nm long, 55 nm wide, and had a wall-thickness of 17 nm. It was found adjacent to a particle of aggregated talc-like and chlorite (Fig. 3.26f).

3.2.6 Sample 6

Sample 6 is composed of lizardite and chrysotile, which comprise approximately 60 and 35% of the regions analyzed, respectively. Approximately 5% of the regions examined also contain particles that resemble polygonal serpentine.

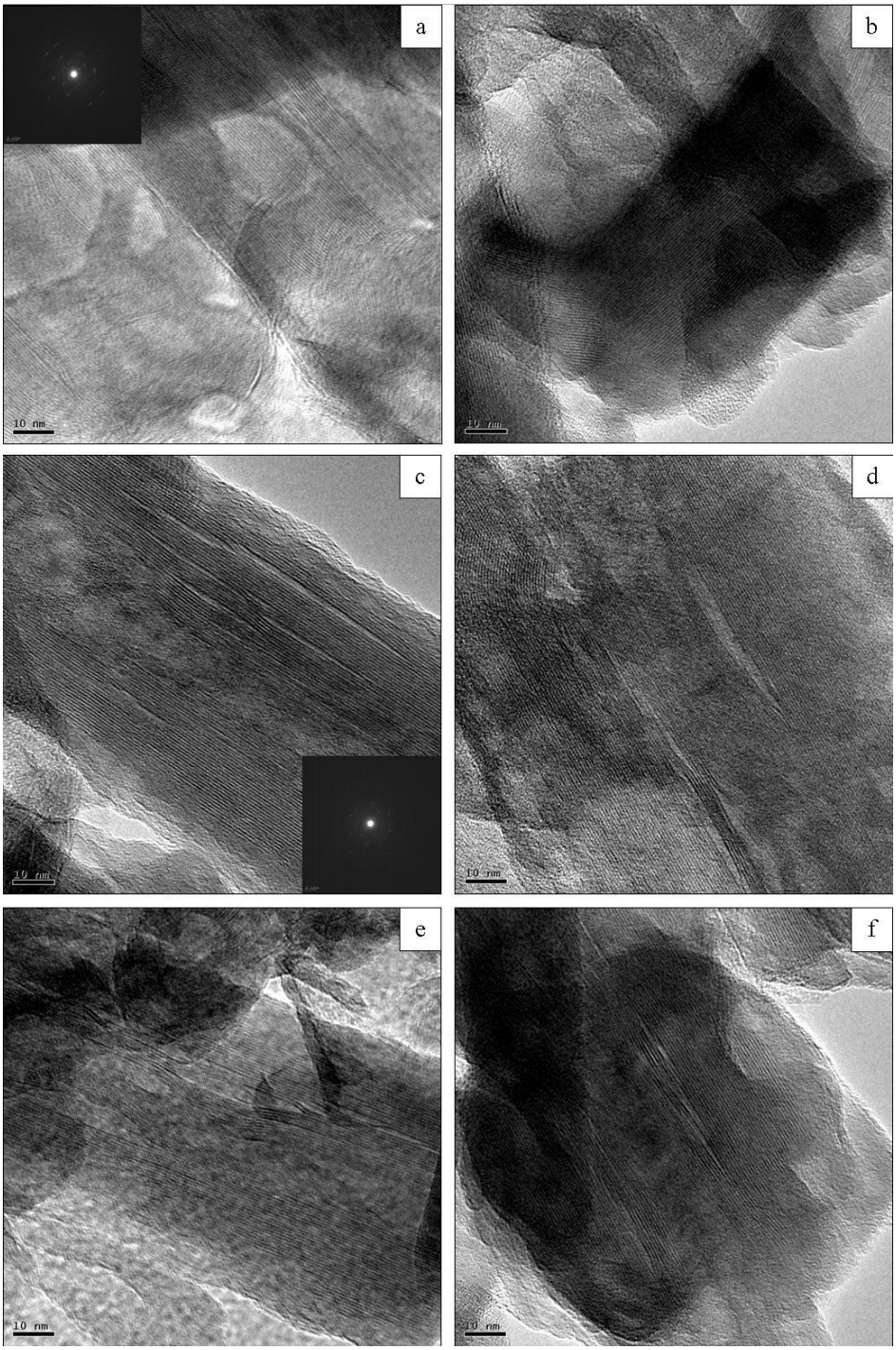

Figure 3.28 TEM brightfield images of lizardite in sample 6. Image contrast has been altered to improve relief. **(a)** Lattice fringe image of lizardite with linear lattices and with curved, wrapping lattices near particle termination. **(b)** Lattice fringe image of lizardite. **(c)** Lattice fringe image of lizardite showing lenticular defect structures; inset: SAED pattern of the region. **(d)** Lattice fringe image of lizardite showing lenticular defect structures in linear lattices. Curved, wrapping lattices are also observed near particle termination. **(e-f)** Lattice fringe images of lizardite showing lenticular defect structures.

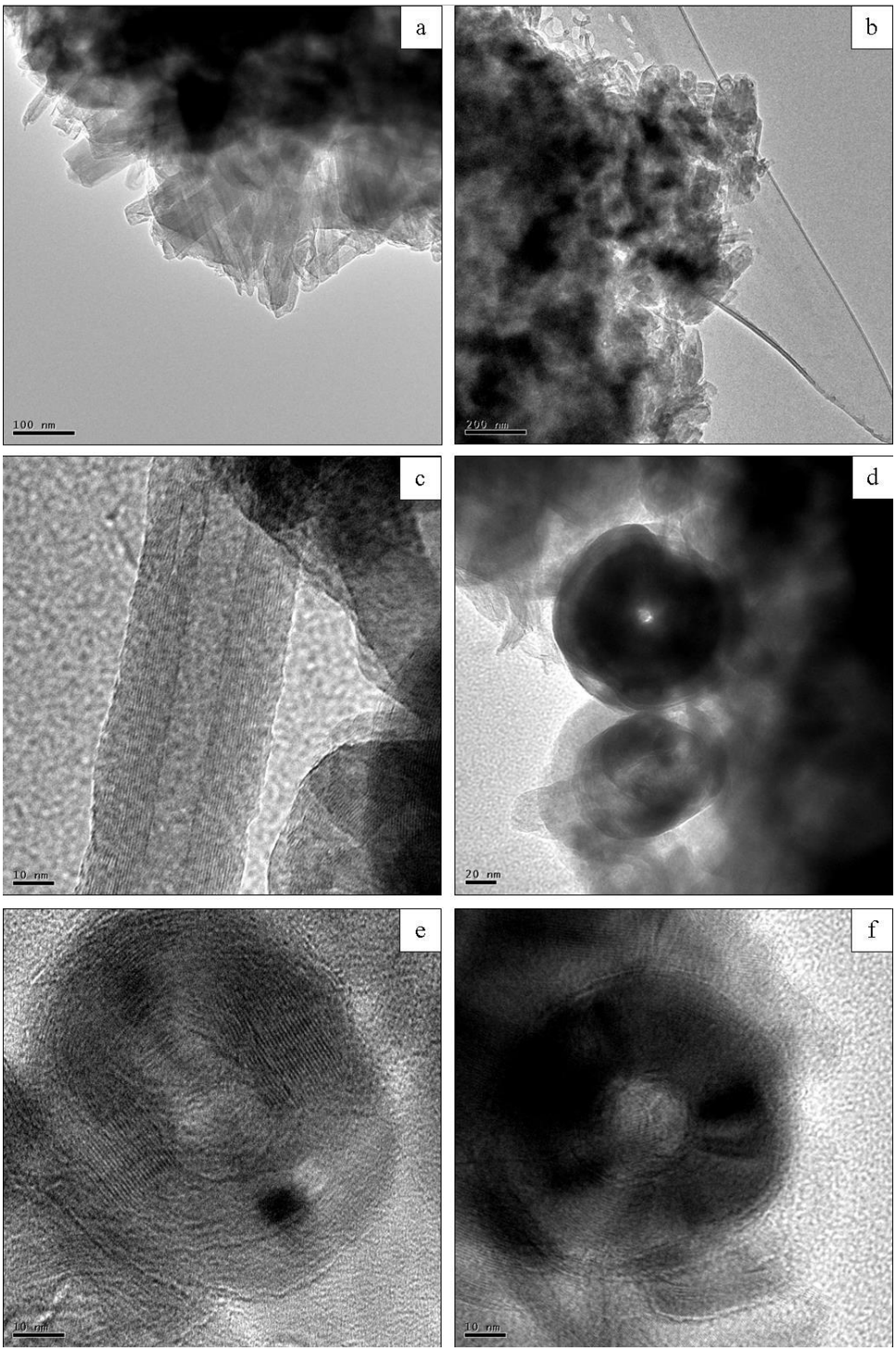

Figure 3.29 TEM brightfield images of chrysotile and pseudo-polygonal serpentine in sample 6. Image contrast has been altered to improve relief. **(a-b)** General texture of the chrysotile-bearing regions. **(c)** Lattice fringe image of a chrysotile nanofibers. **(d)** Image showing chrysotile observed down the fiber axis. **(e)** Lattice fringe image of chrysotile observed down the fiber axis. **(f)** Image showing evidence of sector zoning associated with polygonal serpentine.

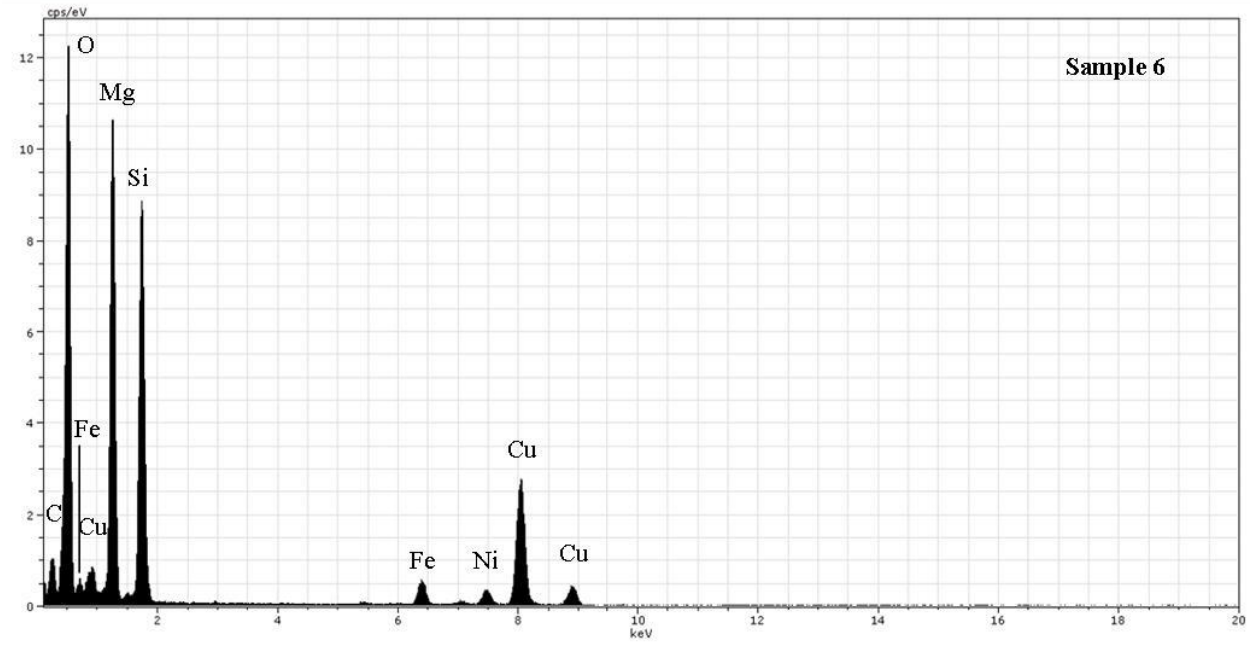

Figure 3.30 EDS spectra of a lizardite-bearing region in sample 6. The spot analysis shown corresponds with Figure 3.28a.

The lizardite occurs in aggregates of broad platy crystals with 7 to 7.3 Å basal spacing (Fig 3.28a-b) intermixed with chrysotile. Although lattices are continuous in all of the lizardite crystals examined, lenticular lattice separations are very common, occurring in approximately 80% of the regions examined. These defects show two adjacent lattices diverging away from each other at 5 to 25° angles and reconvening 5 to 40 nm later, leaving slit-shaped voids in the lattice that vary 1 to 5 nm in width (Fig. 3.28c-f). In approximately 75% of the regions examined, linear lizardite lattices appear to curve and wrap around the edge of the particle rather than terminate at the edge (Fig. 3.28a and d).

Chrysotile occurs with lizardite in aggregates of disarticulated tubular crystals (Fig. 3.29a-b). The tubes vary 50 to 240 nm in length, 20 to 50 nm in width, 8 to 12 nm in wall thickness, and 10 to 12 nm in pore width. Chrysotile d-spacing varies 7 to 7.7 Å and this larger d-spacing is interpreted to be a result of beam damage (Fig. 3.29c). Circular particles (Fig. 3.29d-

f) are interpreted to be chrysotile observed down the fiber axis; however, these features may represent polygonal serpentine. Sectored zoning associated with polygonal serpentine is absent in most circular sections; however approximately 20% have some evidence of it (Fig. 3.29f). High resolution images of these features were not possible owning to beam damage.

All of the phases examined are quite chemically homogenous, being composed of O, Si, Mg, Fe, and Ni in nearly identical proportions region to region. Normalized spot EDS analysis of a lizardite-bearing region shows 37% O, 27% Si, 32% Mg, 2% Fe, and 2% Ni (Fig 3.30).

3.2.7 Sample 7

Sample 7 is composed of chrysotile, lizardite, and minor chlorite, which comprise approximately 60%, 30%, and 10 % of the regions examined, respectively.

Chrysotile occurs both as disarticulated aggregates and as lineated packages of tubular particles (Fig. 3.31a-b). The nanofibers vary 80 to 600 nm in length, 25 to 100 nm in width, 8 to 25 nm in wall thickness, and 8 to 16 nm in pore size. The d-spacing of the lattice fringes varies 7 to 7.3 Å and the lattices are continuous in approximately 95% of regions examined (Fig. 3.31c-d). Lattice defects were observed in approximately 5% of the chrysotile; Figure 3.31e shows a defect within a nanofiber in which a portion of the lattice 5 nm in width diverges at a 35° angle from the rest of the lattice, displacing 5-10 lattices. Following this, the package of displaced lattices appears to twist 360° and reconnect with the rest of the lattice, creating a semi-circle shaped gap 60 nm long and 8 nm wide. Circular particles are interpreted to be chrysotile observed down the fiber axis (Fig. 3.31f). Chrysotile is composed of O, Si, Mg, Fe, and Ni. Normalized EDS spot analysis of a chrysotile-bearing region show 23% O, 34% Si, 31% Mg, 11% Fe, and 1% Ni (Fig. 3.32).

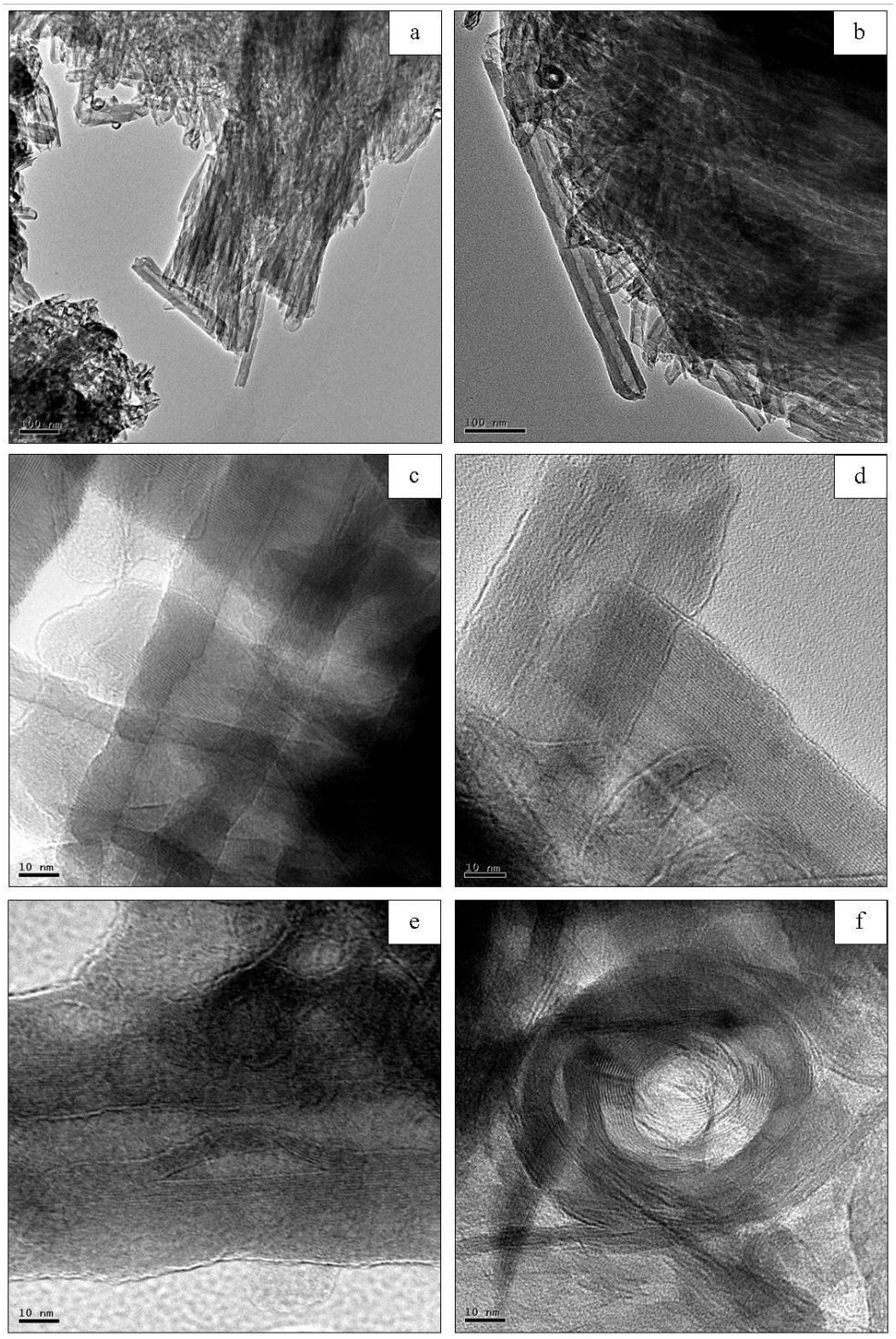

Figure 3.31 TEM brightfield images of chrysotile in sample 7. Image contrast has been altered to improve relief. **(a-b)** General texture of the aggregated chrysotile nanofibers; lizardite is also present within these aggregates. **(c-d)** Lattice fringe images of chrysotile nanofibers. **(e)** Lattice defect in chrysotile lattice. **(f)** Lattice fringe image of chrysotile crystal observed down the fiber axis.

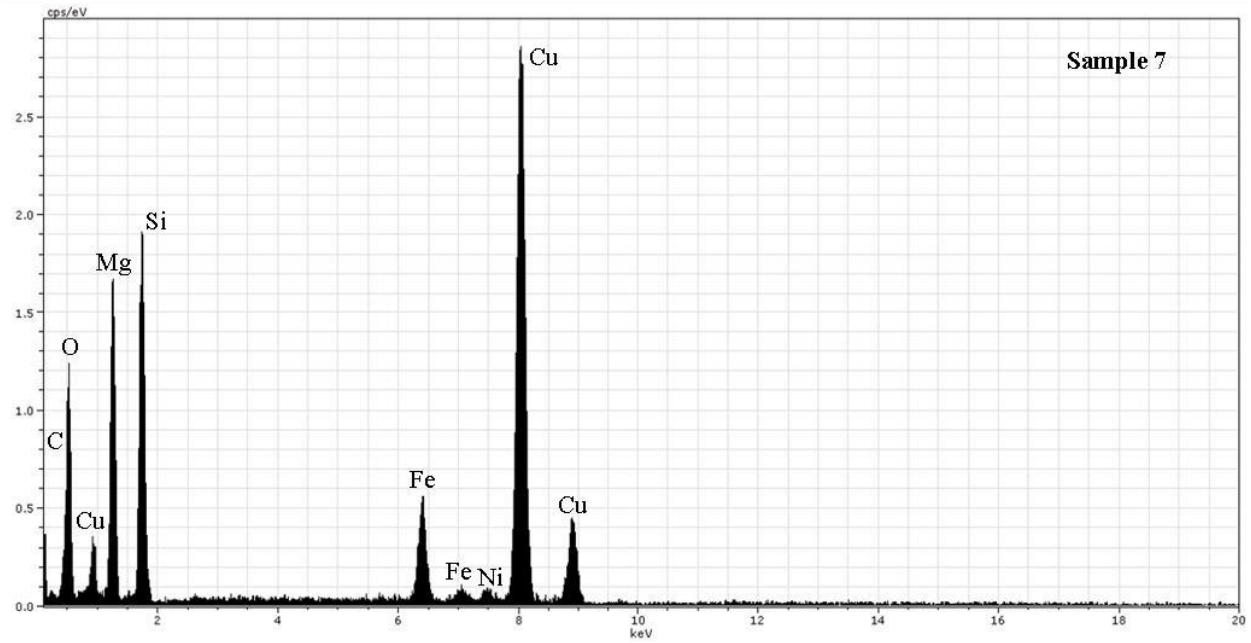

Figure 3.32 EDS spectra of a chrysotile-bearing region in sample 7. The spot analysis shown corresponds with Figure 3.31d.

Intermixed with the chrysotile, lizardite occurs as broad platy crystals with 7 to 7.5 Å basal spacing (Fig 3.33a-b). Although the lattices are continuous in all of the lizardite crystals examined, lenticular lattice separation defects are very common, occurring in approximately 80% of the regions examined. These defects consist of two adjacent lattices diverging away from each other at 10 to 20° angles and reconvening 10 to 20 nm later, leaving slit-shaped voids in the lattice that vary 2 to 8 nm in width (Fig. 3.33c-f). Lizardite is composed of O, Si, Mg, Fe, and trace Ni. Normalized EDS spot analysis of a lizardite-bearing region show 34% O, 29% Si, 35% Mg, 2% Fe, and <1% Ni (Fig. 3.34).

Chlorite occurs as pseudo-lamellar platy aggregates with 14 Å d-spacing directly adjacent to the aggregates of lizardite and chrysotile (Fig. 3.35a) The chlorite particles show significant turbostratification in the form of lattice pinch-outs, which occur in 100% of the regions analyzed, displacing 1-3 lattices over 5 to 10 nm (Fig. 3.35b-d); this displacement occurs in such a way

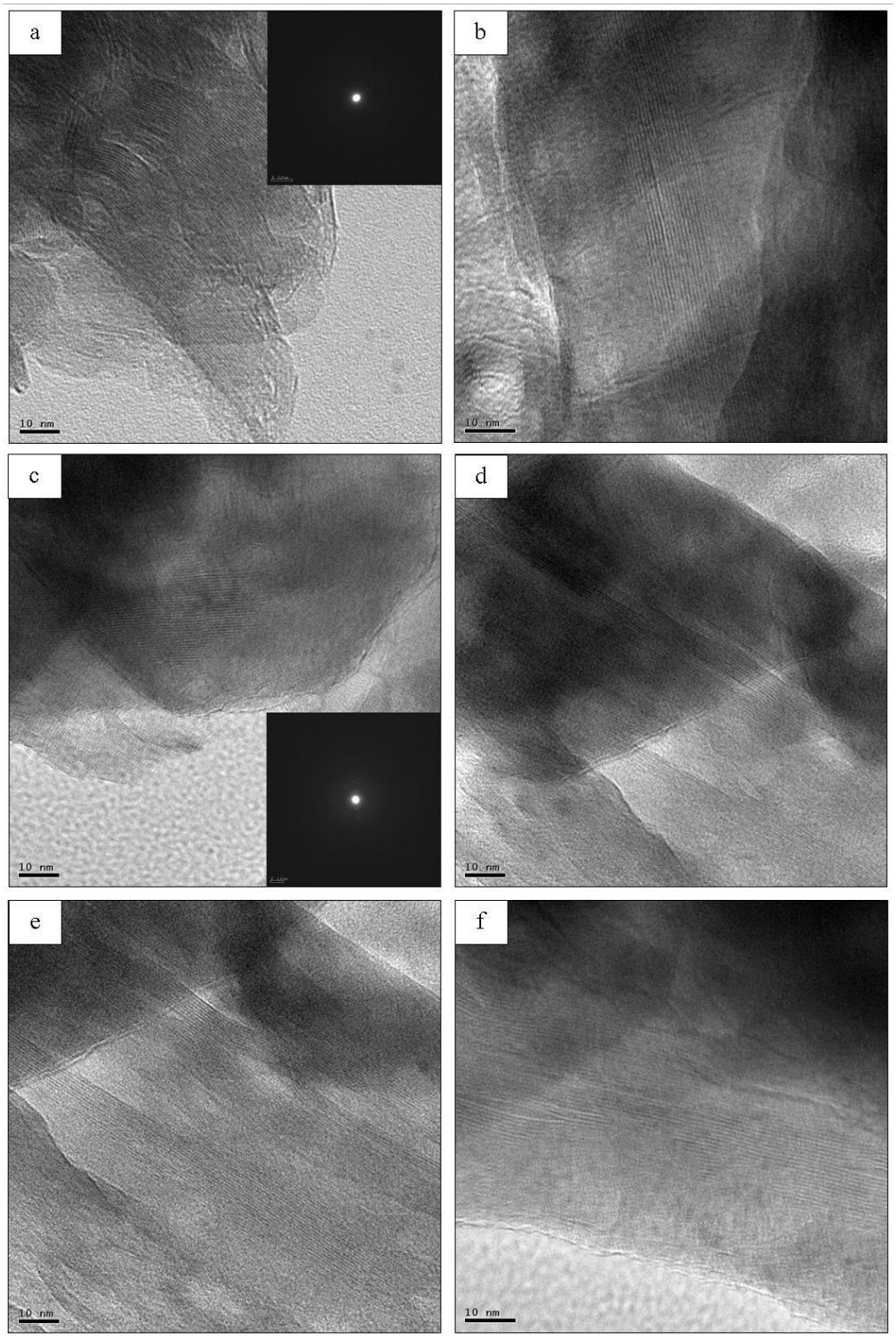

Figure 3.33 TEM brightfield images of lizardite-bearing regions in sample 7. Image contrast has been altered to improve relief. **(a-c)** Lattice fringe images of lizardite crystals; inset: SAED patterns of regions. **(d-f)** Lattice fringe images of lizardite crystals showing lenticular lattice separation defects.

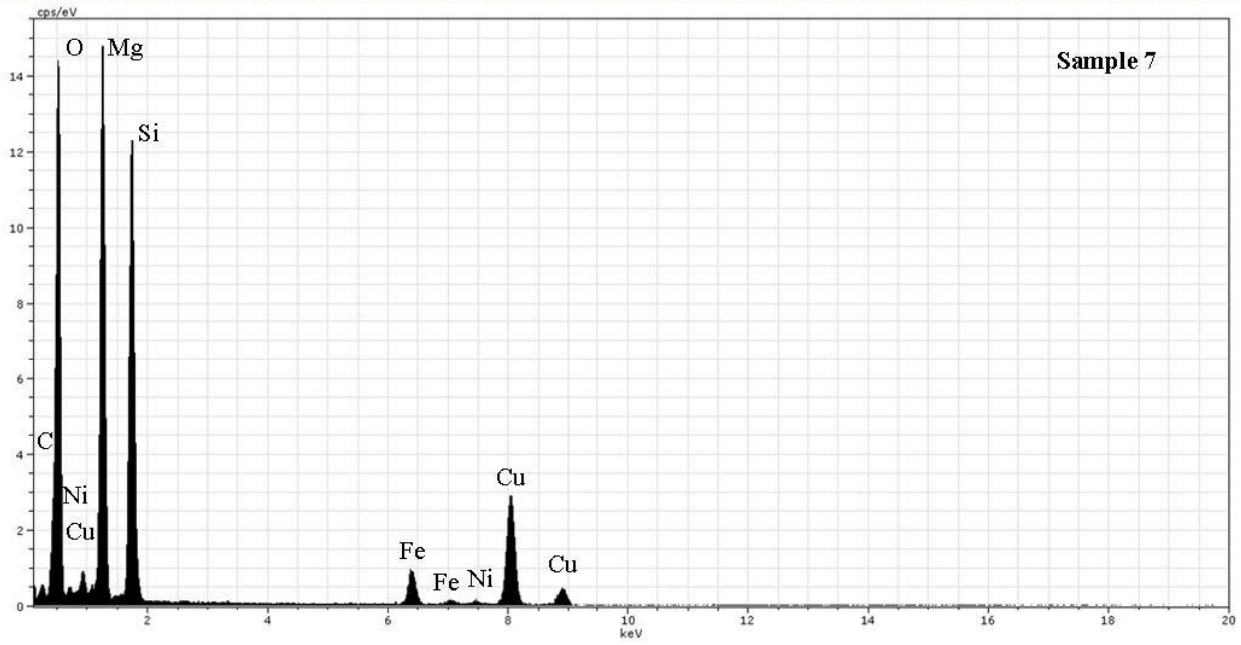

Figure 3.34 EDS spectra of a lizardite-bearing region in sample 7. The spot analysis shown corresponds to Figure 3.33b.

that particles terminate in a 'peak' of 1 to 2 lattices (Fig. 3.35c-d). The lattices also display significant curvature. The chlorite is composed of O, Si, Mg, Fe, and trace Ni, Cl, and K. Normalized EDS spot analysis of a chlorite-bearing region show 38% O, 28% Si, 29% Mg, 3% Fe, with Ni, Cl, and K comprising the final 2% in equal measure (Fig. 3.36).

3.2.8 Sample 8

Sample 8 is composed of chrysotile and antigorite, which comprise approximately 60% and 40% of the regions examined, respectfully.

Chrysotile occurs as isolated nanofibers and as aggregates of disarticulated nanofibers that vary 150 to 700 nm in length, 35 to 165 nm in width, and 10 to 20 nm in wall thickness (Fig. 3.37a). The d-spacing of the lattice fringes in chrysotile is 7 to 7.2 Å (Fig. 3.37b). The nanofibers also occur directly adjacent to platy crystals of antigorite (Fig. 3.37c).

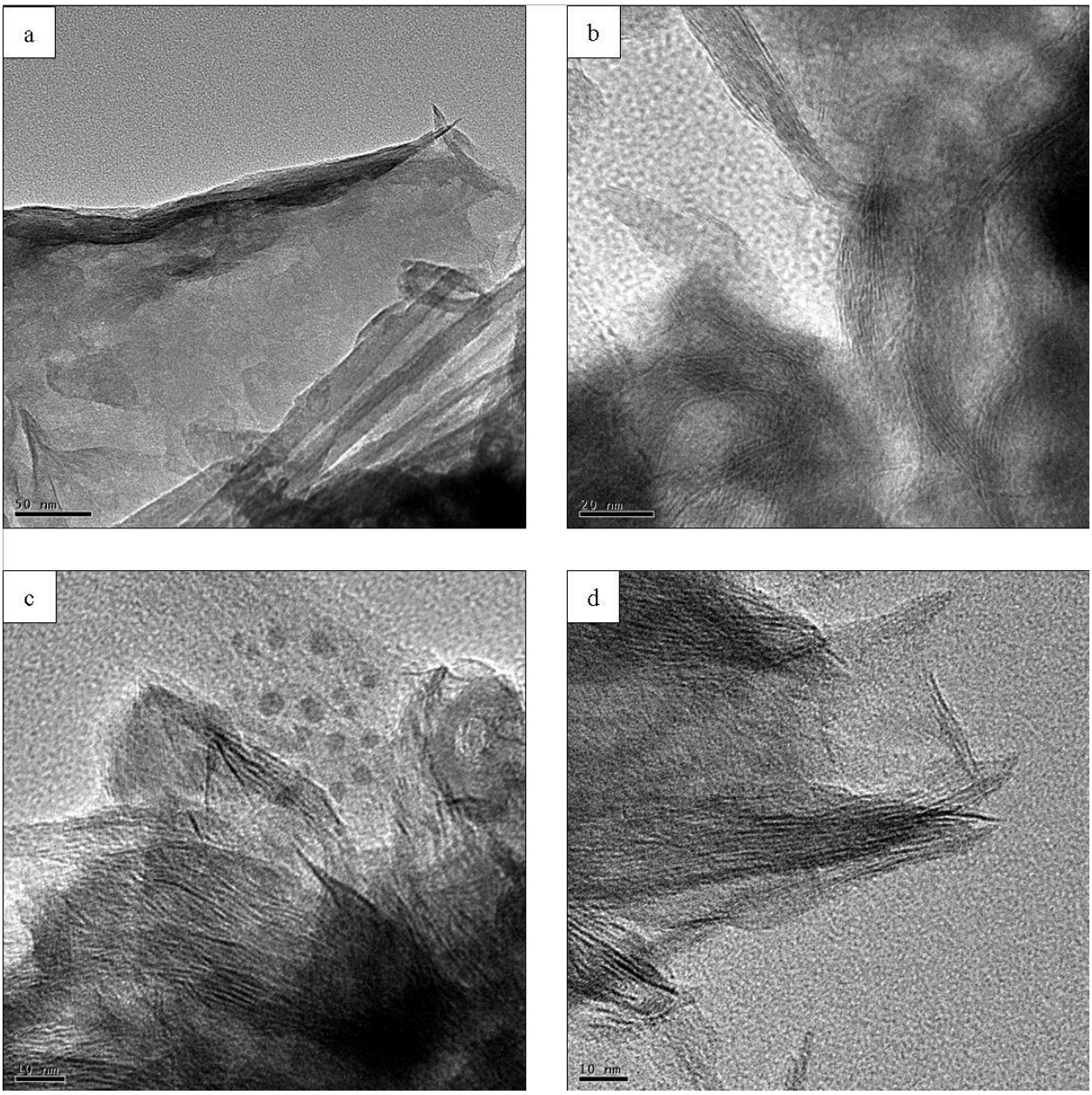

Figure 3.35 TEM brightfield images of chlorite-bearing regions in sample 7. Image contrast has been altered to improve relief. **(a)** General texture of a chlorite-particle, adjacent to a chrysotile nanofiber. **(b-d)** Lattice fringe images of chlorite showing significant crystallographic disorder.

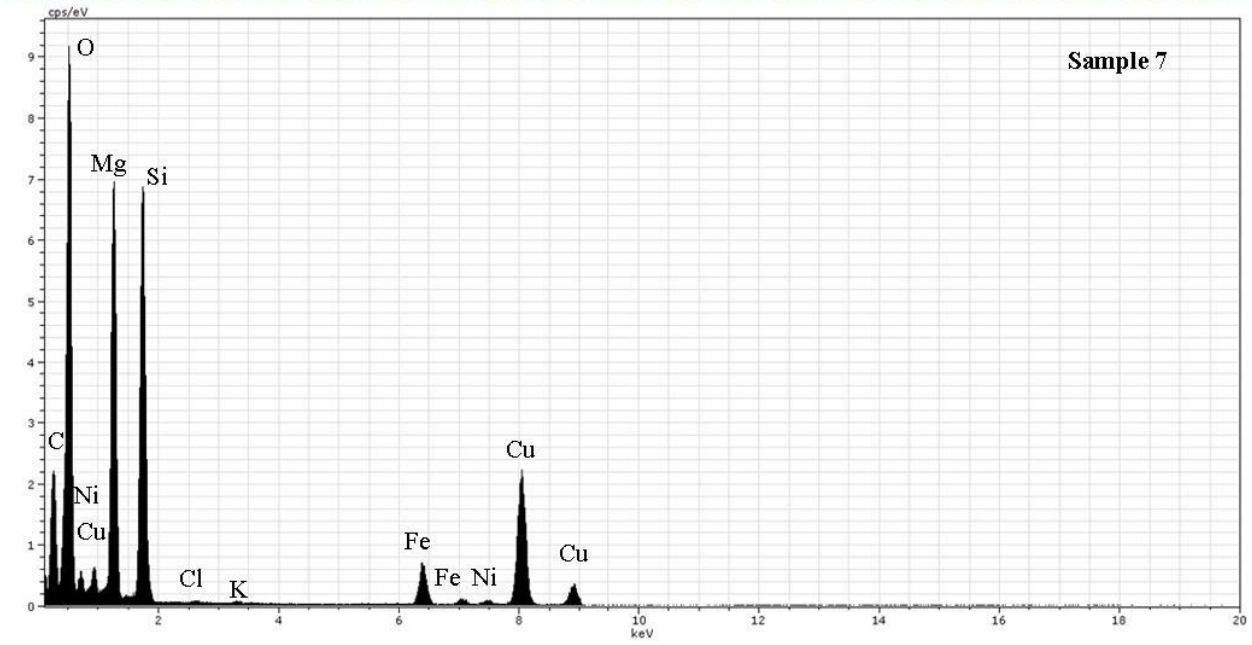

Figure 3.36 EDS spectra of a chlorite-bearing region in sample 7. The spot analysis shown corresponds with Figure 3.35c.

Antigorite occurs as platy crystals 700 to 2,500 nm long and 285 to 625 nm wide. The surface of the crystals displays a corrugated texture consistent with antigorite morphology and agrees well with published images (e.g. Da Costa et al. 2008; Wunder et al. 2001). The modulations are continuous and vary 25 to 50 Å in width (Fig. 3.37d-f). SAED images of the lattices agree well with those published by Da Costa et al. (2008) and Dódony et al. (2002) for antigorite.

All of the regions examined in this sample varied very little in chemistry. A region bearing both chrysotile and lizardite was comprised of O, Si, Mg, Fe, and Ni. Normalized EDS spot analysis for this region has 19% O, 39% Si, 37% Mg, 3% Fe, and 2% Ni.

3.2.9 Sample 9

Sample 9 is composed of silver nanoparticles, amorphous silica, antigorite, chrysotile, and an Al-rich phase consistent with kaolinite. The silver nanoparticles comprise approximately

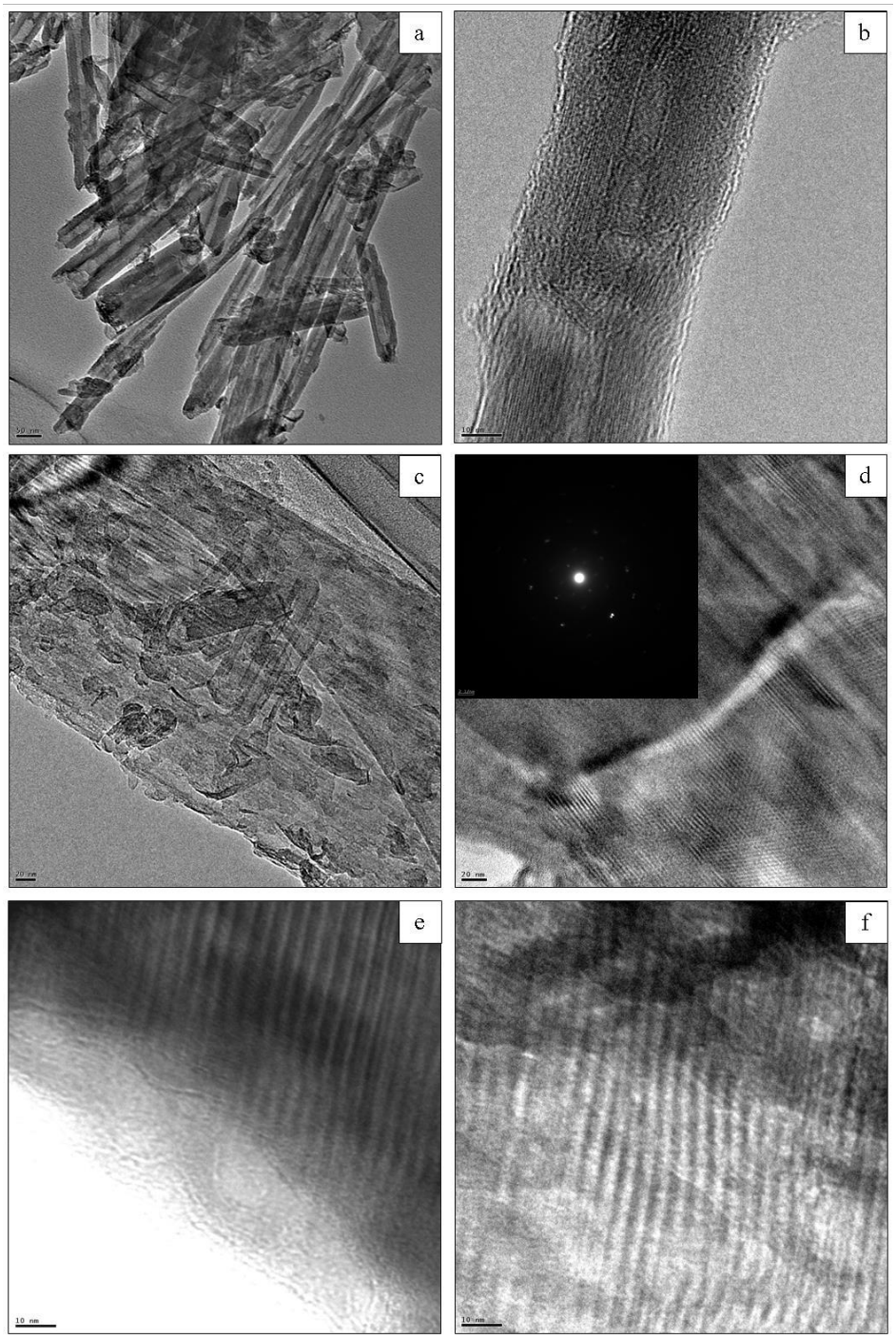

Figure 3.37 TEM brightfield images of chrysotile and antigorite in sample 8. Image contrast has been altered to improve relief. **(a)** General texture of the disarticulated chrysotile nanofibers. **(b)** Lattice fringe image of a broken chrysotile nanofiber. **(c)** Image showing an antigorite crystal overlying disarticulated chrysotile nanofibers. **(d)** Lattice fringe image of several overlapping antigorite particles; inset: SAED pattern of the region. **(e-f)** Images observing the corrugated surface of antigorite crystals (viewing perpendicular to the a-b plane).

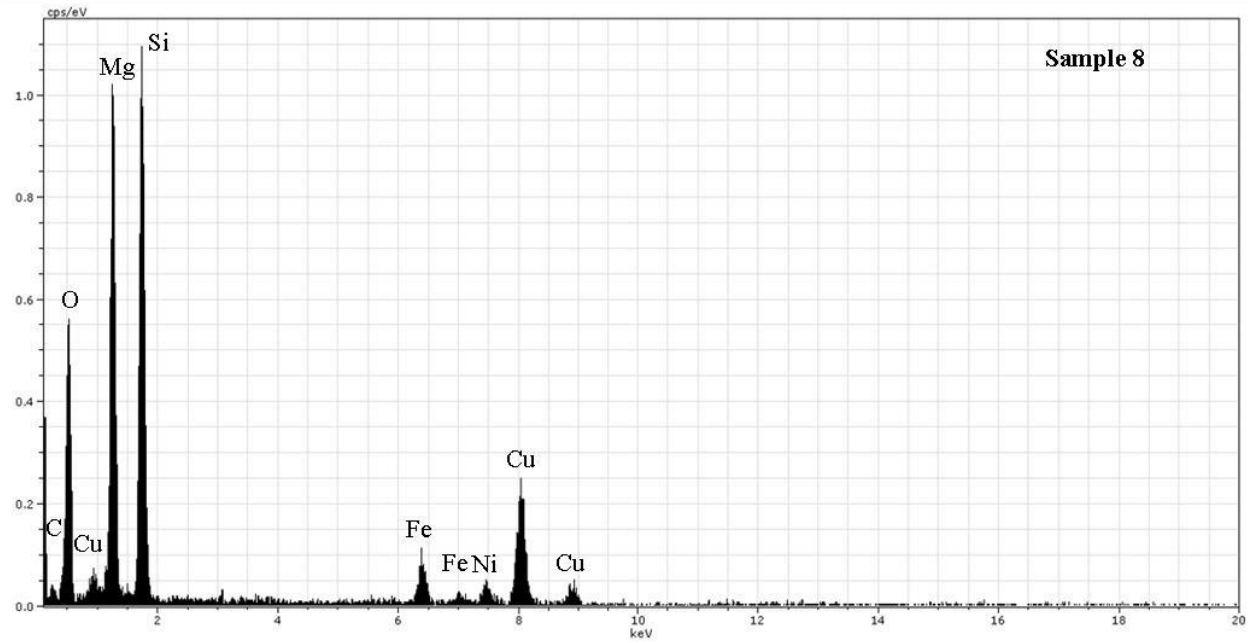

Figure 3.38 EDS spectra of a region bearing both chrysotile and antigorite. The spot analysis shown corresponds to Figure 3.37c.

50% of the regions analyzed, with amorphous silica comprising approximately 20%, antigorite comprising approximately 20%, chrysotile comprising approximately 5%, and kaolinite comprising approximately 5%.

All of the silver nanoparticles are near spherical to irregular-oblate in shape and possess a range of complex textures and associations with the other phases. There is a bimodal size distribution among the nanoparticles; particles that vary 2 to 30 nm in diameter comprise approximately 75% of the total textures and particles that vary 150 to 650 nm in diameter comprise approximately 25% of the textures examined. Approximately 40% of the regions analyzed have the 2-30 nm particles alone whereas 60% of the regions had both 2 to 30 nm and 150 to 650 nm particles present.

The nanoparticles are dispersed within a matrix of amorphous silica and possess internal linear features that are interpreted as twin planes, likely on [111]. The d-spacings of $d_{(111)}$ = 2.39

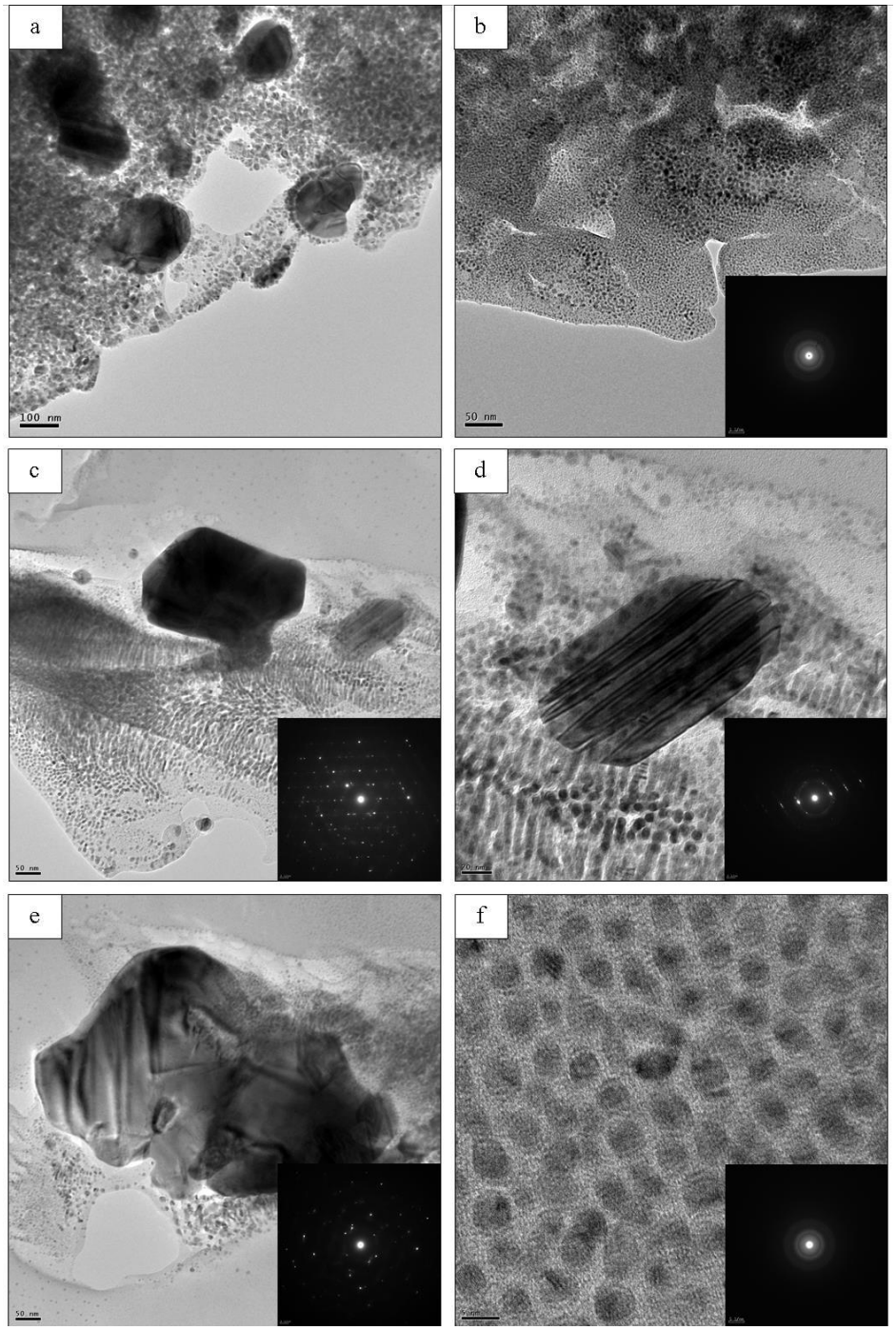

Figure 3.39 TEM brightfield images of silver nanoparticles in sample 9. **(a)** Image showing bimodal size distribution and nanoporphyroblast texture of Ag-nanoparticles. **(b)** Image showing individual and aggregating nanoparticles spatially distributed according to size; inset SAED pattern. **(c-d)** Nanoporphyroblasts within a matrix of smaller, aggregating nanoparticles with a preferred orientation; inset SAED patterns. **(e)** Nanoporphyroblast surrounded by and potentially assimilating smaller nanoparticles; inset SAED pattern. **(f)** Detailed image of small size range nanoparticles; inset SAED pattern.

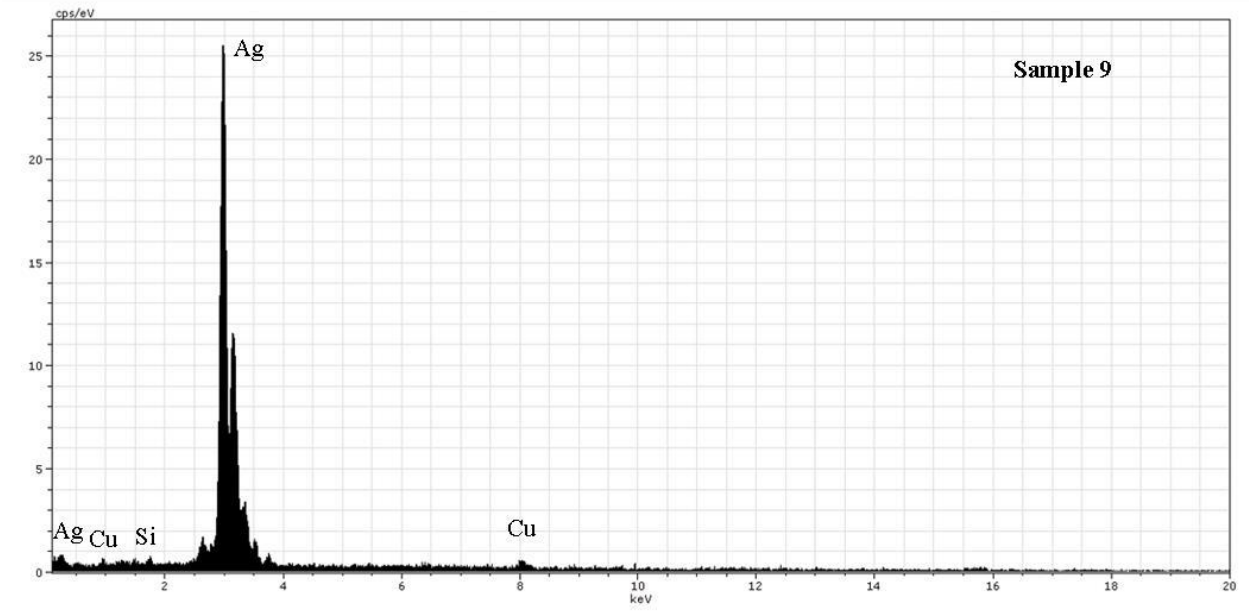

Figure 3.40 EDS spectra of a silver nanoparticle in sample 9. The spot analysis shown corresponds with Figure 3.39d.

Å, $d_{(200)}$ = 1.98 Å, $d_{(220)}$ = 1.44 Å from SAED patterns of the nanoparticles are consistent with those published for silver (Wyckoff, 1963; Novgorodova et al. 1981).

The nature of the contact between adjacent silver nanoparticles is variable. Approximately 20% of the nanoparticles exist as discrete spherules that do not come into contact with adjacent spherules (Fig. 3.39b,f) and approximately 80% of the regions examined show nanoparticles aggregating together (Fig. 3.39a-f). There is a distinct trend of spatial size gradation; particles approximately 30 nm in diameter are surrounded by or aggregating with other particles of similar size with particle size decreasing away from that particle (Fig. 3.39a-b). Regions containing both size modes, a texture that appears nano-porphyroblastic in nature, nanoparticles that are in the 150 to 650 range (the nanoporphyoblasts) displace or appear to be assimilating nanoparticles in the 2 to 30 nm range (Fig. 3.39a, c, d, and e). Figure 3.39c-d shows two nanoporphyroblasts that are associated with the smaller range of nanoparticles that appear to be aggregated with a preferred lineation, potentially influenced by the nanoporphyroblast itself;

lineation of nanoparticles was observed in 20% of the regions examined. Overall, the textures of the silver nanoparticles in this sample are consistent with Ostwald ripening phenomena.

In regions where the silver nanoparticles interface with the other mineral phases, only the smaller size distribution is present, not the nanoporphyroblasts. Although the nanoparticles are dispersed within a matrix of amorphous silica, they are not found associated with regions of isolated amorphous silica networks. The nanoparticles are found associated with the Al-rich kaolinite-like mineral, having an irregular, undulatory interface with this phase (Fig. 3.43b); this occurred in 100% of the regions bearing the kaolinite-like phase. The nanoparticles are also found associated with antigorite and chrysotile-bearing regions, intruding into platy crystals of antigorite, producing a reaction halo where the antigorite structure is destroyed at the interface of nanoparticle intrusion. Observed in one such region is a chrysotile nanofiber entrained by the intruding mass of Ag-nanoparticles (Fig 3.45f); these interfaces with the Ag-nanoparticles occurred in 25% of the antigorite and chrysotile-bearing regions. The silver nanoparticles are composed of Ag with minor Si. Normalized EDS spot analysis of one of the nanoporphyroblasts has 97% Ag and 3% Si (Fig. 3.40).

Amorphous silica occurs as porous, anastomosing networks of near-spherical to irregular oblate particles (Fig. 3.41 a-b). The particles vary 10 to 56 nm in diameter with an average diameter of 20 to 30 nm. SAED patterns of lower magnificent images of the networks show an absence of diffracting planes (Fig. 3.41c); however, high magnificent images show a random granular texture suggesting short-range order corroborated by the diffuse diffraction rings from the FFT (Fig. 3.41d). The pores are irregular in shape, varying 20 to 280 nm long and 20 to 100

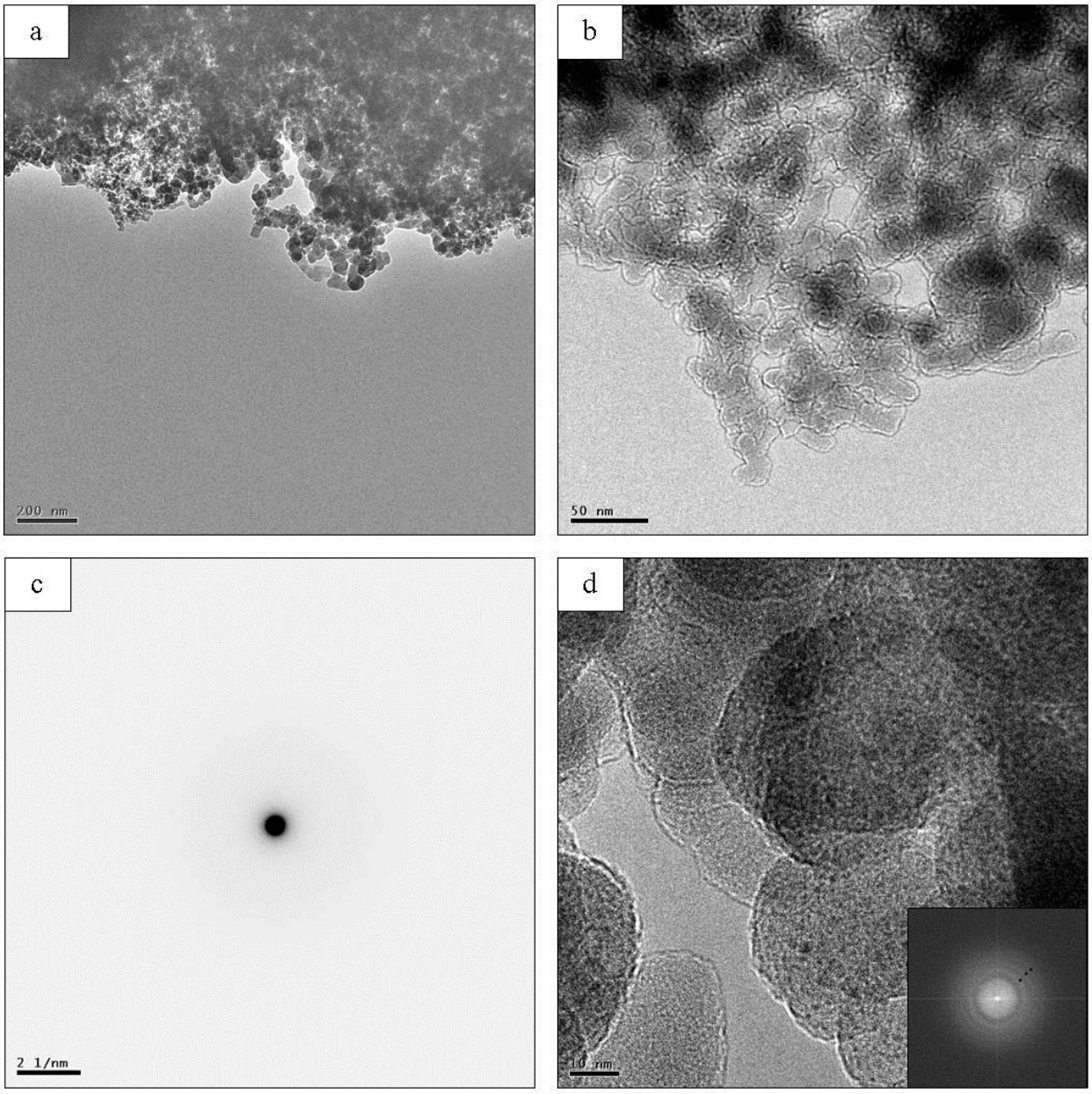

Figure 3.41 TEM brightfield images of amorphous silica in sample 9. Image contrast has been altered to improve relief. **(a-b)** Porous, anastomosing networks of amorphous silica. **(c)** SAED pattern of low-magnification image of amorphous silica. **(d)** High magnification image of amorphous silica spherules showing random granular texture; inset FFT showing diffuse diffraction rings.

nm wide. The pores are present in approximately 10% of the aggregates of silica particles, distributed along the edges and are not connected. The particles are composed of Si and O with minor Ag and Ni. Normalized spot EDS analysis of a region of amorphous silica show 57% Si,

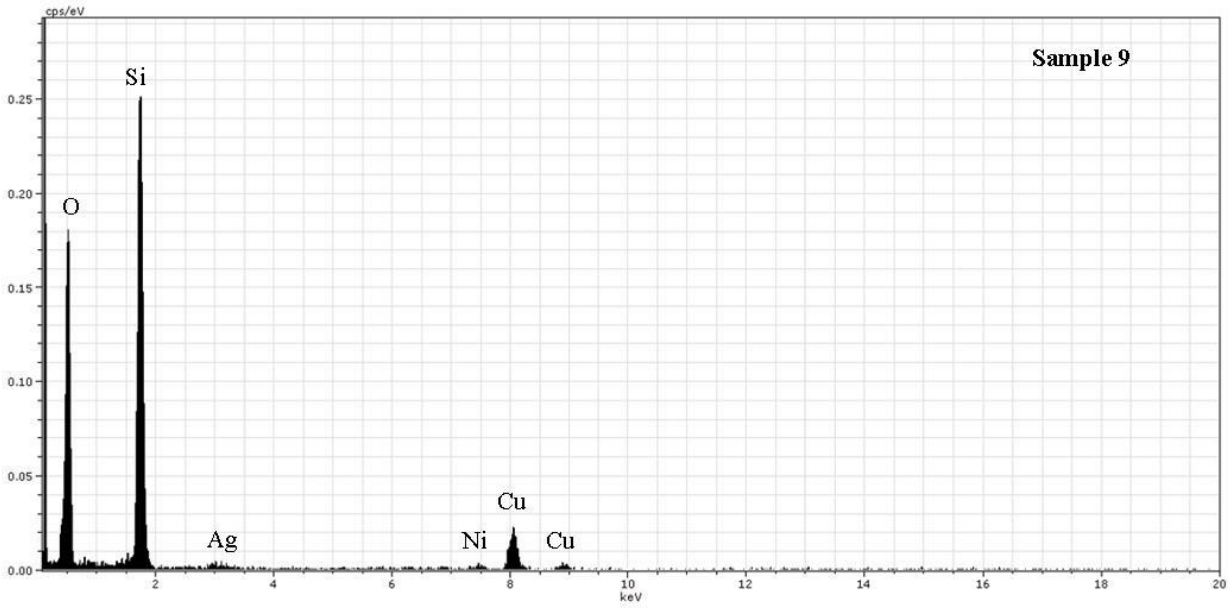

Figure 3.42 EDS spectra of amorphous silica in sample 9. The spot analysis shown corresponds to Figure 3.41c.

41% O, 1% Ag, and 1% Ni (Fig. 3.42). Based on the chemistry and morphology, this phase is interpreted as representing opal or chalcedony.

A porous, Al-rich phyllosilicate phase with continuous lattices is associated with 5% of the silver nanoparticles. The basal spacing value from the image and from the SAED pattern is 3.6 Å (Fig 3.43a). The pores are irregular in shape and are connected to one another; they vary 15 to 80 nm in diameter (Fig. 3.43b) and are distributed evenly throughout the particle except near the contact with the Ag-nanoparticles. On a large scale, the nature of the contact between the Al-rich phyllosilicate and the silver nanoparticles is undulatory, as though the Ag-nanoparticles intrude the phase (Fig. 3.43b). Upon closer examination, the interface is irregular; the nanoparticles near the contact are the smallest in size (5 to 10 nm) grade into larger sizes (25 to 30 nm) farther away from the contact. There appears to be a reaction interface between the

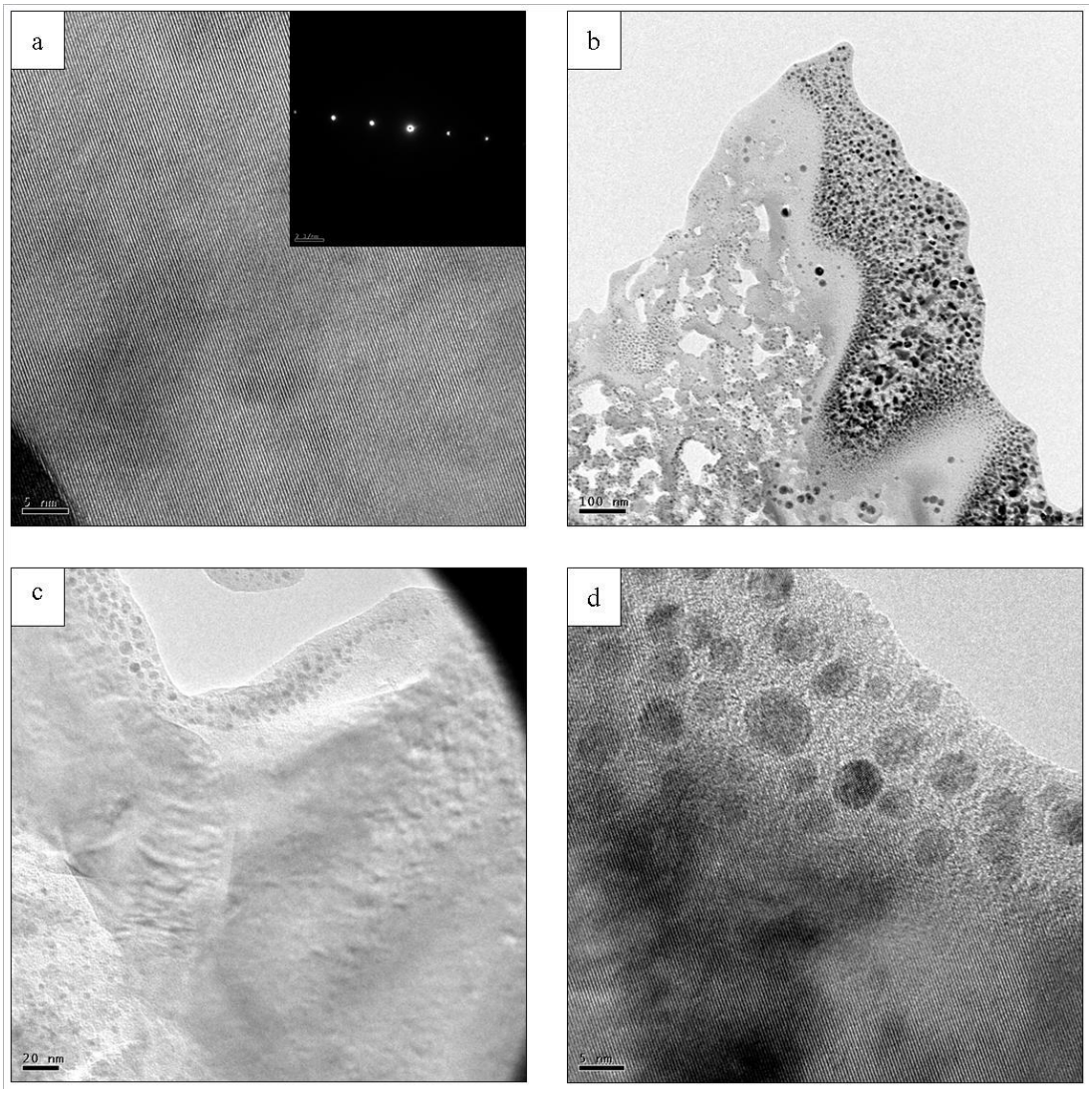

Figure 3.43 TEM brightfield images of kaolinite-like mineral interfacing with Ag-nanoparticles. Image contrast has been altered to improve relief. **(a)** Lattice fringe image of the kaolinite-like phase; inset: SAED pattern. **(b)** Image showing pore detail and undulatory interface with intruding Ag-naoparticles. **(c-d)** Images showing detail of the interface between the kaolinite-like phase and the Ag-nanoparticles.

two phases, as the lattices of the phyllosilicate degrade in quality before disappearing in the Ag-nanoparticle zone (Fig. 3.42c-d). Ag-nanoparticles are also present dispersed within the phyllosilicate in approximately 10% of the concentration in the intruding body of nanoparticles. The Al-rich phase is composed of O, Si, Al, Ag, and minor Ni. Normalized EDS spot analysis of the phyllosilicate show 37% O, 26% Si, 29% Al, 6% Ag, and 2% Ni (Figure 3.44). Based on the

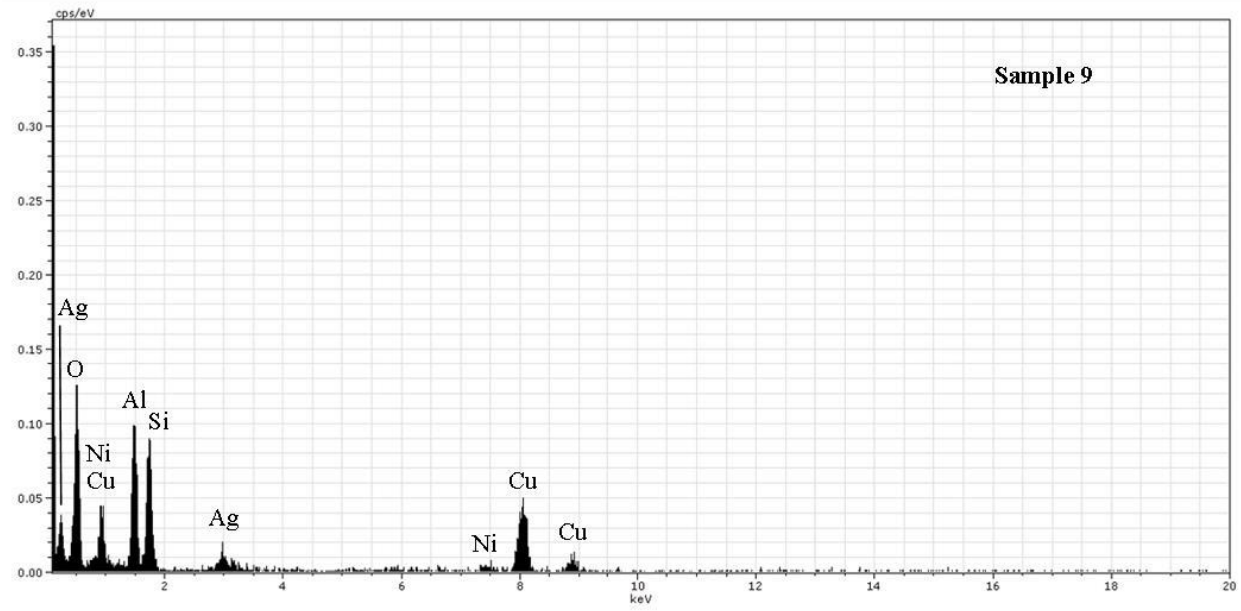

Figure 3.44 EDS spectra of the kaolinite-like phase in sample 9. The spot analysis shown corresponds with Figure 3.43c.

structure and chemistry of the phyllosilicate, it is interpreted as kaolinite or one of its polymorphs, nacrite and dickite, as Al and Si are the dominant cations.

Antigorite comprises approximately 80% of the serpentine in sample 9 whereas chrysotile comprises approximately 20%. The antigorite occurs as broad, platy crystals with a corrugated texture on the surface of the crystal (Fig. 3.45a-b) and lattice modulations along (100) observed viewing down the b-axis (Fig. 3.45c-d). The spacing between modulations varies 20 to 30 Å; the TEM images and SAED patterns for these regions agree well with those published by Da Costa et al. (2008), Wunder et al. (2001), Baronnet (1992), and Veblen (1992). Antigorite is composed of O, Si, Mg, and Fe with minor Ni, Al, Mn, and Ag. Normalized spot EDS analysis of an antigorite crystal shows 28% O, 32% Si, 26% Mg, 7% Fe, 2% Ag, 2% Ni, 2% Al, and 1% Mn (Fig. 3.46).

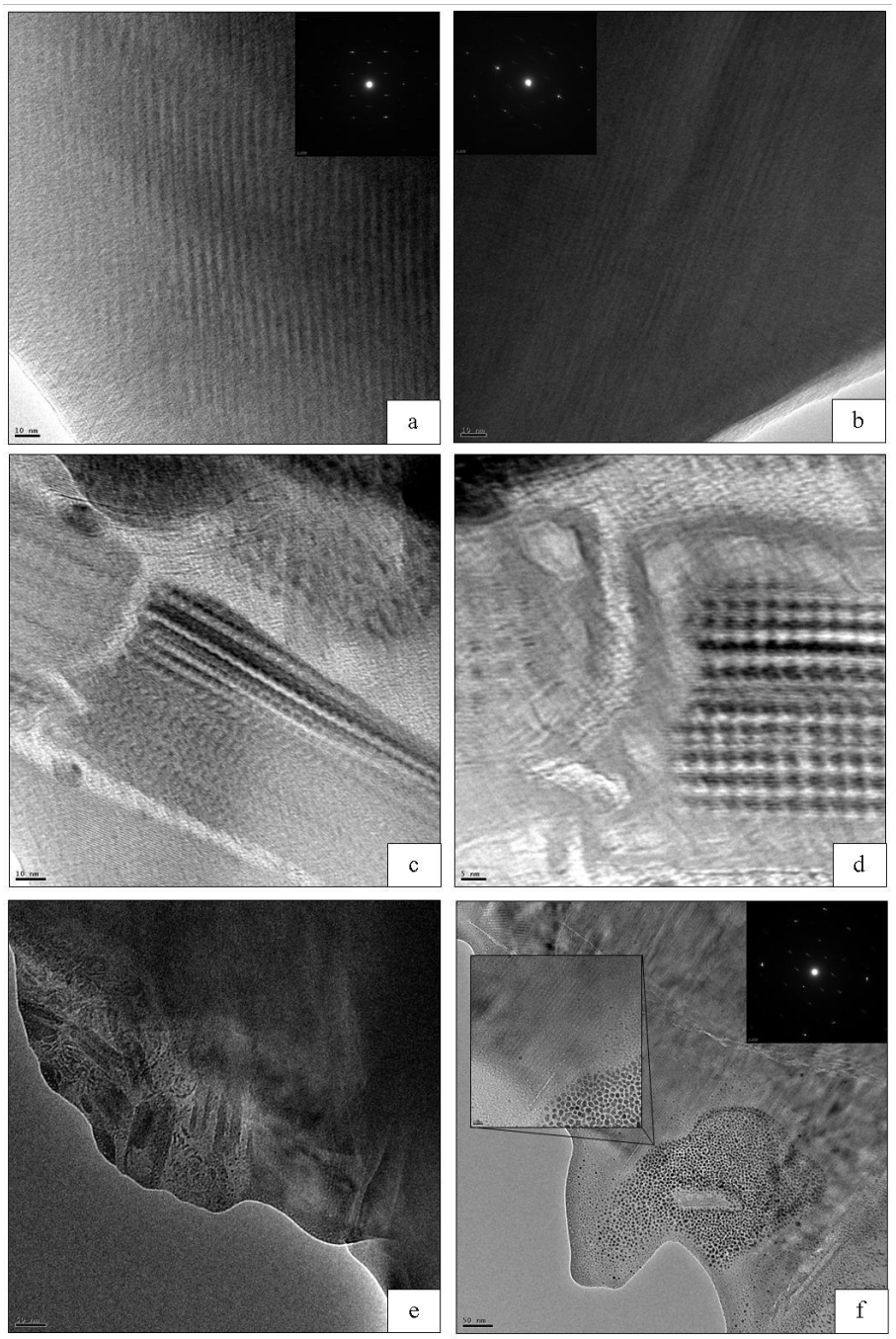

Figure 3.45 TEM brightfield images of regions in sample 9 bearing antigorite and chrysotile. Image contrast has been altered to improve relief. **(a-b)** Antigorite observed down the c-axis; the corrugated crystal surface represents the modulated lattice; inset: SAED patterns. **(c-d)** An antigorite crystal observed down the b-axis, lattice modulations are visible extending along (100). **(e)** Image showing chrysotile nanofibers associated with antigorite. **(f)** Image showing intrusion of Ag-nanoparticles, with an entrained chrysotile nanofiber, into a crystal of antigorite; insets: SAED pattern of the antigorite region (upper right) and higher magnificent image showing detail of the interface between the Ag-nanoparticles and the antigorite crystal.

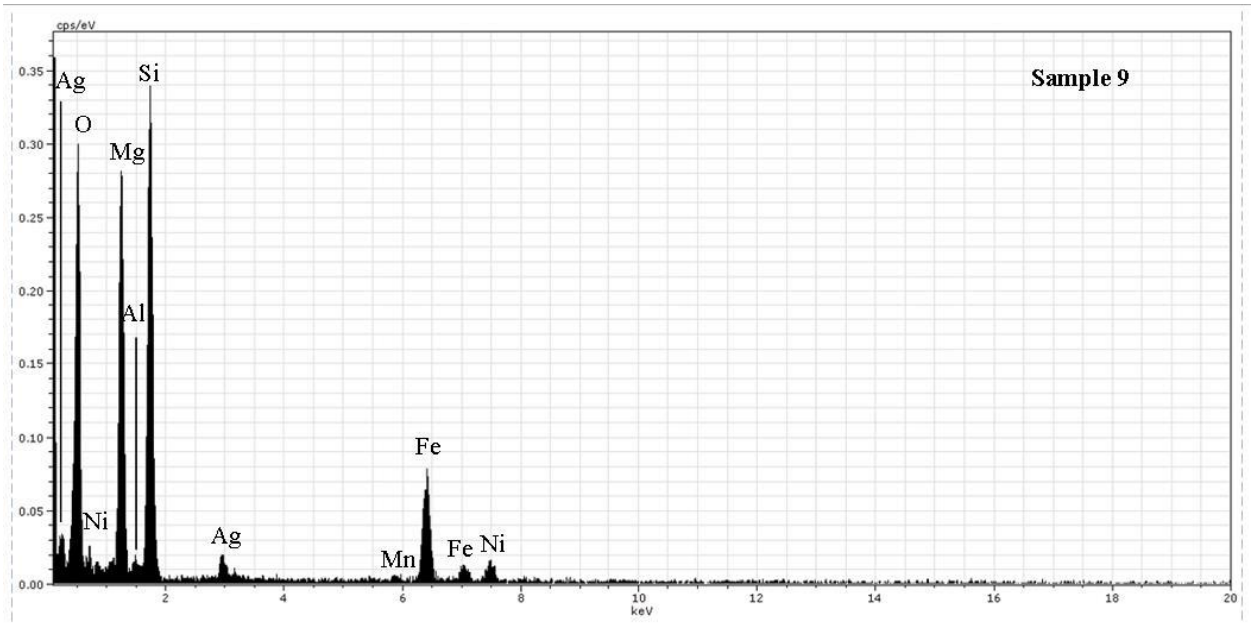

Figure 3.46 EDS spectra of an antigorite crystal in sample 9. The spot analysis shown corresponds with Figure 3.45c.

Chrysotile nanofibers do not occur solitarily, but rather are disarticulated on top of or within the antigorite (Fig. 3.45e); one fiber is also, as mentioned, observed to be entrained within a pseudo-intrusion of Ag-nanoparticles (Fig. 3.45f). Chrysotile is observed within 40% of the antigorite-bearing regions. Chrysotile nanofibers vary 75 to 140 nm in length and 17 to 70 nm in width; lattice fringe images of chrysotile were not obtained due to beam-damage and particle thickness. The nature of the contact between chrysotile and antigorite is irregular and difficult to interpret due to the inability to obtain high resolution images owing to beam damage. It is also a possibility that quality and integrity of these phases and their interfaces with one another was compromised by the ion-milling process, which would also explain the lack of regular particle edges in antigorite crystals.

3.2.10 Sample 10

Sample 10 is composed of a talc-like phase, chlorite, antigorite, and chrysotile. The talc-like phase comprises approximately 75% of the sample, chlorite comprises approximately 10%, antigorite comprises approximately 10%, and chrysotile comprises approximately 5%.

Talc and chlorite occur together in fluffy aggregates of pseudo-lamellar platy particles 50 to 100 nm in length and 5 to 40 nm in width (Fig. 3.47a). Talc is observed both as particles with straight, continuous packages of lattices (Fig 3.47b-c) and as particles with lattices displaying characteristics of crystallographic disorder (Fig 3.47d-f); in both scenarios, the d-spacing of the lattice fringes is 10 Å. Regions with continuous lattices comprise 25% of the talc-like component whereas regions with discontinuous lattices comprise 75%. In the regions with discontinuous lattices, pinch-outs occur throughout the particles over a length of 10 to 15 nm, displacing 1 to 5 lattices; in these regions, the lattices curve slightly to achieve this. Interstratified with 25% of the particles with crystallographically disordered talc are lattices with 14 Å d-spacing interpreted as chlorite; these occur every 2 to 4 talc layers, comprising 10-30% of the talc crystals. In all of the talc and chlorite bearing crystals, an increased resistance to beam damage is observed; this may be a function of the high Ni-content in all of the talc-like and chlorite phyllosilicates in this sample. These regions are composed of O, Si, Mg, and Ni. Spot EDS analysis of a region with continuous lattices shows 22% O, 42% Si, 33% Ni, and 3% Mg, representing a talc-like mineral with near Ni end-member composition (Fig. 3.48). Due to the observed structure and chemistry of these regions, the talc-like component is likely a mixture of pimelite and willemseite with minor nimite present.

Antigorite and chrysotile occur as isolated particles not intermixed with the talc and chlorite aggregates nor with each other. The antigorite is characterized by a corrugated texture on

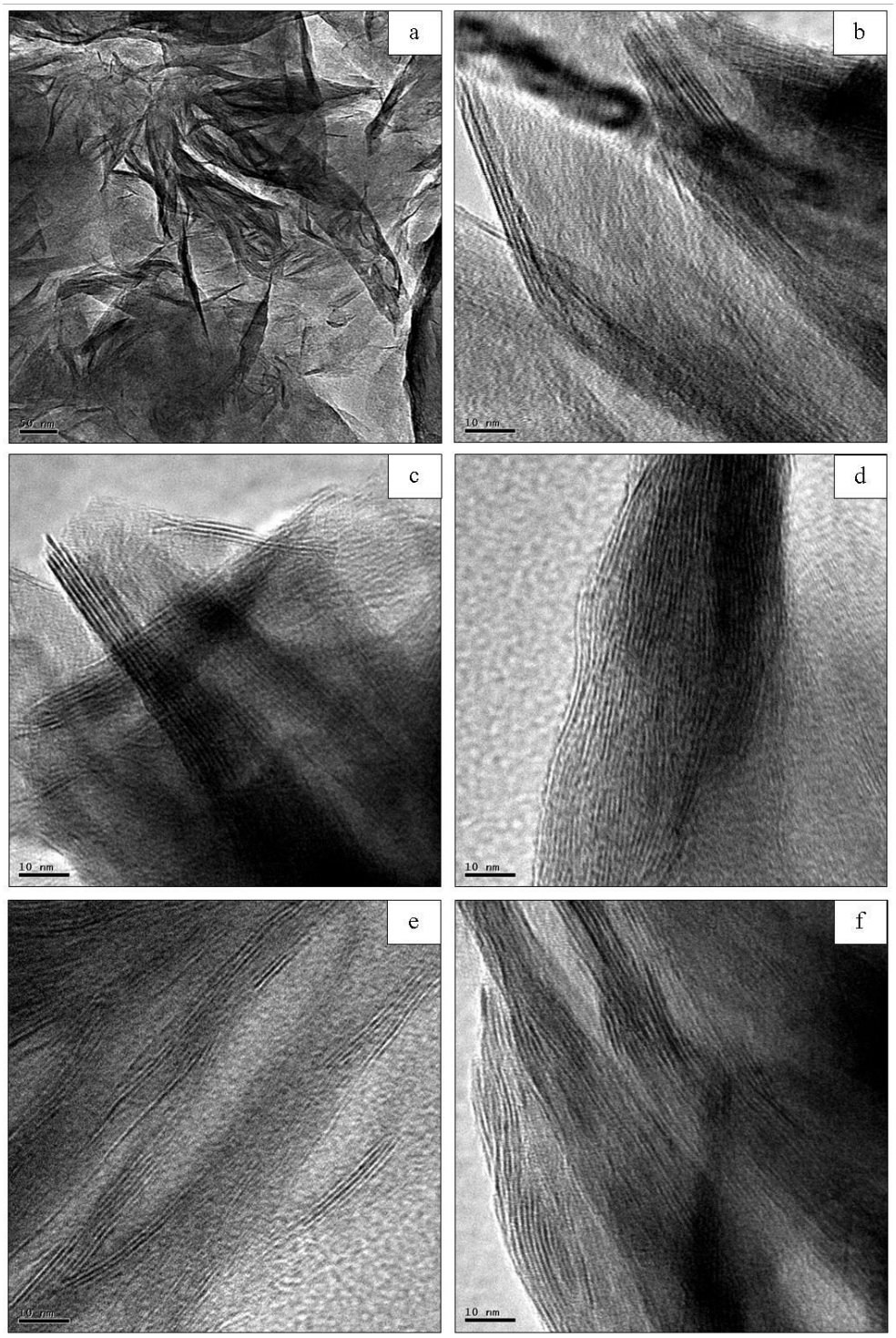

Figure 3.47 TEM brightfield images of a talc-like and chlorite phase in sample 10. Image contrast has been altered to improve relief. **(a)** General texture of the talc and chlorite-bearing regions. **(b-c)** Regions bearing talc-like phases with continuous lattices. **(d-e)** Regions bearing talc-like phases with discontinuous lattices. **(f)** Region bearing interstratified talc and chlorite phases with discontinuous lattices.

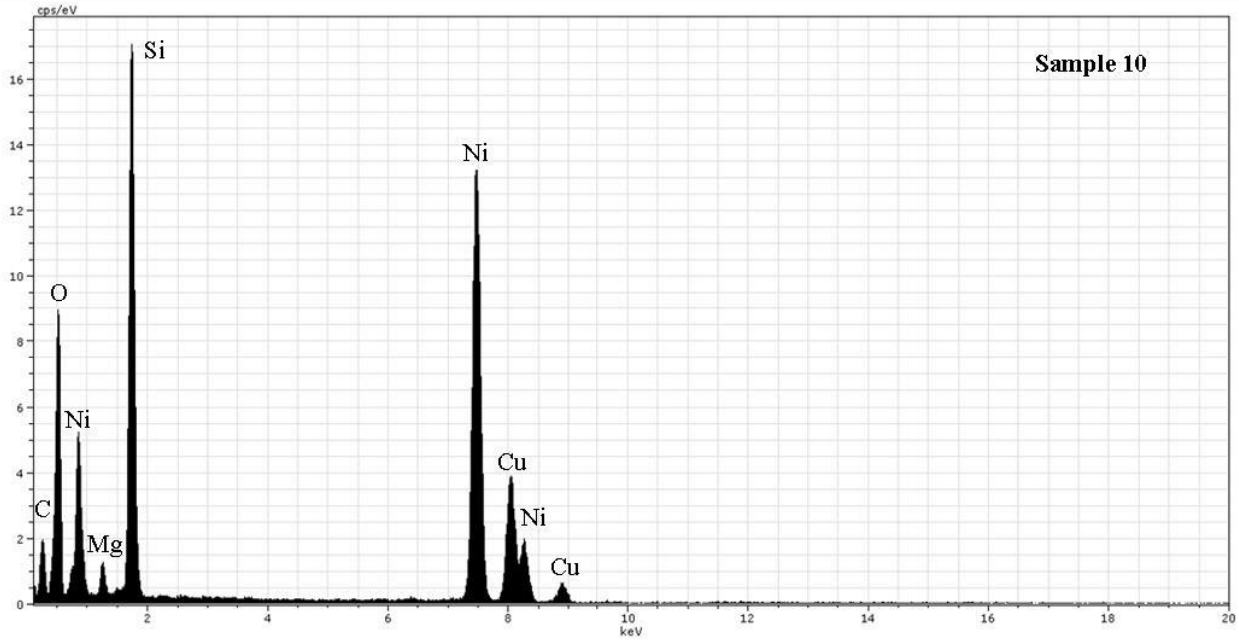

Figure 3.48 EDS spectra of a region of willemseite in sample 10. The spot analysis shown corresponds with Figure 3.47b.

the surface of the crystal which represents lattice modulations extending along (100); the spacing of the modulations varies 17 to 25 Å. The antigorite crystals observed in this sample all have a hachured texture, which likely represents multiple overlapping crystals; this interpretation is supported by the nature of the SAED pattern (Fig. 3.49a-b). The antigorite is composed of O, Si, Mg, Al, and Fe, with minor Ca and Ni. The normalized EDS spot analysis of an antigorite-bearing region shows 37% O, 22% Si, 23% Mg, 12% Al, 3% Fe, 2% Ca, and 1% Ni (Fig. 3.50).

There are very few chrysotile nanofibers present in sample 10. They vary 110 to 200 nm in length, 30 to 40 nm in width, and 15 to 30 nm in wall thickness (Fig. 3.49c-d); the d-spacing of the lattice fringes is 7.2 to 7.5 Å (Fig. 3.49e-f).

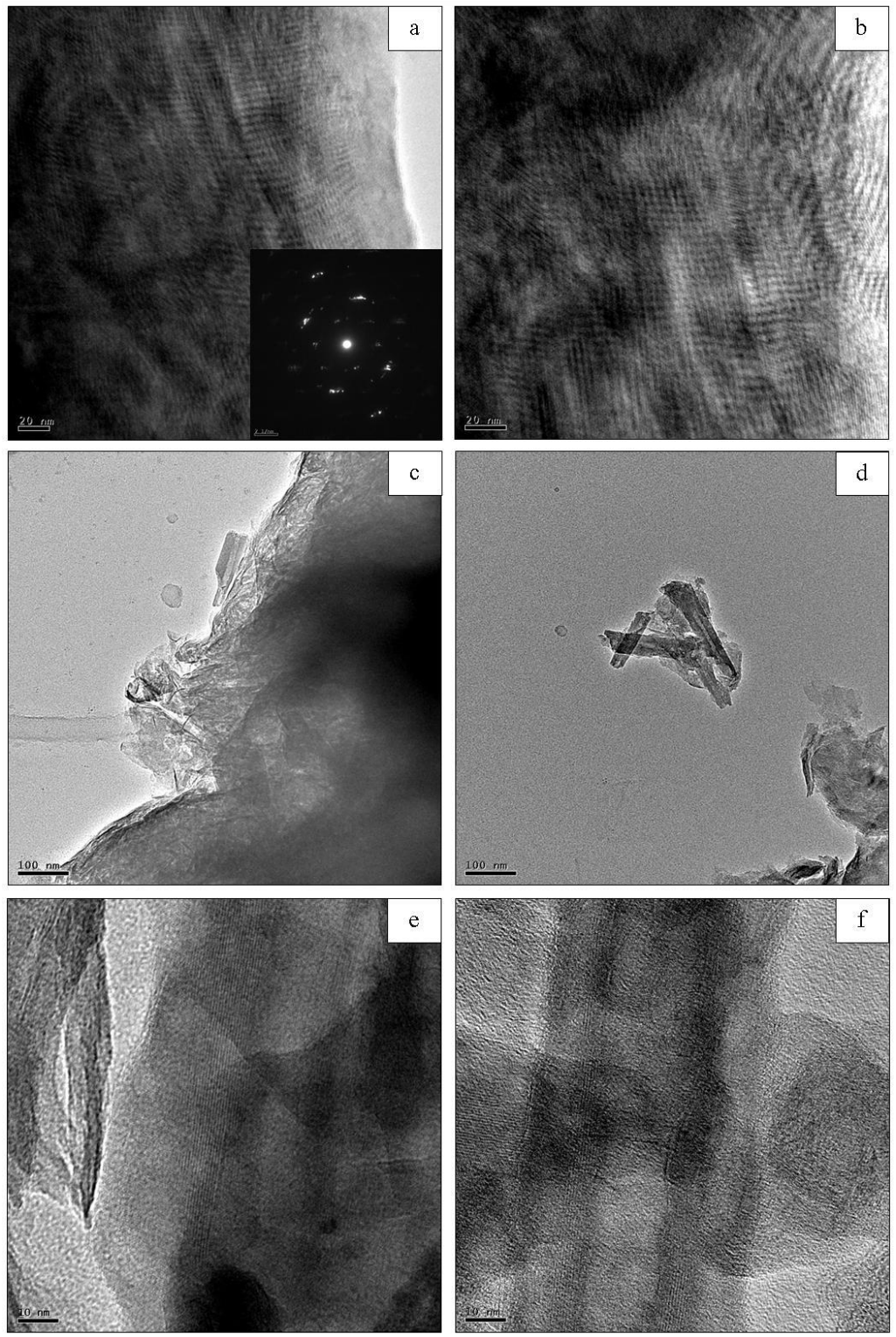

Figure 3.49 TEM brightfield image of antigorite and chrysotile in sample 10. Image contrast has been altered to improve relief. **(a-b)** Antigorite-bearing regions with a hachured texture. **(c-d)** Isolated chrysotile nanofibers. **(e-f)** Lattice fringe images of chrysotile nanofibers.

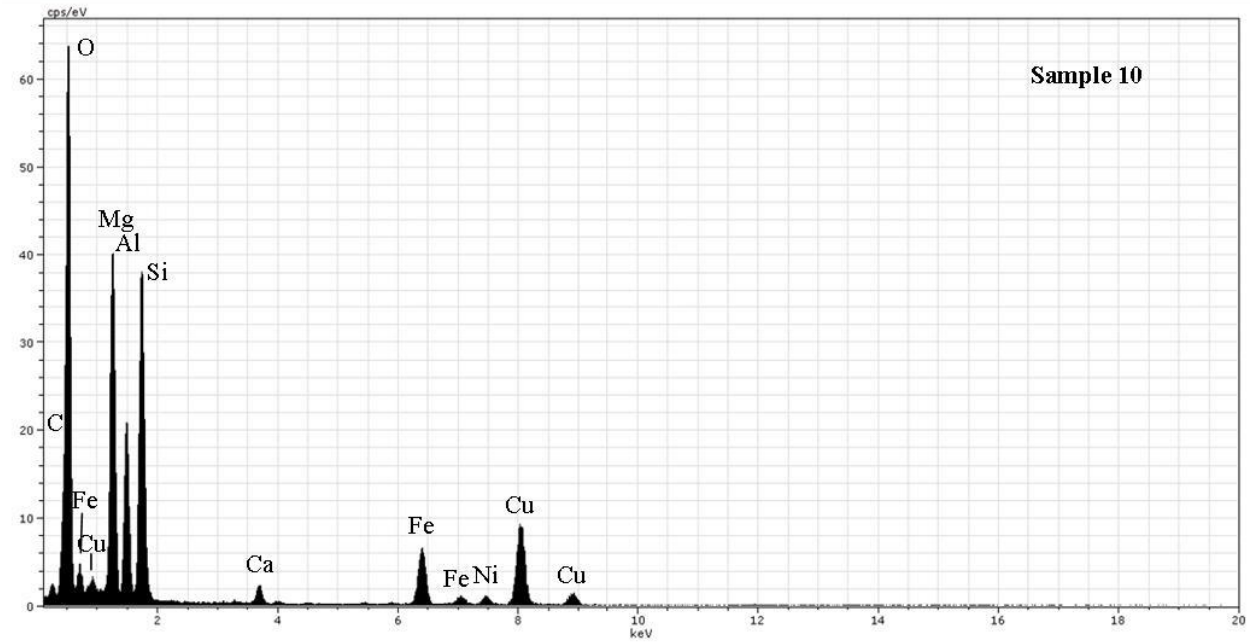

Figure 3.50 EDS spectra of an antigorite-bearing region in sample 10. The spot analysis shown corresponds with Figure 3.49b.

4. DISCUSSION

4.1 Nomenclature

Unless strict identification of members of the kerolite – pimelite series or the talc – willemseite series can be made using XRD alone, the terms ‘talc-like’ or simply ‘talc’ are utilized to refer to all phases with approximately 10 Å basal spacing. TEM and EDS data, when permissible, enabled more precise phase identifications.

‘Serpentine’ is used to refer to the ~7 Å phase in XRD analysis due to the likely presence of two or more polymorphs in a single sample. Tentative serpentine polymorph identifications can be made with heat treatments (see chapter 4.2.2); however TEM elucidated the true nature of the phases.

In the context of nomenclature with respect to Ni-content, mineral naming and identification follow recommendations by Brindley and Maksimovic (1974). For both serpentine and talc-like phases, the variable ‘R’ refers to the Mg- or Ni-containing crystallographic site. Talc – willemseite ($Mg_3Si_4O_{10}(OH)_2$ – $Ni_3Si_4O_{10}(OH)_2$) refer to well-ordered minerals with ~9.4 Å basal spacing. Willemseite will be used when nickel content exceeds 1.5 atoms per formula unit (*apfu*) in the R-site. ‘Kerolite’ – ‘pimelite’ ($Mg_3Si_4O_{10}(OH)_2•H_2O$ – $Ni_3Si_4O_{10}(OH)_2•H_2O$), although not accredited by the International Mineralogical Association (IMA), are useful varietal names for minerals with compositions along the talc – willemseite series but with significant crystallographic disorder, very thin crystals, and additional water. These minerals will likewise be subject to the rule in which ‘pimelite’ will not be used until Ni occupies greater than or equal to 1.5 *apfu* in the R-site. It should be noted that these designations are made with spot EDS analyses and in the inherent error of these analyses should be taken into consideration for strict

nomenclature differentiation. In essence, designation of a mineral belonging to the talc – willemseite series or the kerolite – pimelite varietal series will be based only on EDS data in conjunction with TEM and XRD data as the designation is largely structural in nature.

The serpentine minerals will be treated similarly. Lizardite, chrysotile, and antigorite ($Mg_3Si_2O_5(OH)_4$) will be referred to as such or as nickeloan varieties of themselves until Ni exceeds 1.5 *apfu* in the R-site after which they will be referred to as nepouite, pecoraite, and nickel-dominant antigorite respectively (a nickel antigorite end-member has not yet been named).

The chlorite group, with the general formula $A_{5\text{-}6}T_4Z_{18}$, where A = Al, Fe^{2+}, Fe^{3+}, Li, Mg, Mn, or Ni, T = Al, Fe^{3+}, Si, or a combination, and Z = O and/or OH, is characterized by ~14 Å basal spacing. The Ni-dominant chlorite is known as nimite and has a formula of $(Ni,Mg,Fe,Al)_{11.93}(Al_2Si_6)O_{20}(OH)_{16}$ (Fleischer, 1969) or more simply $(Ni,Mg,Al)_6(Si,Al)_4O_{10}(OH)_8$ (de Waal, 1970) and a basal spacing of 14.2 to 14.3 Å. All ~14 Å specimens analyzed with TEM and XRD have been designated simply as 'chlorite' so far which is appropriate for the general purpose of this study, however, when TEM data and accompanying EDS data show broadly that Ni equals or exceeds 2.6 ions per 18 oxygens (which follows recommendations by de Waal (1970)), the mineral is identified as nimite.

Brindley et al. (1979) use the term 'nickeloan lizardite' or simply 'Ni-lizardite' when referring to those nickel-bearing lizardites that have less than 1.5 *apfu* Ni; this convention is followed here when referring to any Ni-containing talc-like and serpentine minerals containing less than 50% of X sites occupied by Ni but greater than 0% and any chlorite-like mineral containing an appreciable amount of Ni.

4.2 X-ray Diffraction

4.2.1 Lorentz Polarization (Lp) and General Diffraction Characteristics

Correction for Lorentz-polarization (*Lp*) in the talc-like phases must be considered. Correction for the *Lp* factor essentially produces the intensity with which the crystal should have scattered incident radiation but did not due to partial monochromatization of the unpolarized X-rays; it is a function of the size of the unit cell as well as the Bragg angle at which the reflection occurred. Talc has a basal spacing of 9.2 to 9.4 Å, lower than the range of basal spacings recorded in this (9.7 to 10.0 Å) and past studies of the kerolite-pimelite series. After correction for the *Lp* factor, the resulting reflection profiles determined by Brindley and Maksimovic (1974), Brindley et al. (1977) and Brindley et al. (1979) result in a basal spacing of about 9.6 ± 0.05 Å. The *Lp* effect is most noticeable at low-angle reflections and is negligible at higher angles, as reported by Brindley et al. (1977).

In addition to *Lp*-correction, adjacent layer surfaces in end-member talc are situated such that the oxygen atoms partially pack together and bring the layers closer than otherwise would be the case (Rayner and Brown, 1973). Layer misfit and disordered stacking in the kerolite-pimelite series does not allow for such close-packing and would further increase apparent basal spacing beyond the *Lp* effect. After both factors have been taken into account, basal spacing for the kerolite-pimelite series is not ~10 Å, but rather in the normal talc range. An interesting phenomenon is the apparent disagreement between *Lp*-corrected values and measurements from TEM images and SAED patterns that were approximately 10 Å. The exact reasons for this disagreement are unknown but may be related to differences in water in the XRD instrument, which does not have a controlled atmosphere, and the high vacuum environment of the TEM

column. A complexing factor may relate to the very small particle size of numerous minerals observed in these samples which is often < 200 nm and thus reflection broadening is very much expected, complicating reflection position determination.

An indicator of disordered stacking among phyllosilicates is the presence of broad two-dimensional *hk* diffraction bands characteristic of random-layer stacking. The powder pattern of a random layer stacking sequence will consist of two types of reflections: crystalline-type reflections of the type (00*l*) and diffuse two-dimensional lattice reflections of type (*hk*); there will be no discrete reflections of type (*hkl*) (Warren, 1950). These two-dimensional reflections have been noted in the kerolite-pimelite series by Brindley et al. (1977) and Brindley et al. (1979) as well as in minerals of the lizardite-nepouite series (Brindley and Wan, 1975). Such diffraction characteristics have been well noted in numerous other phyllosilicates (Bailey 1987, 1988) and are referred to as 'streaking'. To be consistent with previous diffraction studies of nickel phyllosilicates, the nomenclature of Brindley et al. (1977, 1979) and Brindley and Wan, (1975) is used (i.e. 'two-dimensional diffraction bands'). For example, in the range of 2θ values collected in this investigation, the talc (02,11) is the prominent two-dimensional diffraction band; indicating intralayer disorder within the material (as opposed to interlayer disorder which would be evidenced by two dimensional diffraction bands associated with the (001) reflection). This is consistent with Kogure et al. (2006) who found that interlayer displacement in disordered talc was relatively ordered whereas intralayer displacement is almost completely disordered. Broadness of any disordered talc (001) reflections is a function of both its very fine-grained nature and its interstratification with serpentine and possible other phases.

4.2.2 Serpentine Dehydroxylation

The temperature at which the serpentine minerals dehydroxylate varies with species; however, there is an apparent degree of disagreement in the literature about the temperatures at which these reactions occur. Wells et al. (2009), in their XRD analysis of 'garnierite' from New Caledonia stated that the complete collapse of the 7.36 Å reflection at 7.24 (2θ) (the serpentine 002 reflection) after having been heated to 550 °C for 2 hours, confirmed the presence of serpentine in both samples. Brindley and Wan (1975) reported a dehydroxylation initiation temperature of 450 °C for lizardite and nepouite, Trittschack et al. (2012) note that lizardite basal reflections decrease in intensity between 500 and 550 °C, and Brindley and de Souza Santos (1971) and Perez-Rodriguez et al. (2005) in their examinations of antigorite noted that dehydroxylation did not commence until 600 °C.

In contrast, Gualtieri et al. (2012), Dlugogorski and Balucan (2014), and Viti (2010) report that serpentine dehydroxylation takes place between 550 and 800 °C, the derivative thermogravimetric and differential thermal analyses in these studies reported dehydroxylation for antigorite occurs between 700 and 715 °C, for lizardite between 708 and 714 °C, for polygonal serpentine between 685 and 691 °C, and for chrysotile 650 and 654 °C, respectively. It is obvious that the thermal stability for these minerals varies with composition, but the author to author disagreement is a source of confusion.

It is apparent that due to these disagreeing values, X-ray diffraction of heat-treated serpentine-bearing samples cannot be used alone to determine serpentine species; however, the TEM data aids in this interpretation. Complete or near complete collapse of the serpentine basal reflections in the study material after being heated at 550 °C for 30 minutes occurred in samples 2, 4, 5, and 7. Persistence of the basal reflection occurred in samples 1, 3, 6, 8, 9, 10. Samples 4,

5, and 7 (no serpentine was found with TEM in sample 2) all contain lizardite and chrysotile (along with minor chlorite in 4 and 7 and kerolite in 5) whereas samples 3, 8, 9, and 10 (no serpentine was found with TEM in sample 1 and sample 6 contained lizardite, chrysotile, and pseudo-polygonal serpentine) all contain antigorite (Figs. 3.1-3.10).

From these data, it can be broadly stated that the lizardite-bearing samples experienced significant dehydroxylation at 550 °C whereas antigorite-bearing samples did not. This is consistent with data reported by Brindley and Wan (1975), Brindley and de Souza Santos (1971), Perez-Rodriguez et al. (2005) and Trittschack et al. (2012).

In samples 4 and 7, which are comprised almost entirely of serpentine, a broad peak at approximately 6° (2θ) with 14.2 and 14.7 Å d-spacing, respectively, developed when heated to 550 °C. Brindley and Wan (1975) and McKelvy et al. (2004) noted the appearance of a broad reflection developing between 580 and 800 °C with a d-value of 11.5 to 14.7 Å at $2\theta = 6°$ in their lizardite samples the former referred to as a long-spacing (LS) phase coinciding with rapid decay of original basal reflections (Figs. 3.4 and 3.7). McKelvy et al. (2004) call this phase 'meta-serpentine' and associate it with the doubling of the 7.336 Å interlamellar spacing along (001). The LS phase is a chlorite-like arrangement or rather like chlorite after the first stage of dehydroxylation. The LS phase is notated as chlorite in the pattern figure labels for clarity (Figs. 3.4 and 3.7). How the presence of this phase varies between serpentine polymorphs is unknown, however, it was only found here in the samples dominated by lizardite.

4.2.3 Comments on Miscellaneous XRD Results

In terms of solvation with ethylene glycol and glycerol, the phyllosilicates had virtually no reaction, indicating the absence of expandable phases. The exception to this is sample 6,

where reflections of 22 to 27 Å appeared in the 3.2 to 4° (2θ) range upon glycerol solvation. These reflections were not visible in the ethylene glycol solvation nor in the heat-treated samples. They likely represent small amounts of interstratified smectite-like material. The presence of a smectite-like material is not unusual as Wells et al. (2009) found a significant amount of smectite in their study of 'garnierite' material from the Goro nickel lateritic deposit in New Caledonia. Ethylene glycol solvation produced no change in the pattern indicating the absence of expandable phases in that particular powder mount indicating the considerable heterogeneity of the phases. A smectite phase was not observed with TEM analysis.

Glycerol solvation produced diminished reflections in many of the samples. This was due to apparent over-saturation with glycerol or pooling on the surface of the clay material. Another feature that occurred in all samples upon glycerol solvation was the generation of a poorly defined reflection in the approximately 15° to 19.5° (2θ) range leading up to reflections/bands in the approximately 20° (2θ) range. This is interpreted to represent the interaction of the large glycerol molecule and the extremely fine-grained material.

The XRD pattern for sample 10 showed the presence of enstatite and hornblende in addition to the phyllosilicates. These phases are interpreted to represent residual primary harzburgite. Pyroxene and amphibole were also found by Wells et al. (2009) in Ni-phyllosilicate material from the Goro lateritic nickel deposit in New Caledonia.

4.3 Comments on TEM and EDS Data Interpretation

Mineral identifications using TEM data are based on crystal habit, directly measured lattice-spacings, selected area electron diffractions (SAED), and beam-damage susceptibility. Due to the high incidence of beam damage in hydrous phyllosilicates, both image and

accompanying diffraction are not always obtainable. This can sometimes be mitigated by using the fast Fourier transform (FFT) of the image, which produces a pattern similar to an SAED. Lattice d-spacing measurements can be improved in accuracy by measuring from the FFT in addition to directly measuring the profile on the image. Unless otherwise stated, "d-spacing" refers to the basal spacing of the phyllosilicate species (00*l*).

Most of the phases with ~10 Å basal spacing among the sample material have a characteristic platy, lamellar morphology with crystallographic disorder in the form of turbostratic stacking ranging from severe (Fig. 3.14) to minor (Fig. 3.47). Features that indicate crystallographic disorder include lattice discontinuities ("pinch-outs"), aggregated, small, randomly oriented crystals, quasi-braided textures, lattice curvature, and diffuse rings on SAED images in highly magnified regions rather than discrete reflections or the complete absence of reflections, for which FFT images supplanted (Fig. 3.11). Species identification of the ~10 Å phases must be further aided by EDS analysis; therefore the term "talc-like" for kerolite-pimelite series minerals or "talc" for talc-willemseite phases is used, the former distinguished by the aforementioned crystallographic disorder characteristics whereas the latter is distinguished by larger crystals with ordered lattices.

Distinction between serpentine polymorphs is based on a few simple criteria. Lizardite, chrysotile, and antigorite all have approximately 7 Å basal spacing, but crystal habit varies among the polymorphs. Chrysotile is the simplest to identify based on its tubular habit. Antigorite and lizardite can be difficult to distinguish from one another at times as the antigorite in the sample material is platy in morphology rather than lath-like. Unless the crystal displays characteristic corrugated morphology and lattice fringe modulations, it will not be referred to as

antigorite but rather lizardite unless other data conclusively prove otherwise. One of the purposes of the XRD analysis is observe the behavior of the serpentine basal reflections upon heating; samples that clearly maintain these basal reflections at above 550°C are likely antigorite rather than lizardite. In this way, XRD can lend credence to an otherwise ambiguous TEM identification of serpentine. The identification of lizardite polytypes using TEM requires viewing parallel to the layers along two or more directions depending on how many layers the polytypes have (Dodony and Buseck, 2004). As the samples in this study were not oriented, polytype identification was not possible.

In some of the samples, regions that appear to contain polygonal serpentine exist. This identification is made with caution as the observed particles could be chrysotile as viewed down the long axis of the tube; the presence of characteristic flat sector zoning associated with polygonal serpentine is the best way to make the distinction (Fig. 3.29).

Chlorite has a characteristic basal spacing of approximately 14 Å. The term "chlorite" will be used to refer to this phase unless EDS aids in more refined phase identification. In the sample material, some of the chlorite has a similar morphology to the talc-like species, however, the former is observed to usually have better crystallographic order as well as higher resistance to beam damage due to lower water content.

In all samples, significant amounts of carbon and/or copper are detected. These elements are interpreted to originate from the sample substrate – copper grids (ion-milled samples) and lacy carbon copper grids (grain mounted samples). All EDS analyses were conducted as spot analyses and thus have spatial resolution limitations and error well-recognized with this type of analysis.

Although phyllosilicate chemistry of the samples was largely consistent with that of Ni-bearing talc-like, serpentine, chlorite minerals, other trace elements were detected. Cl and S, observed in samples 1, 4, and 7 represent residual Cl and S incorporated into the parent rock during serpentinization (Kendrick et al., 2013; Debret et al., 2014). Ca noted in samples 2 and 10 are likely residual from primary harzburgite minerals. The Cr detected in samples 3 and 4 is expected as chromite is a commonly associated with the New Caledonian laterite deposits as is the Mn detected in samples 3, 4, and 9 (Dublet et al. 2012). Sample 4 and 9, as noted in the hand-sample descriptions, had gray arborescent mineralization on the phyllosilicates; these are interpreted as representing Mn-oxides.

4.4 Mineralogy

4.4.1 Talc-Willemseite and Kerolite-Pimelite

XRD analyses show that a talc-like component is present in samples 1, 2, 5, 9, and 10 (Figs. 3.1, 3.2, 3.5, 3.9, and 3.10). The talc (001) and (003) reflections for these samples were quite broad, reflecting both crystallographic disorder and very small particle size. The two-dimensional diffraction bands (02,11) and (13,20) were also always present, reflecting the turbostratic interlayer stacking among the talc-like component (Brindley et al., 1977; Brindley et al., 1979). These features were observed with TEM as well, where Ni-kerolite was observed in samples 1, 2, 3, 5, and 10, pimelite in samples 2 and 10, and willemseite in sample 10. The discrepancy in phase distribution observed with XRD and TEM is interpreted as a function of both the very small particle size (not always detectable with XRD) and the significant heterogeneity of the Ni-phyllosilicates.

With TEM, the talc-like phases were readily apparent as pseudo-lamellar platy aggregates of small crystals with approximately 10 Å basal spacing, displaying commensurate pinch-outs, quasi-braided textures, and lattice curvature (e.g. Figs. 3.11 and 3.14). These phases were also extremely beam-sensitive in comparison to the serpentine phases owing to their higher water content. It was also observed that pimelite and willemseite were slightly more resistant to beam damage than the less Ni-rich talc-like phases, which may potentially be a function of Ni content. The material interpreted as willemseite in sample 10 is characterized by orderly, prominent, and more beam-resistant lattices. In contrast to the kerolite-pimelite phases, the crystals with approximately 10 Å basal spacing were also large in size.

It is interpreted that the minerals of the kerolite – pimelite series resulted from the laterization process as secondary phyllosilicates after primary lizardite and chlorite. This is indicated by the crystallographic disorder and relative Ni-enrichment of these materials compared to the primary phases. Although no nepouite (Ni-rich lizardite) was observed in this investigation, it is broadly confirmed to be a significant component of the Ni-rich material in New Caledonia and also similarly disordered with respect to primary low-Ni lizardite (Brindley and Wan, 1975).

Kerolite is fundamentally different from talc in terms of formation. Whereas talc is a product of hydrothermal alteration or low-grade metamorphism, kerolite occurs in low-temperature weathering horizons crystallizing from an initial gel-like state (Brindley et al., 1977). The association of willemseite in sample 10 with antigorite and chlorite are indicators that this sample may have originated close to the contact of the underlying lithologies, the heat-produced from the obduction process facilitating the alteration to an ordered Ni-talc.

A phase having a basal spacing of 4.5 to 5.0 Å was observed in the TEM analysis of samples 3 and 4. This phase is interpreted to potentially representing half of the normal thickness of a normal (001) talc spacing and thus may be the (002), observed because of local thickness and chemical composition variation. This phase comprised very minor percentages of samples 3 and 4 and was not detected with XRD. An alternative explanation of a more complex interstratification scheme where brucite-like layers or other oxyhydroxide layers exist may be the case. Brucite makes sense due to the formation conditions of primary lizardite, as discussed in chapter 4.5.

4.4.2 Chlorite

Chlorite has been reported in New Caledonia by Kato (1961), Manceau et al. (1985), and Wells et al. (2009). The chlorite textures were not commented on by these authors although the chlorite-bearing samples were noted to be low in Fe and thus referred to as clinochlore ($Mg_5Al(AlSi_3O_{10})(OH)_8$). In our material, chlorite appears to have two distinct textures: well-ordered and disordered. Sample 3 contained the largest amount of chlorite, with samples 4, 7, and 10 containing only minor amounts usually interstratified with other phases. Sample 3 is the only one in which chlorite was observed with XRD in the untreated and air-dried run. Upon heating to 550 °C, this reflection significantly increased in intensity. This increase in intensity is potentially related to both an increase in crystallinity and to the contribution of the so-called 'long-spacing' or 'metamorphic-serpentine' phase that occurs when lizardite is heated to between 580 and 800 °C noted by Brindley and Wan (1975) and McKelvy (2004), contributing an 11.5 to 14.7 Å reflection at $2\theta = 6°$.

From TEM observations, sample 3's chlorite occurs as large crystals with well-ordered lattices. In contrast, the localized chlorite-bearing regions in samples 4, 7, and 10 displayed crystallographic disorder similar in style to the kerolite-pimelite phases.

Chlorite is an accessory serpentinization mineral that develops at the expense of magnetite in the presence of aluminum (Schwartz, et al., 2013). As will be discussed in later, magnetite is present in samples 3 and 10 due to a low-temperature serpentinization regime (50 to 300 °C), the presence of both magnetite and chlorite in these samples indicates that the parent rock was largely forsteritic with a minor aluminum component, which is the observed normalized chemistry in these samples. Manceau et al (1985) found well-crystalized nepouite (Ni-dominant lizardite) growing on chlorite crystals in veins cutting the silicified and lateritic zones. The well-ordered nature of the chlorite in sample 3 is likely due to it being a primary serpentinization phase (hence why secondary serpentines are growing on it). This is plausible if, again, the parent rock was significantly iron-deficient and had enough aluminum present so that both chlorite and magnetite were able to form.

The small amounts of disordered chlorite in samples 4, 7, and 10 may have formed in a process similar to that of kerolite-pimelite minerals, through laterization processes with Al-bearing fluids. Alternatively, primary chlorite may simply have been altered to secondary chlorite in a recrystallization process in response to weathering.

4.4.3 Lizardite

Two-dimensional hk bands were observed in samples in which no talc-like phase appeared to be present, only a serpentine phase. The patterns in which this occurred (samples 4, 6, and 7) are the ones which contain lizardite (one region of a particle with 6 Å d-spacing is

noted as lizardite in sample 5, however, because of the anomalous basal spacing, this may represent a degraded or altered chlorite). These bands may reflect interlayer disorder as they do for kerolite-pimelite minerals, but as observed with TEM, the lizardite does not possess the same style of disorder (turbostratic stacking) as the talc-like minerals do. A more likely cause of poorly defined reflections in the lizardite-bearing samples is the lenticular layer separations observed within them.

These separations are caused by cation diffusion; regions containing these separations also contain diagnostic mottled contrast, which is due to strain caused by heterogeneity induced by diffusion of cations and/or dehydration that is associated with the growing, lens-like separations of layers (Ahn et al. 1986; Pecor, 1992). These layer separations commonly occur along (001), possibly nucleating at original sites of structural defects or hydrated interlayers (Ahn et al. 1986; Pecor, 1992).

The regular occurrence of these features in the lizardite-bearing samples is likely a reflection of both primary serpentinization (associated with primary olivine and pyroxene defects) and secondary alteration where elements such as Ni diffused out of the lizardite structures into secondary phyllosilicates.

4.4.4 Chrysotile and Polygonal Serpentine

Chrysotile was observed with TEM in all but three samples (1, 2, and 3) as readily apparent fibrous particles that vary 50 to 700 nm in length. The particles were low in Ni, preventing the designation of pecoraite, the Ni-chrysotile end member. Sample 8 was the only one in which the material removed from the rock was visibly fibrous in habit to the unaided eye;

not unexpectedly, sample 8's diffraction pattern had the highest resolution in terms of crystallographic order.

Most of the circular sections in chrysotile-bearing regions represent the chrysotile observed down the fiber axis; however, particles with sector-zoning associated with polygonal serpentine do occur. Polygonal serpentine forms when additional growth of chrysotile is barred and further microstructural evolution demands something new. The flatter curvature of the outer layer of highly developed chrysotile provides a substrate favorable for the attachment and growth of planar serpentine (Evans, 2004). Due to beam damage, high resolution images were not possible and therefore these particles will require more examination to make a more certain identification.

4.4.5 Antigorite

The presence of significant amounts of antigorite in the sample material is a new observation in New Caledonian 'garnierite' deposits. Samples 3, 8, 9, and 10 displayed crystals of antigorite with the characteristic corrugated morphology on the surface of the crystal, which represent periodic lattice modulations extending in the (100) direction. An image taken looking in the (010) direction in sample 9 shows the modulations in great detail; this viewing direction is difficult to obtain due to the induced (001) orientation that accompanies a grain-mounted sample. Sample 9 was ion-milled making this viewing direction was possible.

Identification of the serpentine polymorphs in the sample material was difficult due to the fine-grained nature of the phyllosilicates and their intimate intermixing with other phases. However, as discussed previously, the state of the basal spacing reflections at when heated to 550 °C was successful in partially delineating the serpentine phases, especially determining

whether the phase was lizardite or antigorite dominant. Due to its higher temperature stability, the basal reflections of all of the antigorite-bearing samples (confirmed later with TEM) did not suffer loss of their basal reflections whereas the lizardite-bearing samples either suffered complete or partial collapse of (002) and (004).

4.4.6 Amorphous Silica

Amorphous silica is found in samples 1 and 9 both alone and acting as the matrix for the silver nanoparticles. The presence of amorphous silica is not unusual as silica-rich fluids were the primary tropical weathering agent, facilitating the crystallization of kerolite-pimelite minerals from an initial gel-like state and also chrysotile.

Quartz reflections were observed in almost all of the samples XRD patterns, indicating that crystallographic order does exist in a silica phase. This is observed somewhat with TEM; sample 9's amorphous silica showed a random granular texture indicating a semblance of crystallographic order.

Sample 5 is interpreted as almost entirely Ni-chalcedony ('chrysoprase') (Fig. 3.26), a cryptocrystalline form of quartz with inclusions of kerolite-pimelite owing to the nature of its diffraction (Fig. 3.5). This 'chrysoprase' phase was not observed with TEM possibly due to issues producing the required suspension so that only kerolite and pimelite inclusions were represented on the grids. These observations are consistent with the character of the hand sample; the green material was significantly harder and more difficult to remove from the host rock with the X-ACTO knife and steel probe.

4.4.7 Silver and Gold

Silver occurs as discrete nanoparticle spherules in samples 1 and 9, with the latter possessing far greater amounts. In sample 9, the textures of the Ag-nanoparticles are complex (Fig. 3.39). The 'nano-porphyroblastic' texture observed is essentially consistent with Ostwald ripening phenomena. Ostwald ripening describes the evolution of an inhomogenous structure (can be solid or liquid) over time. It is a thermodynamically driven process that occurs to produce more energetically stable large particles from smaller particles due to surface area to volume ratios (Voorhees, 1984). Saunders (1990, 1994, and 2012) and Burke (2015) found very similar textures in colloidal gold deposits (also found in association with amorphous, colloidal silica) in epithermal systems.

The nanoparticles in both samples are found within a matrix of amorphous silica. Amorphous or cryptocrystalline silica are known to be a component of New Caledonian Ni-laterites; indeed, nearly all of the sample material possessed silica veins and produced quartz reflections in the XRD analysis. These features represent the circulation of silica-rich fluids that may have played a central role in the laterization process; secondary serpentine and talc-like minerals are thought to have crystallized from an initial gel-like state aided by the circulation of these fluids (Manceau et al., 1985; Brindley et al., 1977). Although only a few studies have been conducted Burke (2013) on Michigan copper and Burke (2015) on epithermal hydrothermal gold, nanospherule textures seem to be associated with higher temperature deposition. Whether the silver was deposited in earth surface conditions or may reflect some low temperature epithermal deposition, similar to quartz deposition described by Saunders and others is unclear. The silver was likely a component of the circulating silica-rich fluids that may have contributed to weathering, although from where it was originally derived cannot be determined with the present data set.

Silver has not been reported to be a component of Ni-laterite deposits in New Caledonia; the reasons for this are still unclear. Due to the limited amount of sample material analyzed, the percentage silver comprises in the ore material could not be determined; however, it is likely small. As it was only found in association with the amorphous silica, it may be difficult to detect using normal analytical techniques and only ion-milling revealed the spherules. In addition, the Ag-spherules are far too small to be detected with XRD, especially if they are only a few weight percent.

Gold was observed in sample 3 not as discrete particles but apparently as a component of the phyllosilicates. It was only detected in minor to trace amounts (0.003 to 0.009 wt. %) so further exploration is needed to see how ubiquitous it is. Its origin is likely similar to that of the silver nanoparticles but in much smaller quantities not conducive to forming discrete particles.

4.5 Assemblage-Based Metamorphic Regime Reconstruction

The nature of the sample collection precludes spatial differentiation of the observed phases; however, assemblage-based inferences can be made. Table 4.1 summarizes the phyllosilicate phases observed in each sample for each analysis.

Although it is often thought otherwise, antigorite and lizardite are not polymorphs in the strict sense and it is abnormal for them to coexist outside of a multigenerational system; antigorite has a lower H_2O content, a lower octahedral occupancy, and a higher SiO_2 content related to the modulated nature of its structure (Zussman et al., 1957; Dungan, 1979). Lizardite and chrysotile are, however, polymorphs. Coleman (1971) refers to lizardite and chrysotile as the ‘pseudomorphic serpentines’, differing in mineralogy, texture, and petrogenesis from ‘antigorite serpentine’. The

Table 4.1 Summary of phyllosilicate phases observed using XRD and TEM with EDS. Mineral symbols follow recommendations by Kretz (1983): Tlc = talc, Srp = Serpentine, Chl = Chlorite, Ker = kerolite, Pim = pimelite, Liz = lizardite, Ctl = chrysotile, Atg = antigorite, Wlm = willemseite, P.Srp = polygonal serpentine. 'Ni-' prefix indicates nickel bearing varieties that are Mg-dominant.

Sample	XRD*	TEM and EDS
1	Tlc, Srp	Ni-Ker, Pim[§]
2	Tlc, Srp[†]	Pim
3	Chl, Srp	Ni-Chl, Ni-Atg, Ni-Ker
4	Srp[†]	Ni-Ctl, Ni-Liz, Chl[§]
5	Tlc, Srp[†]	Ni-Ker, Liz[§], Ctl[§]
6	Srp[†]	Ni-Liz, Ni-Ctl, P.Srp[‡]
7	Srp[†]	Ctl, Liz, Chl[§]
8	Srp	Ni-Atg, Ni-Ctl
9	Tlc[‡]	Ni-Atg, Ni-Ctl
10	Srp, Chl	Pim, Wlm, Atg[§], Ctl[§], Chl[§]

*Phases observed from air-dried and untreated analyses.

†Serpentine basal reflections completely or partially collapse at 550°C

‡Tentative identifications

§ Phase in trace or very minor amounts

pseudomorphic serpentines form via the hydration of peridotites and are characterized by textures that are strictly indicative of retrograde replacement of olivine, orthopyroxene, and clinopyroxene. Antigorite serpentine forms largely by the recrystallization of pseudomorphic serpentines during prograde metamorphism (Coleman, 1971; Wicks and Whittaker, 1977; Dungan, 1979). There are, naturally, exceptions to this rule. Retrograde lizardite serpentinization is generally inferred to occur in the low-temperature 50-300 °C range whereas retrograde antigorite serpentinization occurs in the high temperature 400-600 °C range (Evans, 2010). The former scenario is the most common by far. In general terms, antigorite is the high temperature serpentine mineral whereas lizardite and chrysotile are the low temperature minerals (e.g. O'Hanley et al., 1989).

From the observed assemblages, it is interpreted that the New Caledonian peridotite was first serpentinized in a low-temperature regime by altering the olivine and orthopyroxene into lizardite and minor chlorite (Reynard et al., 2015). Lending credence to this scenario is the presence of magnetite, which is detected in hand samples 3 and 10. Magnetite originates from low-temperature serpentinization as a reaction product along with dihydrogen gas and brucite (Equation 1); these products are the result of slow Mg-Fe olivine diffusion rates.

$$\text{MgFe Olivine} + H_2O = \text{MgFe Serpentine} + \text{Brucite} + \text{Magnetite} + H_2\,(\text{aq}) \qquad (1)$$

At temperatures consistent with antigorite serpentinization, Mg-Fe diffusion rates in olivine are orders of magnitude faster, with the result that the growth of Mg-rich antigorite can be accommodated by a compositional adjustment of olivine, eliminating the need to precipitate magnetite (Evans, 2010; Schwartz et al., 2013). Also supporting this regime are the sulfur and chlorine present in the lizardite-bearing samples, which originate early near mid-ocean ridges from circulating seawater during serpentinization (Debret et al., 2013). The brucite component of Equation 1 may be related to the observed 4.5 to 5.0 Å phase in the TEM analysis of samples 3 and 4, brucite having a basal spacing of ~ 4.5 Å; further investigation of these areas will be needed to confirm this identification.

The lizardite-bearing samples are Mg-rich and Al-poor, therefore phase stability is likely closely analogous to the MgO-SiO_2-H_2O (MSH) system (the most common retrograde regime) rather than the MgO-Al_2O_3-SiO_2-H_2O system, where lizardite stability increases drastically into antigorite stability zones; the lack of any antigorite-lizardite coexistence among the samples supports this assertion (O'Hanley et al., 1989; Evans, 2004). Recent pressure-temperature diagrams based on oxygen isotope thermometry show a stable field of chrysotile between 195°C

and 260°C with lizardite stable below and antigorite stable above (O'Hanley and Wicks, 1995; O'Hanley, 1996). These relationships are confirmed with stable isotope data from lizardite serpentinites that suggest formation at a temperature less than 200 °C (Wenner and Taylor (1971).

Lizardite is interpreted as the primary serpentinization product. Bastites are lizardite formed from pyroxene rather than from olivine and are usually replaced by talc or talc + antigorite. In his study of the Darrington peridotites, Dungan (1979) noted that most of the bastites converted to aggregates of talc + chlorite or talc + antigorite; he also found that antigorite growth is facilitated by the presence of chrysotile in mesh-textured serpentine (serpentine formed from olivine) but that chrysotile is absent in bastites. Any relationships inferred from this information are impeded by lack of detailed petrography of the New Caledonia serpentinites. Having both bastites and mesh-textured serpentines would go far to explain the relationships between samples bearing both high amounts of chrysotile and antigorite (samples 8 and 9) and the samples containing both antigorite and talc (samples 3 and 10); however, the nature of these rocks are primarily harzbugitic, so a bimodal primary phase of olivine plus orthopyroxene is the case. Conversely, the fact that chrysotile and antigorite do occur together suggests that antigorite preceded chrysotile as the nanofibers of chrysotile would have otherwise shown signs of alteration.

Chrysotile is by far the most common phase among the samples, occurring in all but three (1, 2, and 3). Chrysotile is a component of New Caledonian 'garnierite' that is often downplayed in favor of lizardite; however, from the results, it is quite clear that it is a common constituent. It may be possible that due to the fine-grained nature, complex interstratification of phases, and the

presence of multiple serpentine polymorphs that identification of chrysotile with XRD alone was impeded in past investigations.

Chrysotile growth, forming metastably from lizardite, is favored in isotropic stress micro-environments of fluid-filled voids and pores and in veins, generally after active hydration in the immediate surroundings has ceased (O'Hanley et al., 1989; Evans, 2004). Indeed, Pritchard (1979), Laurent and Hebert (1979), and Cogulu and Laurent (1984) concluded from studies of ophiolites and from ocean floor lithologies that chrysotile did not form until olivine had reacted out the system. Due to having different stability fields, the widespread coexistence of lizardite and chrysotile in natural systems is rationalized by assuming that they formed from separate solid solutions; the addition of variable amounts of iron as well as aluminum virtually ensures that both phases will coexist stably. The occurrence of the chrysotile crystallizing in discrete veins and voids in the sample material supports the environment favorable to have lizardite and chrysotile occurring adjacent to one another because both the preferred growth kinetics of chrysotile and the necessity for two separate solid solutions are satisfied. Samples 4, 6, and 7 (and 5 to a minor degree) have lizardite and chrysotile coexisting; these samples likely represent a formation stage in which lizardite is being altered to chrysotile.

Manceau et al. (1985) reported the presence of antigorite as a minor phase along with chrysotile in lizardite-nepouite series samples from New Caledonia, providing a 3 μm electron micrograph of platy-tabular crystals in association with silica gels. Theirs is the only report of antigorite in New Caledonia and it was clearly assessed as a minor phase of little importance. In contrast, the observations in this study show antigorite in equally abundant amounts as lizardite and chrysotile in several samples. Although limited in the number of samples, TEM data from

samples 3, 8, 9, and 10 clearly show that antigorite is present (Figs. 3.19, 3.37, 3.45, and 3.49). There are two scenarios that might have produced it: (1) it is the primary serpentinization phase and (2) it is the product of prograde recrystallization of primary serpentines. As stated previously, the antigorite bearing samples contain significant amounts of magnetite, its presence detected by characteristic high specific gravity, metallic luster, and a clear reaction with a magnet. Magnetite occurring with antigorite must be residual from primary lizardite serpentinization (Evans, 2010); the antigorite crystalized after lizardite and magnetite. Lending support to this scenario is a possible phase transformation between lizardite and antigorite captured in Figure 3.23b.

The lack of significant antigorite-lizardite coexistence among the samples material may indicate that either antigorite formation occurred after serpentinization had long ceased and all lizardite had converted to chrysotile in a post-obduction prograde metamorphic event or that antigorite is the product of recrystallization of lizardite during a syn- or post-emplacement heat input. Nicholson (2016, personal communication) asserts that the ophiolite nappe in New Caledonia underwent conditions much higher than supergene (50 °C or less) as is generally accepted (LaGabrielle et al., 2013), but involved temperatures in the range of 700 °C, which is sufficient for the usually sluggish crystallization of antigorite to commence and form the crystals observed with TEM. As the vertical distribution of antigorite was not assessed in this investigation, the nature and timing of the thermal event cannot be determined at present. The position of antigorite in a vertical section would be able to delineate this information; if it is present only at the interface with the underlying terrane, the emplacement itself could have been a high temperature event, in disagreement with the widely accepted passive emplacement model (LaGabrielle et al. 2013) and if antigorite is distributed throughout the vertical section, post-

emplacement extensional faulting, which is associated with the ophiolite units, may have contributed the required conditions. The recognition of antigorite in several samples indicates that the pressure-temperature regime in New Caledonia should be revisited and this finding justifies detailed exploration for antigorite to reconstruct P-T regimes.

The proposed formation history of the phyllosilicates in New Caledonian Ni-laterites based on sample assemblages is hypothesized to consist of three distinct generations of mineralization. (1) The parent rock, of dunite-harzburgite composition, was hydrated into a serpentinite consisting of lizardite with minor chlorite (both with good crystallographic order consistent with the morphologies observed with TEM) and magnetite while it was still submerged in the ocean. With this alteration, nickel moved sluggishly into the primary alteration phases from the peridotite in low concentrations as evidenced by the lower concentrations in the lizardite-bearing samples; (2) The primary serpentinite was then obducted onto the continental crust, the heat and pressure from this event or other post-obduction tectonic events such as extensional faulting causing some of the lizardite to experience prograde metamorphism into antigorite and talc-willemseite, with primary alteration chlorite and magnetite persisting; (3) Post obduction, the laterization process began (either after or contemporaneous with antigorite formation), aided by the post-obduction extension of the ultramafic nappe, allowing silica rich fluids containing trace amounts of silver and gold to produce a second generation of phyllosilicates with a significant nickel enrichment. Primary lizardite and chlorite were altered to chrysotile, a second generation of Ni-enriched lizardite-nepouite series minerals, kerolite-pimelite series minerals, and secondary disordered chlorite.

4.6 Implications for New Caledonia: Mining and Health

The present investigation has revealed that nickel phyllosilicates in New Caledonia are associated with significant amounts of silver nanoparticles (Ag-NPs), an economically valuable component. The spatial distribution and concentrations of the Ag-NPs still need to be evaluated; however, the exploration and exploitation of Ag-NPs may prove to be a worthwhile investment for New Caledonia. Better still, since silver is inert, it could potentially be recovered from mining slag.

On the other hand the presence of Ag-NPs is of major environmental and health concern. Ag-NPs have been found to be highly toxic to many organisms including aquatic and terrestrial plants, algae, fungi, and aquatic vertebrates, invertebrates, and microorganisms (Levard et al. 2012). Silver accumulates in the gills and gut of freshwater and marine fish as well as in freshwater crustaceans and impairs ionoregulatory function (Bianchini et al., 2005; Blinova et al., 2012; Levard et al. 2012). Even in low concentrations, Ag-NPs were found to be toxic to algae and crustaceans (Kahru and Dubourguier, 2010).

Ag-NPs also pose a risk to humans; they are one of many nanomaterials (including fullerenes, carbon nanotubes, and titanium dioxide) that affect mitochondrial function, leading to programmed cell death (apoptosis) (Elsaesser and Howard, 2012; Oberdorster, 2005). Ag-NPs are well known to be toxic to skin keratinocytes, lung fibroblast cells, and glioblastoma cells in humans (Levard et al., 2012). In addition, Ag-NPs readily transform in the environment with interaction with air, water, and soil, which modifies their surface properties and alters their transport, fate, and toxicity (Levard et al., 2012; Elsaesser and Howard, 2012).

Another nanoparticle found ubiquitously throughout of the sample material (occurring in 7 out of 10 samples) with well-known toxicity is chrysotile asbestos. The fiber lengths vary 50 to

700 nm among the sample material, well below the 2.5 μm requirement for inhalation into the deep lung. The size of the particles to which individuals are exposed is important; ultrafine particles remain in the lung long after fine particles have already dissolved (Oberdorster et al., 2005). This is due to an increased surface area in ultrafine particles that allows them to be more reactive. As earth materials enter the body, they can change redox state, causing them to be more or less soluble. The change in solubility then affects permeability and persistence in the body.

The human body has great difficulty removing nano-sized particles from the respiratory tract. This process is typically done in the form of macrophages, the effectiveness of which is limited by the macrophage's ability to detect particles, locate them, and perform phagocytosis (Oberdorster, 2005). Ultrafine particles are often able to avoid these macrophages, due to their ability to use endocytosis, competitively inhibiting calcium in neural synapses, to translocate throughout the body (e.g. liver, spleen, heart, kidney, and bone marrow), which is the same mechanisms that viruses use to spread cell to cell (Elsaesser and Howard, 2012).

One of the major issues associated with the uptake of these particles is the difficulty the body encounters in eliminating them from the body. Because these particles stay in the body for an extended period of time, their effects can last long after they are inhaled. Lung tissue tends to hold onto these particles far more effectively than do other body tissues or fluids such as urine, blood or nails. Miners and factory workers who are exposed to high amounts of mineral dust over an extended period of time frequently develop serious illnesses such as lung cancer and pneumoconiosis, however, the main public health concerns with all nanomaterials is with chronic, low dose exposure over a lifetime, possibly leading to increased incidences of degenerative diseases (Elsaesser and Howard, 2012).

Poor management of tailings in nickel-mines in New Caledonia has likely caused these mineral fibers to become airborne and potentially contribute to the observed high incidences of malignant mesothelioma among island residents and most intensely in the mine-workers. The field of nanotoxicology is still in its infancy and it is clear that further investigation of Ag-nanoparticles and the asbestos in New Caledonia is needed to assess the environmental and health damage.

4.7 Further Investigations

In order to delineate the petrologic evolution of the laterized ophiolite complexes in New Caledonia conclusively, cores should be taken at different points throughout the island rather than the random sample collection investigated here. Although these samples were informative and some inferences can be made, samples with context will lend more credence to the conclusions. The proposed cores should be examined at multiple scales and at small intervals as it is clear that the evolution of the assemblages is complex. Detailed petrography should be done to examine the large-scale mineralogical textures at each interval; powder X-ray diffraction should be done to see how crystallographic order of the phases evolves over time; SEM should be done to add more detail to petrographic data; TEM should be done to (1) observe how the crystallographic order of the phases evolves spatially; (2) observe if phases are present that were undetected using XRD (3) examine how the phases transform over time; (4) to monitor the movement of key elements as phases transform spatially using elemental concentration mapping; electron microprobe analysis (EMPA) should be done at intervals to observe how the composition changes in relation to phases.

TEM analysis of these materials is difficult due to the high water content. Multiple preparation techniques should be applied to samples. Ion milling must be done with care as the phases are very sensitive to heat. Several grain mounts of the silver-bearing material must be prepared and analyzed in great detail and compared to ion-milled mounts in order to determine if the silver is located only within the silica phase.

5. CONCLUSIONS

'Garnierite' is often referred to as an intimate mixture of serpentine and talc-like phases; however, this statement may need to be revaluated for considerations of scale. Although XRD results in this and past studies have shown that serpentine and talc-like phases appear to be intimately mixed, TEM has revealed otherwise. The extremely fine-grained 'garnierite' does not contain talc and serpentine interstratified at the nanoscale but rather in discrete packages, likely having formed in separate events due to the significant variation in textures.

The material referred to as 'talc-like' is actually two distinct structural phases, both with approximately 10 Å basal spacing. The kerolite-pimelite series minerals, which comprise the majority of the talc-like phases observed in the sample material, occur as small, pseudo-lamellar platy crystals that display significant crystallographic disorder and are highly sensitive to radiation damage from the electron beam, related to their higher water content. The talc-willemseite series, however, were observed to have larger crystals with well-ordered lattices and a higher resistance to beam damage. These two talc-like minerals have very different formation styles; the kerolite-pimelite minerals are interpreted to have crystallized from a gel-like state facilitated by low-temperature weathering, causing the extreme turbostratic stacking disorder observed, whereas the talc-willemseite phases likely formed via hydrothermal alteration or low-grade metamorphism. The presence of both of these phases suggests that two different events occurred to produce them.

In past investigations of New Caledonian Ni-phyllosilicates, only lizardite and chrysotile were observed to comprise the serpentine component. However, in the samples investigated here, lizardite, chrysotile, and antigorite, were observed in approximately equal measure with TEM.

Lizardite occurs as platy crystals with well-pronounced, continuous lattices with a significant amount of lenticular lattice partings, which result from cation diffusion related to the alteration process (Ahn et al. 1986; Pecor, 1992). From these textures as well as associated phases, lizardite is interpreted to be the primary serpentinization product along with chlorite.

Chrysotile occurred in 7 out of 10 samples as nanofibers varying 50 to 700 nm in length. The nanofiber size is important and of great concern as the size range observed is well below the 2.5 micrometers or less required for particles to be inhaled into the deep lung. These particles may be significantly contributing to the high incidences of lung disease such as lung cancer and malignant mesothelioma in New Caledonia among mine works and the general public. Indeed, medical investigations of lung disease in New Caledonia have identified chrysotile asbestos as an important co-factor although the geological community has not investigated the amount, size, and distribution of the chrysotile. The size of the nanofibers made identification in hand sample all but impossible, and the distribution of it among the samples as observed with TEM is such that it is likely a larger component of the Ni-laterite deposits than previously considered.

Antigorite occurs as platy crystals with superlattice periodicities that vary 20 to 60 Å in width. The presence of antigorite among the sample material is significant because a high temperature alteration event (around approximately 700 °C) would have been required to facilitate the normally sluggish growth kinetics of the modulated crystal structure. Candidate thermal events for the formation of antigorite in this setting are (1) the emplacement of the ophiolite itself and (2) post-obduction extensional faulting; however, these hypotheses are in disagreement currently accepted tectonic models for the New Caledonian ophiolite, which is considered to have been passive and supergene.

Chlorite, which has been reported before in New Caledonia, is observed here to possess two distinct morphologies both with approximately 14 Å basal spacing: those with continuous, well-ordered lattices and those with turbostratically disordered lattices similar to the kerolite-pimelite series minerals. The implications of this are that two generations of chlorite may be present, one that is primary and associated with pre-obduction serpentinization and one that is secondary and associated with tropical weathering of the ultramafic rocks.

A newly discovered component of the nickel-phyllosilicates are the silver nanoparticles present in significant amounts in two of the samples selected for study, displaying complex, nanoporphyroblastic textures, describing their bimodal size distribution of 2 to 30 nm and 150 to 650 nm, consistent with Ostwald ripening phenomena. The Ag-nanoparticles likely have not been reported before due to their size and potentially small weight percentage, which would not have been detected with XRD; additional examination of the material will help to delineate the amount of Ag-nanoparticles present and the extent to which they associate with the nickel phyllosilicates. These Ag-nanoparticles are a potential economically valuable product for New Caledonia; however, they are also a cause for concern. Silver nanoparticles are known to be highly toxic to a variety of aquatic and terrestrial flora and fauna and even humans.

Nickel mining is vital to the economy of New Caledonia. In order to fully exploit the laterite deposits in a way that is both lucrative and safe for the workers, citizens, wildlife, and environment, a complete characterization and understanding of the target material is important. TEM is very useful in elucidating the nanoscale features of extremely fine-grained and intermixed material such as these Ni-phyllosilicates, which may not have been detectable otherwise.

REFERENCES

Ahn, J.H., Pecor, D.R., and Essene, E.J. (1986) Cation-diffusion-induced characteristic beam damage in transmission electron microscope images of micas. Ultramicroscopy, 19, 375-382.

Ali, S.H. and Grewal, A.H. (2006) The ecology and economy of indigenous resistance: divergent perspectives on mining in New Caledonia. The Contemporary Pacific, 18, 361-392.

Ambatsian, P., Fernex, F., Bernat, M., Parron, C., Lecolle, J. (1997) High metal inputs to closed seas: the New Caledonian lagoon. Journal of Geochemical Exploration, 59, 59-74.

Bailey, S.W. (1969) Polytypism of trioctahedral 1:1 layer silicates. Clays and Clay Minerals, 17, 355-371.

Bailey, S.W. (1988) X-ray diffraction identification of the polytypes of mica, serpentine, and chlorite. Clays and Clay Minerals, 36, 3, 193-213.

Bailey, S.W., and Banfield, J.F. (1995) Derivation and identification of nonstandard serpentine polytypes. American Mineralogist, 80, 1104-1115.

Banfield, J.F., and Bailey, S.W. (1996) Formation of regularly interstratified serpentine-chlorite minerals by tetrahedral inversion in long-period serpentine polytypes. American Mineralogist, 81, 79-91.

Baronnet, A. (1992) Polysomatism and stacking disorder. Reviews in Mineralogy and Geochemistry, 27, 181-230.

Barannet, A., and Devouard, B. (2005) Microstructures of common polygonal serpentines from axial HRTEM imaging, electron diffractions, and lattice simulation data. The Canadian Mineralogist, 43, 513-542.

Baronnet, A., Mellini, M., and Devouard, B. (1994) Sectors in polygonal serpentine. A model based on dislocations. Physics and Chemistry of Minerals, 21, 330-343.

Baumann, F., Maurizot, P., Mangeas, M., Ambrosi, J., Douwes, J., and Robineau, B. (2011) Pleural mesothelioma in New Caledonia: associations with environmental risk factors. Environmental Health Perspectives, 119, 695-700.

Bentabol, M., Cruz, M.D.R., and Huertas, F.J. (2007) Synthesis of Ni-rich 1:1 phyllosilicates. Clays and Clay Minerals, 55, 572-582.

Bianchini, A., Playle, R.C., Wood, C.M., and Walsh, P.J. (2005) Mechanism of acute silver toxicity in marine invertebrates. Aquatic Toxicology, 72, 67-82.

Bird, E.C.F., Dubois, J., Iltis, J. (1984) The impacts of opencast mining on the rivers and coasts of New Caledonia. Tokyo: United Nations University, 60.

Blinova, I., Niskanen, J., Kajankari, P., Kanarbik, L., Käkinen, A., Tenhu, H., Penttinen, O-P., and Kahru, A. (2013) Toxicity of two types of silver nanopartilces to aquatic crustaceans *Daphnia magna* and *Thamnocephalus platyurus*. Environmental Science and Pollution Research, 20, 3456-3463.

Bloise, A., Belluso, E., Fornero, E., Rinaudo, C., Barrese, E., and Capella, S. (2010) Influence of synthesis conditions on growth of Ni-doped chrysotile. Microporous and Mesoporous Materials, 132, 239-245.

Brindley, G.W., and Hang, P.T. (1973) The nature of garnierites – I structures, chemical compositions and color characteristics. Clays and Clay Minerals, 21, 27-40.

Brindley, G.W., and Maksimovic, Z. (1974) The nature and nomenclature of hydrous nickel-containing silicates. Clay Minerals, 10, 271-277.

Brindley, G.W., and de Souza Santos, P. (1971) Antigorite – its occurrence as a clay mineral. Clays and Clay Minerals, 19, 187-191.

Brindley, G.W., and Wan, H. (1975) Compositions, structures, and thermal behavior of nickel-containing minerals in the lizardite-nepouite series. American Mineralogist, 60, 863-871.

Brindley, G.W., Bish, D.L., and Wan, H. (1977) The nature of kerolite, it's relation to talc and stevensite. Mineralogical Magazine, 41, 443-452.

Brindley, G.W., Bish, D.L., and Wan, H. (1979) Compositions, structures, and properties of nickel-containing minerals in the kerolite-pimelite series. American Mineralogist, 64, 615-625.

Burke, M. (2013) Transmission electron microscopy (TEM) and bulk chemical investigations of copper and associated silver from Michigan's Keweenaw peninsula: Implications for formation and archaeological interpretations. Geological Society of America Abstracts with Programs, 45, 178.

Burke, M. (2015) An electron microscopy study of gold and associated minerals from Round Mountain, Nevada. M.Sc. Thesis, Miami University, Oxford, OH.

Bustamante, P., Grigioni, S., Boucher-Rodoni, R., Caurant, F., and Miramand, P. (2000) Bioaccumulation of 12 trace elements in the tissues of the nautilus *Nautilus macromphalus* from New Caledonia. Marine Pollution Bulletin, 40, 688-696.

Cluzel, D. and Vigier, B. (2008) Syntectonic mobility of supergene nickel ores of New Caledonia (Southwest Pacific): evidence from garnierite veins and faulted regolith. Resource Geology, 58, 161-170.

Cluzel, D., Aitchison, J.C., and Picard, C. (2001) Tectonic accretion and underplating of mafic terranes in the Late Eocene intraoceanic fore-arc of New Caledonia (Southwest Pacific): geodynamic implications, Tectonophysics, 340, 23-59.

Cunningham, S.D., and Berti, W.R. (1993) Remediation of contaminated soils with green plants: an overview. In Vitro Cellular and Developmental Biology-Plant, 29, 207-212.

Danloux, J., and Laganier, R. (1991) Classification et quantification des phénomènes d'érosion, de transport et de sédimentation sur les bassins touchés par l'exploitation minière en Nouvelle Calédonie, ORSTOM, Nouméa (in French).

Debret, B., Koga, K.T., Nicollet, C., Andreani, M., and Schwartz, S. (2014) F, Cl, and S input via serpentinite in subduction zones: implications for the nature of the fluid released at depth. Terra Nova, 26, 96-101.

Dlugogorski, B.Z. and Balucan, R.D. (2014) Dehydroxylation of serpentine minerals: Implications for mineral carbonation. Renewable and Sustainable Energy Reviews, 31, 353-367.

Dódony, I. and Buseck, P.R. (2004) Lizardite-chlorite structural relationships and inferred high-pressure lizardite polytype. American Mineralogist, 89, 1631-1639.

Dódony, I., Pósfai, M., and Buseck, P.R. (2002) Revised structure models for antigorite: an HRTEM study. American Mineralogist, 87, 1443-1457.

Dublet, G., Juillot, F., Morin, G., Fritsch, E., Fandeur, D., Ona-Nguema, G., and Brown, G.E. Jr. (2012) Ni speciation in a New Caledonian lateritic regolith: a quantitative X-ray absorption spectroscopy investigation. Geochimica et Cosmochimica Acta, 95, 119-133.

Dupon, J.F. (1986) Les effets de l'exploitation minière sur l'environnement des îles hautes: le cas de l'extraction du minerai de nickel en Nouvelle-Calédonie (in French).

Dungan, M.A. (1979) A microprobe study of antigorite and some serpentine pseudomorphs. Canadian Mineralogist, 17, 771-784.

Elsaesser, A. and Howard, C.V. (2012) Toxicology of nanoparticles. Advanced Drug Delivery Reviews, 64, 129-137.

Evans, B.W. (2004) The serpentine multisystem revisited: Chrysotile is metastable. International Geology Reviews, 46, 479-506.

Evans, B.W. (2010) Lizardite versus antigorite serpentinite: Magnetite, hydrogen, and life (?). Geology, 38, 879-882.

Faust, G.T. (1966) The hydrous nickel-magnesium silicates – the garnierite group. American Mineralogist, 51, 271-298.

Fernandez, J., Ouillon,S., Chevillon, C., Douillet, P., Fichez, R., Le Gendre, R. (2006) A combined modelling and geochemical study of the fate of terrigenous inputs from mixed natural and mining sources in a coral reef lagoon (New Caledonia). Marine Pollution Bulletin, 52, 320-331.

Fitzherbert, J.A., Clarke, G.L., and Powell, R. (2003) Lawsonite-Omphacite-bearing metabasites of the Pam Peninsula, NE New Caledonia: Evidence for disrupted blueschist- to ecolgite-facies conditions. Journal of Petrology, 44, 1805-1831.

Fleischer, M. (1969) New mineral names. The American Mineralogist, 54, 1737-1742.

Florence, T.M., Stauber, J.L., Ahsanullah, M. (1994) Toxicity of nickel ores to marine organisms. Science of the Total Environment, 148, 139-155.

Gualtieri, A.F., Giacobbe, C., and Viti, C. (2012) The dehydroxylation of serpentine group minerals. American Mineralogist, 97, 666-680.

Hang, P.T., and Brindley, G.W. (1973) The nature of garnierites – III thermal transformations. Clays and Clay Minerals, 21, 51-57.

Hédouin, L., Pringault, O., Metian, M., Bustamante, P., Warnau, M. (2007) Nickel bioaccumulation in bivalves from the New Caledonia lagoon: seawater and food exposure. Chemosphere, 66, 1449-1457.

Horowitz, L.S. (2009) Environmental violence and crises of legitimacy in New Caledonia. Political Geography, 28, 248-258.

Jaffré T., Latham, M., and Schmid, M. (1977) Aspects de l'influence de l'extraction du minerai de nickel sur la vegetation et les sols en Nouvelle-Calédonie. Cah ORSTOM Sér Biol, 12, 307-231 (in French)

Jaffré, T., Munzinger, J., and Lowry, P.P. II. (2010) Threats to the conifer species found on New Caledonia's ultramafic massifs and proposals for urgently needed measures to improve their protection. Biodiversity and Conservation, 19, 1485-1502.

Kahru, A. and Dubourguier, H.C. (2010) From ecotoxicology to nanoecotoxicology. Toxicology, 269, 105-119.

Kato, T. (1961) A study on the so-called garnierite from New Caledonia. Mineralogical Journal, 3, 107-121.

Kendrick, M.A., Honda, M., Pettke, T., Scambelluri, M., Phillips, D., and Giuliani, A. (2013) Subduction zone fluxes of halogens and noble gases in seafloor and forearc serpentinites. Earth and Planetary Science Letters, 365, 86-96.

Kim, J., Pecor, D.R., Tessier, D., and Elass, F. (1995) A technique for maintaining texture and permanent explansion of smectite interlayers for TEM observations. Clays and Clay Minerals, 43, 51-57.

Kogure, T., Kameda, J., Matsui, T., and Miyawaki, R. (2006) Stacking structure in disordered talc: interpretation of its X-ray diffraction pattern by using pattern simulation and high-resolution transmission electron microscopy. American Mineralogist, 91, 1363-1370.

Krekeler, M.P.S., and Guggenheim, S. (2008) Defects in microstructure in palygorskite-sepiolite minerals: a transmission electron microscopy (TEM) study. Applied Clay Science, 39, 98-105.

Krekeler, M.P.S., Guggenheim, S., and Rakovan, J. (2004) A microtexture study of palygorskite-rich sediments from the Hawthorne Formation, Southern Georgia, by transmission electron microscopy and atomic force microscopy. Clays and Clay Minerals, 52, 263-274.

Kretz, R. (1983) Symbols for rock-forming minerals. American Mineralogist, 68, 277-279.

LaGabrielle, Y., Chauvet, A., Ulrich, M., and Guillot, S. (2013) Passive obduction and gravity-driven emplacement of large ophiolite sheets: The New Caledonian ophiolite (SW Pacific) as a case study? Bulletin de la Société Géologique de France, 184, 373-384.

Langer, A.M., Rohl, A.N., Selikoff, I.J., Harlow, G.E., and Prinz, M. (1980) Asbestos as a cofactor in carcinogenesis among nickel-processing workers. Science, 209, 4454, 420-422.

Latham, M. (1971) L'influence de l'exploitation minière sur la dégradation des sols en Nouvelle-Calédonie (in French).

Levard, C., Hotze, E.M., Lowry, G.V., and Brown, G.E. Jr. (2012) Environmental transformations of silver nanoparticles: Impact on stability and toxicity. Environmental Science and Technology, 46, 6900-6914.

L'Huillier, L., Jaffré, T., Wulff, A., Lebrun, M., Maggia, L., Barré, N., and Gateblé, G. (2010) Mines et Environnement en Nouvelle-Calédonie.

Lillie, A.R., and Brothers, R.N. (1970) The geology of New Caledonia. New Zealand Journal of Geology and Geophysics, 13, 145-183.

Losfield, G., L'Hullier, L., Fogliani, B., Jaffre, T., and Grison, C. (2015) Mining in New Caledonia: environmental stakes and restoration opportunities. Environmental Science and Pollution Research, 22, 5592-5607.

Luce, D., Bugel, I., Goldberg, P., Goldberg, M., Salomon, C., Billion-Ballard, M., Nicolau, J., Quénel, P., Fevotte, J., and Brochard, P. (2000) Environmental exposure to tremolite and respiratory cancer in New Caledonia: a case-control study. American Journal of Epidemiology, 151, 259-265.

Manceau, A., and Calas, G. (1985) Heterogeneous distribution of nickel in hydrous silicates from New Caledonia ore deposits. American Mineralogist, 70, 549-558.

Manceau, A., Calas, G., and Decarreau, A. (1985) Nickel-bearing clay minerals: I. Optical spectroscopy study of nickel crystal chemistry. Clay Minerals, 20, 367-387.

McDonald, A., Scott, B., and Villemure, G. (2009) Hydrothermal preparation of nanotubular particles of a 1:1 nickel phyllosilicate. Microporous and Mesoporous Materials, 120, 263-266.

McKelvy, M.J., Chizmeshya, A.V., Diefenbacher, J., Béarat, H., and Wolf, G. (2004) Exploration of the role of heat activation in enhancing serpentine carbon sequestration reactions. Environmental Science and Technology, 38, 6897-6903.

Mellini, M. and Zanazzi, P.F. (1987) Crystal structures of lizardite-1*T* and lizardite-2*H*1 from Coli, Italy. American Mineralogist, 72, 943-948.

Migon, M., Ouillon, S., Mari, X., Nicolas,E. (2007) Geochemical and hydrodynamic constraints on the distribution of trace metal concentrations in the lagoon of Nouméa, New Caledonia. Estuarine, Coastal and Shelf Science, 74, 756-765.

Montoya, J.W. and Baur, G.S. (1963) Nickeliferous serpentines, chlorites, and related minerals found in two lateritic ores. The American Mineralogist, 48, 1227-1238.

Moore, D.M. and Reynolds, R.C. (1989) X-ray Diffraction and the Identification and Analysis of Clay Minerals. Oxford University Press.

Mudd, G.M. (2010) Global trends and environmental issues in nickel mining: sulfides versus laterites. Ore Geology Reviews, 38, 9-26.

Novgorodova, M.I., Gorshkov, A.I., and Mokhov, A.V. (1981) Native silver and its new structural modifications. International Geology Review, 23, 485-494.

Oberdörster, G., Oberdörster, E., and Oberdörster, J. (2005) Nanotoxicology: an emerging discipline evolving from studies of ultrafine particles. Environmental Health Perspectives, 823-839.

O'Hanley, D.S. (1996) Serpentinites: Records of petrologic and tectonic history. Oxford Monographs in Geology and Geophysics, 34.

O'Hanley, D.S. and Wicks, F.J. (1995) Conditions of formation of lizardite, chrysotile, and antigorite, Cassiar, British Columbia. The Canadian Mineralogist, 33, 753-773.

O'Hanley, D.S., Chernosky, J.V. Jr., and Wicks, F.J. (1989) The stability of lizardite and chrysotile. Canadian Mineralogist, 27, 483-493.

Pascal, M., De Forges, B.R., Le Guyader, H., and Simberloff, D. (2008) Mining and other threats to the New Caledonia biodiversity hotspot. Conservation Biology, 22, 498-499.

Pecora, W.T., Hobbs, S.W., and Murata, K.J. (1949) Variations in garnierite from the nickel deposit near Riddle, Oregon. Economic Geology, 44, 13-23.

Pelletier, B. (1983) Localisation du nickel dans les minerais "garnieritiques" de Nouvelle-Caledonie. Sci. Géol., Mém, 73, 173-183.

Pérez-Rodríguez, J.L., Franco, F., Ramírez-Valle, V., and Pérez-Maqueda, L.A. (2005) Modification of the thermal dehydroxylation of antigorite by ultrasound treatment. Journal of Thermal Analysis and Calorimetry, 82, 769-774.

Rayner, J.H. and Brown, G. (1973) The crystal structure of talc. Clays and Clay Minerals, 21.

Reynard, B., Bezacier, L., and Caracas, R. (2015) Serpentines, talcs, chlorites, and their high-pressure phase transitions: a Raman spectroscopy study. Physics and Chemistry of Minerals, 42, 641-649.

Saunders, J.A. (1990) Colloidal transport of gold and silica in epithermal precious-metal deposits: evidence from the Sleeper deposit, Nevada. Geology, 18, 757-760.

Saunders, J.A. (1994) Silica and gold textures in bonanza ores of the Sleeper deposits, Humboldt County, Nevada: evidence for colloids and implications for epithermal ore-forming processes. Economic Geology, 89, 628-638.

Saunders, J.A. (2012) Textural evidence of episodic introduction of metallic nanoparticles into bonanza epithermal ores. Minerals, 2, 228-243.

Schmidt, C. (1884) Annalen der Physik

Schwartz, S., Guillot, S., Reynard, B., Lafay, R., Debret, B., Lanari, P., and Auzende, A.L. (2013) Pressure-temperature estimates of the lizardite/antigorite transition in high pressure serpentinites. Lithos, 178, 197-210.

Soler, J.M., Cama, J., Gali, S., Meléndez, W., Ramírez, A., and Estanga, J. (2008) Composition and dissolution kinetics of garnierite from the Loma de Hierro Ni-laterite deposit, Venezuela. Chemical Geology, 249, 191-202.

Spangenberg, K. (1938) Die wasserhaltigen nickelsilicate. Centennial Mineralogy, Abstract A, 360-364.

Springer, G. (1976) Falcondoite, nickel analogue of sepiolite. Canadian Mineralogist, 14, 407-409.

Suarez, S., Nieto, F., Velasco, F., and Martin, F.J. (2011) Serpentine and chlorite as effective Ni-Cu sinks during weathering of the Aguablanca sulphide deposit (SW Spain). TEM evidence for metal-retention mechanisms in sheet silicates. European Journal of Mineralogy, 23, 179-196.

Trittschack, R., Grobéty, B., and Koch-Müller, M. (2012) In situ high-temperature Raman and FTIR spectroscopy of the phase transformation of lizardite. American Mineralogist, 97, 1956-1976.

Uehara, S. (1998) TEM and XRD study of antigorite superstructures. The Canadian Mineralogist, 36, 1595-1605.

UNESCO (2013) Lagoons of New Caledonia: reef diversity and associated ecosystems.

US Geological Survey (2010) Mineral commodity summary 2010. US Geological Survey, 108-109.

Uyeda, N., Hang, P.T., and Brindley, G.W. (1973) The nature of garnierites – II electron-optical study. Clays and Clay Minerals, 21, 41-50.

Veblen, D.R. (1992) Electron microscopy applied to nonstoichiometry, polysomatism, and replacement reactions in minerals. Reviews in Mineralogy and Geochemistry, 27, 181-230.

Villanova-de-Benavent, C., Nieto, F., Proenza, J.A., and Galí, S. (2011) Talc- and serpentine-like "garnierites" from Falcondo Ni-laterite deposit (Dominican Republic): a HRTEM approach. Macala, 15, 197-198.

Villanova-de-Benavent, C., Viti, C., Proenza, J.A., Galí, S., and Nieto, F. (2015) Ni-enrichment processes revealed by TEM imaging on garnierites. Macla, 20, 149-150.

Viti, C. (2010) Serpentine minerals discrimination by thermal analysis. American Mineralogist, 95, 631-638.

Voorhees, P.W. (1984) The theory of Ostwald ripening. Journal of Statistical Physics, 38, 231-253.

de Waal, S.A. (1970) Nickel minerals from Barberton, South Africa: II. Nimite, a nickel-rich chlorite. The American Mineralogist, 55, 18-30.

Warren, B.E. (1941) X-ray diffraction in random layer lattices. The Physical Review, 59, 693-698.

Wells, M.A., Ramanaidou, E.R., Verrall, M., and Tessarolo, C. (2009) Mineralogy and crystal chemistry of "garnierites" in the Goro lateritic nickel deposit, New Caledonia. European Journal of Mineralogy, 21, 467-483.

Whittaker, E.J.W. and Zussman, J. (1956) The characterization of serpentine minerals by X-ray diffraction. Mineralogical Magazine, 31, 107-126.

Wicks, F.J. and O'Hanley, D.S. (1988) Serpentine minerals; structures and petrology. Reviews in Mineralogy and Geochemistry, 19, 91-167.

Wicks, F.J. and Whittaker, E.J.W. (1975) A reappraisal of the structures of the serpentine minerals. The Canadian Mineralogist, 13, 227-243.

Wulff, A.S., Hollingsworth, P.M., Ahrends, A., Jaffré, T., Vellion, J., L'Huillier, L., and Fogliani, B. (2013) Conservation priorities in a biodiversity hotspot: analysis of narrow endemic plant species in New Caledonia. PLoS ONE, 8, 1-14.

Wunder, B., Wirth, R., and Gottschalk, M. (2001) Antigorite: Pressure and temperature dependence of polysomatism and water content. European Journal of Mineralogy, 13, 485-495.

Yang, K., Whitbourne, L., Mason, P., and Huntington, J. (2013) Mapping the chemical composition of nickel laterites with reflectance spectroscopy and Konaimbo, New Caledonia. Economic Geology, 108, 1285-1299.

Zussman, J., Brindley, G.W., and Corner, J.J. (1957) Electron diffraction studies of serpentine minerals. American Mineralogist, 42, 133-153.